uOttawa

L'Université canadienne
Canada's university

FACULTÉ DES ÉTUDES SUPÉRIEURES ET POSTOCTORALES

uOttawa

L'Université canadienne
Canada's university

FACULTY OF GRADUATE AND POSDOCTORAL STUDIES

Jason Boulet

AUTEUR DE LA THÈSE / AUTHOR OF THESIS

M.Sc. (Physics)

GRADE / DEGREE

Department of Physics

FACULTÉ, ÉCOLE, DÉPARTEMENT / FACULTY, SCHOOL, DEPARTMENT

The Effects of Delayed Visual Feedback on Postural Dynamics

TITRE DE LA THÈSE / TITLE OF THESIS

André Longtin

DIRECTEUR (DIRECTRICE) DE LA THÈSE / THESIS SUPERVISOR

Ramesh Balasubramaniam

CO-DIRECTEUR (CO-DIRECTRICE) DE LA THÈSE / THESIS CO-SUPERVISOR

Réjean Munger

Christopher Py

Peter Watson

Gary W. Slater

Le Doyen de la Faculté des études supérieures et postdoctorales / Dean of the Faculty of Graduate and Postdoctoral Studies

The Effects of Delayed Visual Feedback on Postural Dynamics

by

Jason Boulet

Thesis submitted to the
Faculty of Graduate and Postdoctoral Studies
In partial fulfillment of the requirements
For the Master of Science degree in
Physics

Department of Physics
Faculty of Science
University of Ottawa

Your file Votre référence
ISBN: 978-0-494-66241-0
Our file Notre référence
ISBN: 978-0-494-66241-0

Abstract

We report on experiments and modeling of the interactions between delayed visual feedback and postural control in human quiet stance. A heuristic model is derived based on physiological and psychophysical parameters. The level of agreement found between the data and the model was found to be very good for power spectral densities, probability density functions and mean-squared displacements (or Hurst exponents). The stochastic delayed differential model identifies critical time scales of postural corrections. We also investigate properties of the model such as stability, small delay approximations and the power spectral density. Lastly, we use nonlinear time series techniques to investigate the temporal structure of the experimental postural dynamics. We propose the first dynamical model of visually assisted posture control.

Acknowledgements

I would like to thank my supervisors Dr. André Longtin and Dr. Ramesh Balasubramaniam for somehow believing in me from day one and for their continual support: financially, intellectually and morally. In particular, I am thankful that Dr. André Longtin gave me the freedom to choose the direction and style of my work. He has been a constant guide with an open door and the voice of reason in the midst of my nonsense. I would also like to thank Dr. Ramesh Balasubramaniam for conceiving the idea of a Master's of Science in Physics for me and propagating some of my past interests to future ones. Although not directly related to my supervision, I thank Dr. Andreas Daffertshofer for devising the basis of my experimental work and being a stringent critic of my theoretical work.

For keeping me sane on the days that I was present at the lab, I would like to thank Brian Heffernan, Tyler Cluff and Brian Richardson. In particular, I am grateful for the aid afforded by James Jun and Maarten van den Heuvel in relation to my experiment.

Outside of the lab, friends have remarkably been by my side before this experience started—I am indebted abundantly to them. I have too many friends that have made substantial contributions to my development, to thank in this space; I can only trust that they know who they are. However there are two in particular that I shall name. Steven Zhang, for the mountain of support, friendship and ideas over the years. It was he who convinced me to take a stab at physics. Tyler Sylvestre, for the almost daily interactions that invariably led to reflections on an expanse of topics and thereby keeping my mind well-rounded. Also, the friendship.

My family, composed of my mother Dalilah, father Wayne, sister Pamela and brother Mathieu, I thank you from the deepest for the continual, unwavering sentiment that, where I am now, I should have always been. I would also like to thank my parents for raising me in the middle of nature itself and allowing me unbounded exploration to satisfy my curiosity.

Finally, over the past two years, $1/2 - \epsilon$ of my time has been dedicated to my re-

search, the remainder, $1/2 + \epsilon$, has been with my significant other, Justine. Thank you for allowing me to see another side of life. For an introduction on this topic, please refer to [72].

Dedication

Pour ma famille.

For my family.

Contents

List of Tables

List of Figures

List of Symbols and Acronyms

Symbols

β	Angular damping coefficient
χ	Order of strong convergence
Δt	Time step of integration or discretization
$\delta(t)$	Dirac Delta Function
ϵ	Percent of maximum L_2 norm; threshold
γ	Visual feedback strength
$\hat{\epsilon}$	Absolute error criterion
$\hat{\epsilon}(\Delta t)$	Absolute error criterion averaged over realizations
$\hat{x}$	Fourier Transform
$\Im$	Imaginary part of complex number
$\in$	Is a member of the set
κ	Proprioceptive feedback strength
λ	Eigenvalue
λ_1	Largest Lyapunov Exponent

$\langle\rangle$	Ensemble average
$\|\|\|\|$	Euclidean or L_2-norm
$\mathbb{C}$	Complex number
$\mathbb{R}$	Real number
$\mathbf{A}$	Jacobian evaluated at fixed point
$\mathbf{J}$	Jacobian
$\mathbf{R}_{i,j}$	Recurrence matrix or plot
tr	Trace of a matrix (sum of the diagonal elements)
μ_X	Mean of random variable X
ω	Angular frequency
$\Re$	Real part of complex number
σ_X^2	Variance of random variable X
τ	Generalized time lag or delay
τ_c	Critical time
τ_{prop}	Proprioceptive delay
τ_{vis}	Visual delay
θ	Angle in yz-plane with respect to the z-axis
ε	Rescaled inertial term (mgL/β)
$\xi(t)$	Gaussian White Noise
$\{F_z, \tau_x, \tau_y\}(t)$	z-component of force, x- and y-components of torque as functions of time

$\{V_{\text{amp}}\}(t)$	Output voltages from amplifier for $\{F_z, \tau_x, \tau_y\}(t)$
$\{V_{\text{amp}}\}_i$	Digitized output voltages from amplifier
a_r	Musculoskeletal noise intensity
a_s	'Drifting' noise intensity
D	Diffusion coefficient
d	Embedding dimension
F_N	Nyquist frequency
F_s	Sampling frequency
H	Hurst exponent
H_l	Long-term Hurst exponent
H_s	Short-term Hurst exponent
I	Moment of inertia
$K(\tau)$	Mean-squared displacement
L	Distance form floor to center of mass
m	Mass
$p_X(x)$	Probability density function of random variable X
r	Center of Pressure
$R_{xx}(\tau)$	Autocorrelation of x
RR	Recurrence rate
$S_{xx}(\omega)$	Power spectral density of x

$W(t)$	Wiener process or ordinary Brownian motion
$W_H(t)$	fractional Brownian motion
w_n	Hamming window
x^*	Complex conjugate or fixed point of x
X_n	Exact solution to the stochastic differential form of x at sample n
X_t	Exact solution to the stochastic differential form of x at time t
Y_n	Approximation of the stochastic differential form of x at sample n
Y_t	Approximation of the stochastic differential form of x at time t

Acronyms

ADC	Analog to Digital Converter
AMI	Average Mutual Information
AP	Antero-Posterior
CNS	Central Nervous System
COM	Center of Mass
COP	Center of Pressure
DDE	Delay Differential Equation
DOF	Degrees of Freedom
DVF	Delayed Visual Feedback
EC	Eyes Closed
EEG	Electroencephalography

EMG	Electromyography
fBm	fractional Brownian motion
FFT	Fast Fourier Transform
FNN	False Nearest Neighbor
FP	Force Plate
FPE	Fokker–Planck Equation
FT	Fourier Transform
GUI	Graphical User Interface
GWN	Gaussian White Noise
IFT	Inverse Fourier Transform
LCD	Liquid Crystal Display
MEG	Magnetoencephalography
ML	Medio-Lateral
MSD	Mean-Squared Displacement
oBm	ordinary Brownian motion
ODE	Ordinary Differential Equation
PDE	Partial Differential Equation
PDF	Probability Density Function
PSD	Power Spectral Density
PSR	Phase Space Reconstruction

RLC	resistor-inductor-capacitor
RP	Recurrence Plot
RQA	Recurrence Quantification Analysis
SDDE	Stochastic Delay Differential Equation
SDE	Stochastic Differential Equation
WSS	Wide Sense Stationary

Chapter 1

Introduction

Sensory feedback is an integral part of most biological systems. It allows for more accurate decision-making by updating its state, given its environment thereby enabling appropriate motor actions. In living organisms, in particular humans, these functions are executed by the *central nervous system* (CNS), composed of the brain and spinal cord. There are many levels of structural organization in the brain and a common point of view is that the basic building block is the *neuron* or nerve cell. These cells assemble into functional spatially separated areas. The connectivity that links these spatially defined brain areas and their functional cooperation is not well understood.

In this thesis we are particularly interested with how the brain executes a specific sensorimotor task: upright standing. This task is not as trivial as it would initially seem since the body is never fully at rest, constantly being perturbed by internal and external forces. A few senses are used to accomplish this task and it is not well understood how each of them contribute to standing given that the brain must control an unstable physical configuration. In the elderly population, this intrinsic physical instability along with decreasingly sensitive sensory neurons in the joints and feet degrades the information sent to the central nervous system, which eventually leads to an increased fall rate. As a result, falls are the most common cause of trauma and the largest single cause of accidental death in that age group [54]. To amplify the problem, an increasing proportion of the population is entering the elderly category in the Western world. Therefore, more fundamental research is warranted into determining how the central nervous system controls standing posture.

Despite the lack of knowledge about the integration by the brain of sensory information to make decisions on how to control the body, there is overwhelming evidence which suggests that upright posture is better controlled when eyes are open [63] compared to when eyes are closed. Therefore, to better understand the possible visual control loops involved in postural control, recent experiments on humans standing upright have delayed the visual stimulus in a visually guided postural task by 0–1000 milliseconds [67, 79]. The goal of such experiments was to determine the relative contribution that visual feedback has on postural control. By experimentally manipulating the arrival time, or the delay, of the visual stimulus, the time scales relating to slower and faster components of the control could possibly be disentangled. Amongst many possible questions, the following one has been front and center: will behavior entirely destabilize at some given delay and will there be a delay where balance becomes more stable? The authors in [67, 79] suggested that when complete destabilization does not occur, however, in a range of delays, namely 250–750 milliseconds, the standard deviation of postural sway was slightly lower relative to the other delay conditions. The slow components of postural sway appeared to be largely a function of the inertial mass of the participant, whereas the fast components were the consequence of both voluntary and involuntary muscle activity and the integration of multisensory feedback.

Since perturbing the proprioceptive system cannot be achieved without invasive treatment, in this thesis we use a similar experimental approach as [67, 79] with human subjects to study the visual contribution of postural control by varying the time delay of postural feedback for visual input. However, we obtain longer recordings (two minutes, instead of thirty seconds). We also capitalize on the groundwork that has accumulated in terms of simple models [19, 53, 86] of delayed feedback of postural sway. Since it is well established that the physical properties of the human body in rigid upright stance may be characterized as a stabilized inverted pendulum [24, 83], we focus on finding an appropriate controller of the body, and consequently propose a model which produces similar dynamics as the human postural control system with an explicit inclusion of visual input. This is the first combined experimental and modeling effort undertaken to explain the relative effects of two sensory inputs in the postural control system, visual and proprioceptive, as well as of the delay of visual feedback.

To assess the plausibility of a model, we compare it to the experimental data collected from human subjects using a series of numerical tests. These numerical tests are well established in the postural community: power spectral density and probability density functions of solutions. Another test, namely the mean-squared displacement [12] has shown that postural data contains two distinct diffusive regimes which have been linked to two different aspects of the control system: open-loop and closed-loop. Whereas [79] used linear filtering to find two different time scales of control of errors, [12] does not assume linearity of the system. The separation of the regimes is characterized by a critical time and each regime is characterized by a distinct Hurst exponent which quantifies the level of diffusion, which in turn relates to the level of control.

The use of dynamical systems theory allows for a systematic investigation of the stability of the postural model, and in particular to test what parameters influence the model's behavior and how. Time series analysis techniques derived from phase space reconstruction, typically used in the postural community, are also employed to investigate the underlying structure of the experimental data.

The organization of this thesis is as follows: in Chap. 2 we present notions of postural control models, dynamical systems theory, and stochastic processes which are used throughout. In Chap. 3, we give a derivation our postural control model and show how it can reproduce experimental data. In Chap. 4, we explain the experimental and numerical methods. Chapter 5 contains further analyses of our model, and in Chap. 6 we analyze our experimental data with nonlinear time series techniques. Finally, we conclude and lay out directions for future research in Chap. 7.

Publication Notes

Chapter 3 is based on the following published article:

J. Boulet, R. Balasubramaniam, A. Daffersthofer, and A. Longtin. Stochastic two delay-differential model of delayed visual feedback effects on postural dynamics. *Phil Trans R Soc A*, 368(1911):423–438, 2010. doi:10.1098/rsta.2009.0214

Chapter 6 will form the basis of another paper:

J. Boulet, T. Cluff, and R. Balasubramaniam. Intermittency in visually delayed postural dynamics.

Chapter 2

Background

2.1 Human Postural Kinematics

2.1.1 Mechanics and Physiology

Postural sway occurs in two dimensions: antero-posterior (AP) and medio-lateral (ML), yet we focus in this thesis on sway in the antero-posterior plane which is the side or profile view with movement from front to back and vice versa. We chose this focus because it has been shown that trajectories of postural sway in each dimension are independent and show similar dynamics [63]. The mechanical (bone and joint) structure of a human in this plane consists of a series of segmented links which are composed of limbs and connecting joints. Yet, for the small range of motion we are interested in, the multi-segmented or polymer-like chain of limbs moves negligibly. Therefore, the entire structure in the AP plane may be reduced to a pendulum with a joint between the attaching surface (floor) and the body [24].

The physiology of the human ankle is complex since it is composed of bones, tendons, muscles and cartilage (see Figs. 2.1(a) and 2.1(b)). The major muscles responsible for control of the lower leg are the *soleus*, *gastrocnemius* and *tibialis anterior* [39, 38]. The soleus is proximal to the *tibia* and the gastrocnemius, distal to the tibia, is also known

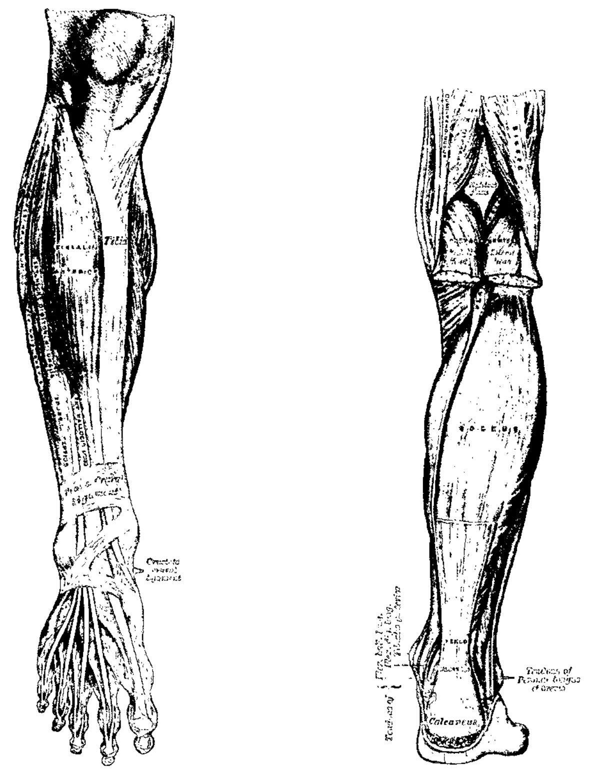

(a) Anterior view [26].

(b) Posterior view with the gastrocnemius removed [26].

Figure 2.1 – Lower human leg.

as the calf muscle; both muscles are located on the posterior portion of the lower leg. To allow for postural equilibrium by opposing contraction to the posterior muscles, in the anterior portion of the lower leg resides the tibialis anterior. However, in efforts to model the ankle's response to perturbations relative to the rest of the body, the ankle has often been reduced to a hinge joint supporting an inverted pendulum [24, 39, 38, 83, 82] (see Fig. 3.7). This pendulum has been characterized by a damping and a stiffness coefficient. In some studies, further simplification of the ankle joint has been pursed by neglecting ankle stiffness [19, 53, 86] since it is not a passive property of its physiology; active or control properties will be covered in Sect. 2.1.2.

With eyes open, compared to eyes closed (EC), it was found that the center of pressure (COP) (which is the sum of the ground reaction forces divided by the torques felt by the ground, exerted by the feet; also see Sect. 4.1.1 for an in-depth definition of the COP) motion was overdamped [81]. Experimental estimates of the damping coefficients have been reported [83] which we use later for modeling.

2.1.2 Neural Sensory Information and Control

In general, sensory information for a neural control system is provided by *afferent* inputs [33]. These inputs are captured by *neurons* at the periphery and transmitted to the central nervous system (CNS) which includes the brain, brain stem and spinal chord. After the CNS has processed and made decisions on the afferent inputs, the CNS generates motor commands and *efferent* signals are propagated in the opposite direction along separate "motor" neurons, from the CNS to the periphery. These signals execute motor commands.

The postural control system makes use of three main afferent inputs: *proprioception*, *vestibular* perception and *vision* [9, 57, 33]. The first, proprioception, in terms of quiet stance in humans, is mostly provided by *mechanoreceptors* (which are typically nerve endings that respond to pain, pressure or light touch) some of which are located in the sole of the foot [16]. Other mechanoreceptors include stretch receptors in muscles called muscle spindle receptors; Golgi tendon organs, which are receptors in the tendon that sense contractile force or effort exerted by a group of muscle fibers; and receptors located in joint capsules that sense flexion or extension of the joint [33].

The second sensory system which offers vestibular perception, is provided by the *otolithic* organs and the *semicircular canals* in the inner ear or *labyrinth*. The otolithic organs are composed of the *utricle* which detects gravity and the *saccule* which detects linear acceleration in the vertical orientation. Since quiet standing has a zero acceleration in the vertical orientation, the saccule does not provide useful information. The *otoconia* crystals in the utricle rest on a viscous gel layer and are heavier than their surroundings.

Consequently, the crystals get displaced during linear acceleration, and therefore, bend the *ciliary bundles* of the hair cells, producing an afferent sensory signal [60]. As a result, this type of afferent input is acceleration-dependent. However, for zero acceleration (or constant velocity), the contribution of this portion of the vestibular perception is below threshold for detection [20]. If acceleration of the head is detected, then the utricle may detect angles from the completely upright head position as small as 0.5 degrees [28]. However, as the head angle increases, the accuracy of determining this angle degrades. The orientation of the semicircular canals is such that they are approximately orthogonal to each other. The semicircular canal afferents are exclusively sensors of rotational forces and therefore do not contribute to postural control, in quiet standing. It has also been reported form multisensory postural experiments that when proprioception and vision are present, vestibular perception is not reliable [57]. Therefore, the contribution of the vestibular system is not well known for postural control in the context of quiet stance. Because of this, we will not explicitly model vestibular feedback. Any possible contribution attributed to the vestibular system will be lumped with proprioception.

Lastly, vision, involves photons captured though the eyes, projected onto the retina, transmitted down the optic nerve to the *lateral geniculate nucleus* and perceived in the hindbrain, mostly composed of the visual *cortices* (V1–V5) [33], see Fig. 2.2. Hence, vision is a much higher-brain-level function than proprioception and vestibular perception since after optical input has been rendered by the the visual cortices, this information projects to multiple cortical areas. Because of this, from a neural pathway perspective, it is not clear what effects this has on the postural system. Despite this, behavioral postural studies have shown that postural sway is reduced when eyes are open compared to when eyes are closed [14, 69, 17]. Also, some studies [67, 79] have shown that lengthening the visual-loop delay gives rise to two distinct time scales (as a function of the delay) apparent in the center of pressure trajectories of postural sway.

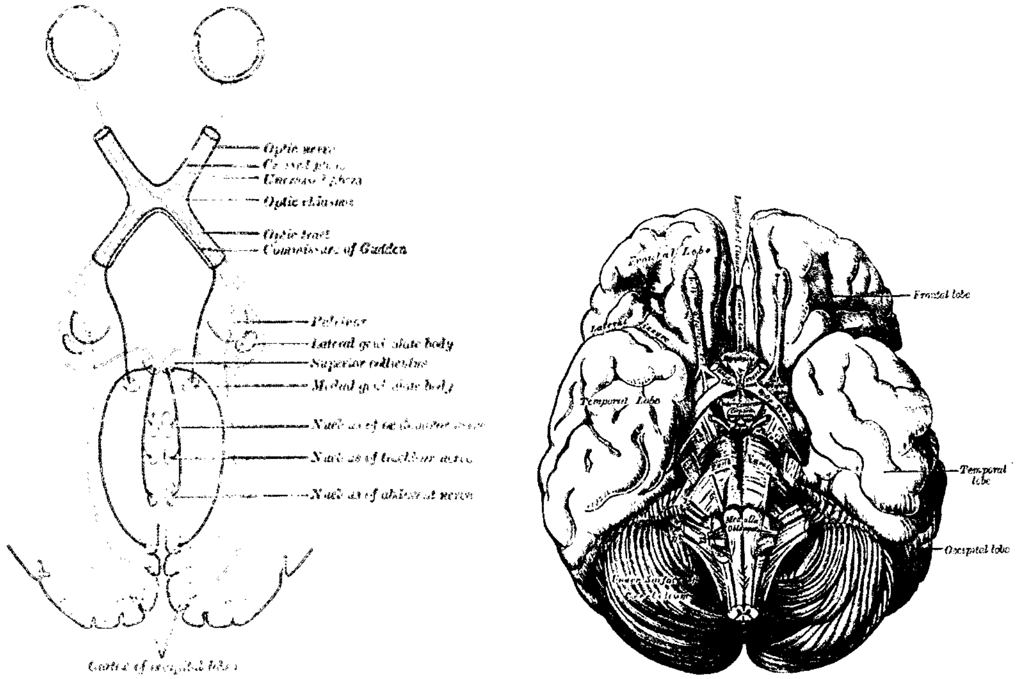

(a) Optic tract [26].

(b) Base of the brain showing the *occipital lobe*—the visual processing area [26].

Figure 2.2 – The visual system.

2.1.3 Postural Control Models

Linear Control Theory Models

The postural control literature admits to two main classes of control models. The first are the type of postural models that are derived from a more general class of sensorimotor models that make use of linear control theory and *internal models* [9, 84, 76, 31, 30, 34, 57]. An internal model is a hypothetical central neural representation of the dynamics and kinematics of movement, which is believed to underlie the nervous system's remarkable ability to discern unknown or underdetermined changes in the environment. There are many variations of these types of models, however, the main concept is as follows. Sensory information (proprioception, vestibular perception and vision) is the input to the system. From here, the internal model translates the sensory information into a kinematic state (position, velocity and acceleration). From this current state, the internal model predicts the future iteration of the state given its knowledge about the *plant* (the subsystem-to-be-controlled). It compares the future state with how the system executes this state and uses the difference between the two signals as an error which is considered to predict the next state in the next iteration.

For example, Kiemel *et al.* [34] analyzed the stochastic structure of postural sway with optimal estimation theory based on the inverted pendulum. They have demonstrated that this structure imposes constraints on postural control models. Experimentally, for each subject and sensory condition, a model of appropriate order was determined, and this model was characterized by the eigenvalues and coefficients of its auto-covariance function. Linear stochastic models of various orders were fit to the center of mass trajectories of subjects during quiet stance in four sensory conditions: (i) light touch and vision, (ii) light touch, (iii) vision, and (iv) neither touch nor vision. In most cases, postural-sway trajectories were similar to those produced by a third-order model.

The system's variables are composed of the state vector, whose components are position x_1 and velocity x_2

$$\mathbf{x} = \begin{bmatrix} x_1 \\ x_2 \end{bmatrix}. \tag{2.1}$$

The internal state estimate vector is

$$\hat{\mathbf{x}} = \begin{bmatrix} \hat{x}_1 \\ \hat{x}_2 \end{bmatrix}. \tag{2.2}$$

The control signal vector is u and finally, the sensory measurements are

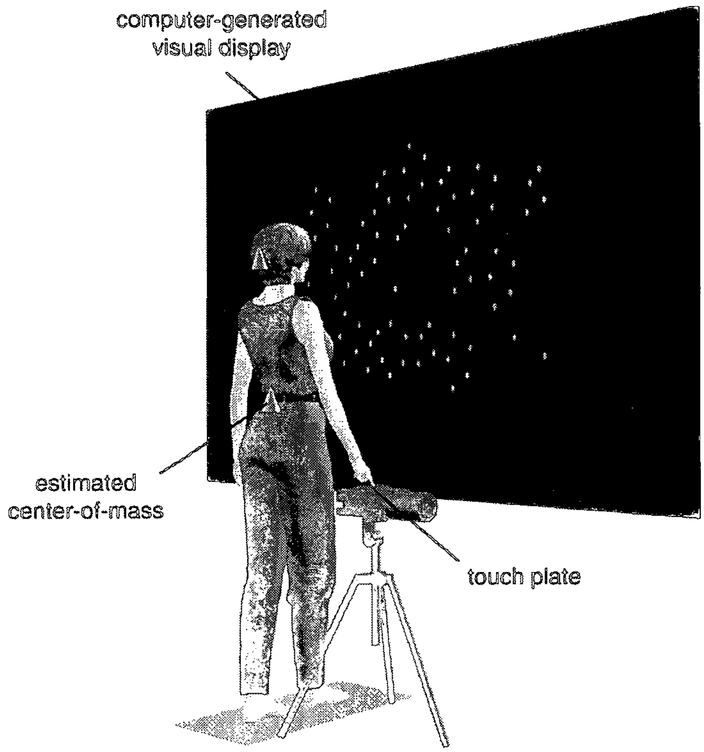

Figure 2.3 – Experimental setup for Kiemel *et al.* [34].

$$\mathbb{z} = \begin{bmatrix} z_1 \\ z_2 \\ z_3 \end{bmatrix}. \tag{2.3}$$

Estimates of the state are computed based on a Kalman filter [32] (or linear quadratic estimation) which is an iterative filter that estimates the state of a linear discrete-time system from noisy measurements and the system's control. Using a predict and update rule, the Kalman filter returns the optimal estimate of the state assuming that all of the noise present within and outside the system is GWN. The full model may be written as

$$\dot{\mathbf{x}} = \mathbf{F}\mathbf{x} - \mathbf{G}\mathbf{C}\hat{\mathbf{x}} + \mathbf{w}(t) \tag{2.4}$$

$$\dot{\hat{\mathbf{x}}} = (\mathbf{F} - \mathbf{G}\mathbf{C}\hat{\mathbf{x}}) + \mathbf{K}(\mathbf{z} - \mathbf{H}\hat{\mathbf{x}}) \tag{2.5}$$

$$\mathbf{z} = \mathbf{H}\mathbf{x} + \mathbf{v}(t) \tag{2.6}$$

$$u = -\mathbf{C}\hat{\mathbf{x}}. \tag{2.7}$$

The control coefficient matrix is

$$\mathbf{C} = \begin{bmatrix} c_1 & c_2 \end{bmatrix}. \tag{2.8}$$

The state transition matrix is

$$\mathbf{F} = \begin{bmatrix} 0 & 1 \\ \gamma & 0 \end{bmatrix} \tag{2.9}$$

and

$$\mathbf{G} = \begin{bmatrix} 0 \\ 1 \end{bmatrix}. \tag{2.10}$$

The observation or measurement matrix is

$$\mathbf{H} = \begin{bmatrix} 1 & 0 \\ 0 & 1 \\ \gamma & 0 \end{bmatrix} \tag{2.11}$$

and the covariance matrix of the process noise is

$$\mathbf{Q} = \begin{bmatrix} 0 & 0 \\ 0 & \sigma^2 \end{bmatrix}. \tag{2.12}$$

The covariance matrix of the measurement noise is

$$\mathbf{R} = \begin{bmatrix} \sigma_1^2 & 0 & 0 \\ 0 & \sigma_2^2 & 0 \\ 0 & 0 & \sigma^2 + \sigma_2^2 \end{bmatrix}. \tag{2.13}$$

The computational noise covariance matrix is

$$\mathbf{R}_c = \begin{bmatrix} \sigma_{c1}^2 & 0 \\ 0 & \sigma_{c2}^2 \end{bmatrix} \tag{2.14}$$

Additional matrices defining the system are

$$\mathbf{T} = \begin{bmatrix} 0 & 0 & 0 \\ 0 & 0 & \sigma^2 \end{bmatrix} \tag{2.15}$$

$$\mathbf{U} = \begin{bmatrix} \mathbf{F} - \mathbf{KH} & 0 \\ 0 & \mathbf{F} - \mathbf{GC} \end{bmatrix} \tag{2.16}$$

$$\mathbf{Z} = \begin{bmatrix} \mathbf{Q} + \mathbf{KRK}^T - \mathbf{TK}^T - \mathbf{KT}^T + \mathbf{R}_c & \mathbf{TK}^T - \mathbf{KRK}^T - \mathbf{R}_c \\ \mathbf{KT}^T - \mathbf{KRK}^T - \mathbf{R}_c & \mathbf{KRK}^T + \mathbf{R}_c \end{bmatrix} \tag{2.17}$$

where ^{T} denotes the transpose and $\mathbf{K}$ is the Kalman gain matrix chosen to minimize the error form the vertical position

$$J = \left\langle d_1 \left(x_1 - \hat{x}_1\right)^2 + d_2 \left(x_2 - \hat{x}_2\right)^2 \right\rangle. \tag{2.18}$$

The noise variables are $\mathbf{w}(t)$, the process noise, $\mathbf{v}(t)$, the measurement noise and $\mathbf{z}(t)$, the sensory measurement noise, which are assumed to be Gaussian and satisfy

$$\left\langle \mathbf{w}(t_1)\, \mathbf{w}^T(t_2) \right\rangle = \delta(t_1 - t_2)\, \mathbf{Q} \tag{2.19}$$

$$\left\langle \mathbf{v}(t_1)\, \mathbf{v}^T(t_2) \right\rangle = \delta(t_1 - t_2)\, \mathbf{R} \tag{2.20}$$

$$\left\langle \mathbf{w}(t_1)\, \mathbf{v}^T(t_2) \right\rangle = \delta(t_1 - t_2)\, \mathbf{T} \tag{2.21}$$

$$\left\langle \mathbf{z}(t_1)\, \mathbf{z}^T(t_2) \right\rangle = \delta(t_1 - t_2)\, \mathbf{Z}. \tag{2.22}$$

The findings from Kiemel *et al.* [34] suggest that computation noise is responsible for most of the variance observed in postural sway, and the postural control system under the conditions tested resides in the regime of accurate velocity information. However, from the large set of parameters, given in the above model, it is not surprising that it is capable of accurately fitting a complex process such as postural sway with sensory inputs. Yet, it is not easy to study properties of this system analytically, and further there is a strong assumption that the system is linear. Therefore, if the system is nonlinear, this state estimation process becomes even more complicated than it already is. Hence, it is difficult to develop an intuition for the complex processes at hand.

Dynamical Systems Models

The second class of models [6, 10, 19, 52, 51, 53, 71, 86] use the approach of dynamical systems by focusing solely on the observable kinematics to hypothesize a neural control mechanism, since the actual control mechanism is to a large degree unknown. Typically, a simple control rule is used and the "plant" (the subsystem-to-be-controlled) is assumed to be known. For example, in simple postural control models, the plant is usually the inverted pendulum, which is a second order nonlinear oscillator. The controller is usually a time-delayed function of the state. The advantage of this approach is that properties of the system's behavior *i.e.*, stability, are easier to compute due to the accumulated theory of dynamical systems.

Chow and Collins [10] have proposed a model of postural sway using a continuous pinned polymer as a "body", embedded in an elastic force field, as an attempt to explain the underlying fluctuations in transverse motion $y \equiv y\,(z,t)$ of standing posture, where z is the height of the polymer and t, the time. Their model is governed by

$$\rho\frac{\partial^2 y}{\partial t^2} + \mu\frac{\partial y}{\partial t} = T\frac{\partial^2 y}{\partial z^2} - Ky + F\,(z,t) \tag{2.23}$$

where ρ is the mass density, μ is the friction, T is the tension, K is the elastic restoring force and $F(z,t)$ is the stochastic (thermal) driving force. This equation reproduces the proper Hurst exponents and shape of the PSD, yet makes no claims about a possible human control system and does not take into account physical human properties.

Eurich and Milton [19] have shown that the mean-squared displacement of experimental data may be represented by assuming that human postural sway may be controlled in a switch-like behavior. Movement inside a boundary of support defined by the region $-1 \leqslant x \leqslant 1$ tends to drift outwards to a boundary without corrective steps. If the trajectory moves beyond ± 1, it may only be detected after a delay of τ, to account for finite neural conduction, processing and neuromuscular response times. At this point, negative feedback is used in a discontinuous fashion by reversing its trajectory with magnitude C. The first-order position-based dynamical model is given as

$$\dot{x} = \begin{cases} x + \sqrt{2D}\xi(t) + C & \text{if } x(t-\tau) < -1 \\ x + \sqrt{2D}\xi(t) & \text{if } -1 \leqslant x(t-\tau) \leqslant 1 \\ x + \sqrt{2D}\xi(t) - C & \text{if } x(t-\tau) > 1 \end{cases} \tag{2.24}$$

where x, t, $\sqrt{2D}$ (the GWN intensity), C, the feedback strength, and the delay τ have been rescaled (as an overdamped pendulum).

Yao *et al.* [86] have used a similar approach to modeling human postural sway as Eurich and Milton [19], except for one crucial difference. Instead of discontinuous control, continuous negative feedback is used. The form of the model is shown below

$$\dot{x}(t) = \alpha x(t) + \beta \tanh[x(t-\tau)] + \gamma\eta(t) \tag{2.25}$$

where $\alpha \approx \sqrt{mgl/2I}$ and m is the mass, l is the center of mass and I is the moment of inertia. The feedback strength is $\beta < 0$, while tanh, the hyperbolic tangent function, a sigmoidal function, which is widely used in neural networks and psychophysics where it represents a smoothed switch for feedback when displacement occurs. The perturbations are modeled by GWN, $\eta(t)$, with intensity γ.

This modeling approach is also used for related human control tasks. An example of balancing a stick at the fingertip by Cabrera [6] is

$$\ddot{\theta} + \Gamma\dot{\theta} - q\sin\theta + R(t)\theta(t-1) = 0. \tag{2.26}$$

All variables and parameters have been rescaled. The angle formed by the two end points of the stick is θ, Γ is the damping term, q is the 'mgL' term, $R(t) \equiv [R_0 + \xi(t)]$ is the stochastic restoring force, where R_0 is a nonzero constant force, $\xi(t)$ is GWN and the delay is 1.

2.2 Phase Space, Flow and Vector Fields

Dynamics is a word often used to refer to the change in the state of an object over time. Any *dynamical system* consists of a set of variables, which are functions of time, that evolve according to a specific set of rules. In this text, time derivatives will be written in Newton or dot notation shown below

$$\dot{x} \equiv \frac{\mathrm{d}x}{\mathrm{d}t}$$

where x is the variable. A mathematical description of a dynamical system may be written as a set of ordinary differential equations (ODE). In fact, any n-th order ODE, or system, may be written as a set of n first-order ODEs such as $\dot{\mathbf{x}} = \mathbf{f}(\mathbf{x})$, also known as a *vector field*. The *flow* is the ensemble of all possible trajectories formed by all state variables in *phase space*, in a time-continuous dynamical system. The basis of the phase space is spanned by unit vectors associated with each state variable.

For example, the series resistor-inductor-capacitor (RLC) circuit may be described as a second-order differential equation

$$\frac{\mathrm{d}^2 q}{\mathrm{d}t^2} + \frac{R}{L}\frac{\mathrm{d}q}{\mathrm{d}t} + \frac{1}{LC}q = \frac{1}{L}v \tag{2.27}$$

where q, the charge, and v, the voltage, are both functions of time; R is the resistance, L is the inductance and C, the capacitance. We can define a new quantity, the current, i which is related to the charge by

$$i = \frac{\mathrm{d}q}{\mathrm{d}t},$$

and rewrite Eq. (2.27) in terms of the current to reduce it to a first-order equation

$$\frac{\mathrm{d}i}{\mathrm{d}t} + \frac{R}{L}i + \frac{1}{LC}q = \frac{1}{L}v$$

such that the second order RLC circuit equation may be written in terms of two first order differential equations

$$\begin{aligned}\dot{q} &= i \\ \dot{i} &= -\frac{R}{L}i - \frac{1}{LC}q + \frac{1}{L}v.\end{aligned}$$

2.3 Attractors

An *attractor*, A, is a closed set of points such that any trajectory $\mathbf{x}(t)$ that begins in A, stays in A for all t. The set of initial conditions, $\{\mathbf{x}(0)\}$, which A attracts, or converges to as $t \to \infty$, is known as the *basin of attraction*. The final criterion describing any attractor is that there is no subset of A that satisfies the above conditions. An attractor, therefore, is a stable set.

Attractors are known to exist in four varieties: the (i) *fixed point*, (ii) *limit cycle*, (iii) *torus* and (iv) *strange attractor*. In this thesis we will only consider (i) and (ii) for now. Later in this chapter, and in Chap. 6 we will return to (iv). A fixed point, also known as an equilibrium point, $\mathbf{x}^*$, satisfies $\mathbf{f}(\mathbf{x}^*) = 0$, and is the point where the flow moves toward or away from. A simple test to determine fixed point stability is via *linear stability analysis*. For the system $\dot{\mathbf{x}} = \mathbf{f}(\mathbf{x})$ of dimension n, where the fixed points are known, the system may be linearized in the form $\dot{\mathbf{x}} = \mathbf{A}\mathbf{x}$, by computing its Jacobian $\mathbf{J}$ (which is the matrix of all first-order partial derivatives of a vector-valued function) and evaluating it at each fixed point, so $\mathbf{A} = \mathbf{J}(\mathbf{x}^*)$. After the system is linearized, the eigenvalues of the system λ_k (where $k = 1, \ldots, n$) are computed by using the trial solution $\mathbf{x} = \mathbf{x}(0)\exp(\lambda t)$ and solving for λ. In general, the eigenvalues take the form $\lambda = \mu \pm i\omega$ (where λ is a complex number, since $i = \sqrt{-1}$) and are obtained by solving $\det(\mathbf{A} - \lambda\mathbf{I}) = 0$ for λ. If $\Re\{\lambda\} < 0$, where $\Re$ denotes the real part of the complex-valued eigenvalue, then the flow is convergent, and hence stable, therefore it is an attractor. If, however, $\Re\{\lambda\} > 0$, then the flow is divergent, and the fixed point is unstable, consequently it is a *repeller*. Otherwise, $\Re\{\lambda\} = 0$, linear stability analysis fails and one must perform nonlinear stability analysis by considering higher order terms rendered by the Taylor expansion of $\mathbf{f}(\mathbf{x})$ around $\mathbf{x}^*$. If there are many fixed points, linear stability analysis can be done around each of them to yield multiple local information, *i.e.*, the flow about each point. From this, the local flows may sometimes be connected together to give the global picture of phase space flow.

For example, the RLC circuit from Eq. (2.27) in an overdamped configuration (where $\sqrt{L/C} < R/2$) and with $v = 0$ has the trivial stable fixed point $(q^*, i^*) = (0, 0)$. The matrix $\mathbf{A}$ for this system is

$$\mathbf{A} = \begin{bmatrix} 0 & 1 \\ -\dfrac{1}{LC} & -\dfrac{R}{L} \end{bmatrix}$$

and therefore, the eigenvalues are computed by

$$\det(\mathbf{A} - \lambda\mathbf{I}) = 0$$
$$\begin{vmatrix} -\lambda & 1 \\ -\dfrac{1}{LC} & -\dfrac{R}{L} - \lambda \end{vmatrix} = 0$$
$$\lambda^2 + \frac{R}{L}\lambda + \frac{1}{LC} = 0$$

which yield

$$\lambda_{1,2} = -\frac{R}{2} \pm \frac{\sqrt{R^2 - 4L/C}}{2}.$$

Recall that the fixed point is stable if $\Re\{\lambda\} < 0$. Considering the overdamped case where $\sqrt{L/C} < R/2$, or $R/2 > \sqrt{R^2 - 4L/C} > 0$, then $\Re\{\lambda_{1,2}\} = \lambda_{1,2} < 0$, hence, the system is stable.

The limit cycle is relatively harder to define. It implies that trajectories converge to or away from self sustained oscillations, whereas the fixed point refers to a convergence to one point only. Establishing the existence of limit cycles may be treated with the *Poincaré–Bendixson Theorem* [72] below, where a *closed orbit* is just a periodic (with period T) trajectory in phase space, *i.e.*, $\mathbf{x}(t) = \mathbf{x}(t+T)$.

Theorem 1 (Poincaré–Bendixson [72]).

(i) *R is a closed, bounded subset of the two-dimensional manifold, or plane;*

(ii) *$\dot{\mathbf{x}} = \mathbf{f}(\mathbf{x})$ is a continuously differentiable vector field on an open set containing R;*

(iii) *R does not contain any fixed points; and*

(iv) *There exists a trajectory C that that is "confined" in R, in the sense that it starts in R and stays in R for all future time. Then C is either a closed orbit or spirals toward a closed orbit as $t \to \infty$.*

An example of a stable limit cycle (certain parameter values) is the Van der Pol oscillator which takes the form $\ddot{x} - \mu(1 - x^2)\dot{x} + x = 0$. Let us use the Poincaré–Bendixson Theorem to confirm that the Van der Pol oscillator is indeed an limit cycle, when $\mu = 1$. We may rewrite the Van der Pol equation as the 2-dimensional system

$$\dot{x} = y$$
$$\dot{y} = \mu\left(1 - x^2\right)y - x.$$

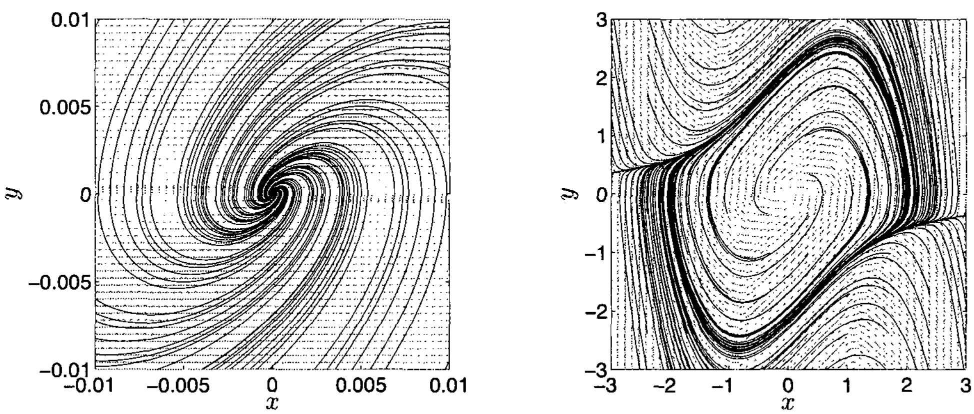

(a) Unstable fixed point, $\mu = -1$. (b) Limit cycle attractor, $\mu = 1$.

Figure 2.4 – Van der Pol oscillator.

It is obvious that the system admits to the trivial fixed point $(x^*, y^*) = (0, 0)$. Therefore the Jacobian of the linearized system, evaluated at its fixed point is

$$\mathbf{A} = \begin{bmatrix} 0 & 1 \\ -1 & \mu \end{bmatrix}.$$

The linear stability analysis in two dimensions is determined by computing the trace and determinant of $\mathbf{A}$. In this case, $\operatorname{tr}\mathbf{A} = \mu$ and $\det\mathbf{A} = 1$. According to theory [72], if

$\operatorname{tr}\mathbf{A} > 0$ and $\det \mathbf{A} > 0$ the fixed point is an unstable spiral, since $\mu = 1$ (also seen in Fig. 2.4(a)). The Poincaré–Bendixson Theorem can be used by defining R as an area around this unstable fixed point that excludes the fixed point itself (*e.g.*, the annulus R). Since the Van der Pol system is a continuously differentiable vector field, it is then clear from Fig. 2.4(b) that the system satisfies the remaining conditions of the Poincaré–Bendixson Theorem, proving the existence of a limit cycle.

2.4 Bifurcations and Nonlinear Dynamics

Linear systems explain a large subset of observed phenomenon very easily. Properties of linear ODEs, such as linear superposition, make analysis much simpler than with *nonlinear* ODEs. While linear systems provide adequate approximations to the flow, especially in the vicinity of hyperbolic fixed points (for which $\Re\{\lambda\} \neq 0$), they are only capable of providing fixed point and oscillatory solutions. In general, the solutions of all linear systems converge to a constant or $\pm\infty$, either monotonically ($\Im\{\lambda\} = 0$, where $\Im$ denotes the imaginary part) or in an oscillatory fashion ($\Im\{\lambda\} \neq 0$). To explore the larger spectrum of dynamics such as limit cycles and *chaos*, we must turn to nonlinear dynamics. In the context of nonlinear ODEs, the term nonlinear refers to the nonlinearity in the functions of the state vector, $\mathbf{x}$. A set of nonlinear ODEs may be written as follows

$$\dot{\mathbf{x}} = \mathbf{A}(\boldsymbol{\alpha})\,\mathbf{x} + \mathbf{g}(\mathbf{x}, \boldsymbol{\alpha}) \tag{2.28}$$

where $\mathbf{A}$ is a matrix of constant coefficients of the linear portion, $\mathbf{g}$ is a vector of nonlinear functions of $\mathbf{x}$ and $\boldsymbol{\alpha}$ is a set of parameters. For example, the Van der Pol equations may be rewritten in the form

$$\begin{bmatrix} \dot{x} \\ \dot{y} \end{bmatrix} = \begin{bmatrix} 0 & 1 \\ -1 & \mu \end{bmatrix} \begin{bmatrix} x \\ y \end{bmatrix} + \begin{bmatrix} 0 \\ -\mu x^2 y \end{bmatrix} \tag{2.29}$$

where, comparing with Fig. 2.5, $g_x(\mathbf{x}, 0) = 0$, and $g_y(\mathbf{x}, \mu) = -\mu x^2 y$. The variation of $\boldsymbol{\alpha}$ can cause, past certain critical values, the system to undergo qualitative changes to its phase space structure. This change is known as a *bifurcation.* Some common bifurcations are the saddle-node bifurcation which happens when two distinct fixed points (one stable, the other unstable) collide into one another and mutually annihilate. The transcritical bifurcation is an example of two fixed points of opposite stability colliding; after the point of collision, the fixed points exchange stability. The pitchfork bifurcation is abundant in systems with spatial symmetry. It describes the appearance or disappearance of fixed points in pairs, stable or unstable (supercritical or subcritical, respectively). However, probably of most interest to this thesis is the Andronov–Hopf bifurcation. This bifurcation occurs when the eigenvalues of the Jacobian at the fixed point become imaginary, *i.e.*, of the form $\lambda = \pm i\omega_{\text{crit}}$, where ω_{crit} is the frequency of oscillation at the bifurcation. Therefore, the Jacobian at the fixed point in this case is $\mathbf{A}$ with eigenvalues are

$$\lambda_{1,2} = \frac{\mu}{2} \pm \frac{1}{2}\sqrt{\mu^2 - 4}.$$

Hence, for a Andronov-Hopf bifurcation to occur, $\mu_{\text{crit}} = 0$, and therefore, $\lambda_{1,2} = \pm i$, so $\omega_{\text{crit}} = 1$. If $\mu > 0$, the fixed point at the origin becomes unstable since $\Re\{\lambda_{1,2}\} > 0$ and all flow moves onto the limit cycle. However, if $\mu < 0$, then $\Re\{\lambda_{1,2}\} < 0$ and the fixed point becomes stable, and the limit cycle no longer exists (see Fig. 2.5). This is the case for the so-called supercritical Andronov–Hopf bifurcation.

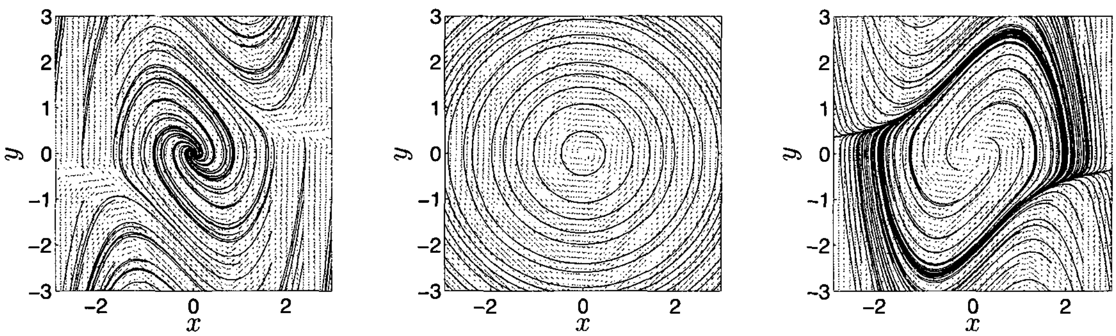

(a) $\mu = -1 < 0$ (b) $\mu = 0$ (c) $\mu = 1 > 0$

Figure 2.5 – Andronov-Hopf bifurcation of the Van der Pol oscillator.

2.5 Time Delays in Dynamical Systems

Time delays are relevant in systems where the state is dependent on one or more past states. In fact, in more recent years, there has been an increase in the use of *delay differential equations* (DDE) in an attempt to model such systems more realistically. Delays typically arise when feedback to the system can only be obtained after a nonzero, finite time. Usually physical systems involving a finite transmission velocity may be modeled with a delay. A general form of a DDE with one degree of freedom and one delay is

$$\dot{x}(t) = f\left(x(t), x(t-\tau)\right)$$

where τ is a constant delay.

Their solutions, however, are far from trivial. First, analogous to the initial condition required for ODEs, an initial history function, $\phi(t)$ where $t \in [-\tau, 0]$ must be chosen, which may produce a discontinuity at $t = 0$. However, as we will soon learn, this is not the biggest problem. Most linear DDEs assume the *ansatz* (or trial solution) to be $x(t) = x(0)\exp(\lambda t)$, from which a characteristic equation may be found. For example, let us choose the DDE, $\dot{x}(t) = ax(t) + bx(t-\tau)$. Then the corresponding characteristic equation around the fixed point $(0,0)$ is

$$\lambda - a - b\exp(-\lambda\tau) = 0$$

which is a transcendental equation that implies an infinite number of complex roots. These roots come in complex conjugate pairs. Hale *et al.* [29] commented on this problem:

> For the autonomous matrix equation... $\dot{x}(t) = Ax(t) + Bx(t-r)$ ...the exact region of stability as an explicit function of A, B and r is not known and probably will never be known. The reason is simple to understand because the characteristic equation is so complicated. It is therefore worthwhile to obtain methods for determining approximations to the region of stability.

Therefore, analytical solutions for the vast majority of DDEs do not exist. As a consequence, we shall resort to numerical methods for the solution of DDEs. Numerical methods will also be used to obtain the roots λ_k of the characteristic equation. If the DDE is linear, the solution can be obtained as a sum over the infinite number of linear modes,

$$x(t) = \sum_{k=1}^{\infty} c_k \exp(\lambda_k t) \tag{2.30}$$

where the coefficients c_k are determined by the initial history function. The real part of these eigenvalues dictate the local stability.

2.6 Stochastic Processes

2.6.1 Quantification of Stochastic Dynamics

Dynamically, the dimensionality of stochastic processes is relatively high compared to deterministic processes. Some types of noise, or stochastic processes such as Gaussian white noise (GWN) are of infinite dimension because it is an infinite collection of independent and identically distributed random variables along the time axis. Yet, noise may exist in a dynamical system, that is, a system may have a deterministic component as well as a stochastic one. Hence from now on, dimensionality will refer to the deterministic part of the system. There are numerous reasons for including noise into a dynamical system, the simplest being uncertainty.

Stochastic processes, which are functions of time, may be viewed from two perspectives. First, since the inherent nature of noise is random, and given a large set of possible outcomes to an event, for a finite period of time, any noisy or truly random sequence of numbers will never repeat itself. This view is based on that of *realizations* of a process, or individual trials of a stochastic process. The other view is based on the statistics of the process. A one dimensional stochastic process is a case with one random variable X, with corresponding realizations $x(t)$, where $x \in \mathbb{R}$. The ensemble average is the mean value of the process over all realizations and may be a function of time $\langle x(t) \rangle$. The other type of average for stochastic processes is the time average measured over time with one realization. For an *ergodic* process, the time and ensemble average of $x(t)$ are equal:

$$\langle x(t) \rangle = \lim_{T \to \infty} \frac{1}{T} \int_0^T x(t)\, \mathrm{d}t. \tag{2.31}$$

Note that all stochastic measures mentioned in this thesis are generalizable to higher dimensions. If the probability distribution function (PDF) $p_X(x)$ is known, then the mean of the distribution of random variable X is given by

$$\mu_X = \int_{-\infty}^{\infty} x p_X(x) \, \mathrm{d}x. \tag{2.32}$$

Similarly, the variance of X is

$$\sigma_X^2 = \int_{-\infty}^{\infty} (x - \mu_X)^2 \, p_X(x) \, \mathrm{d}x. \tag{2.33}$$

Mean-Squared Displacement

The *mean-squared displacement* (MSD), or two-point correlation of $x(t)$ is

$$K(\tau) = \left\langle [x(t+\tau) - x(t)]^2 \right\rangle, \tag{2.34}$$

which depends only on $\tau = t' - t$, where $t' \geqslant t$.

Autocorrelation

The *autocorrelation* of $x(t)$ with mean μ_X and variance σ_X^2 is the mean value of the product of a random variable realization with a time-shifted version of itself

$$R_{xx}(t, t') = \frac{\langle [x(t) - \mu_X] \, [x(t+\tau) - \mu_X] \rangle}{\sigma_X^2}. \tag{2.35}$$

The autocorrelation depends only on the difference between two times, τ, if the process is wide sense stationary (WSS), that is if the mean and variance do not vary as a function of time. The autocorrelation is also the auto-covariance normalized by the variance of $x(t)$. Another fundamental property of the autocorrelation function is that it is symmetric about $t = 0$.

Power Spectral Density

The *Fourier Transform* (FT) is used to transform $x(t)$ into $\hat{x}(\omega)$, where $\hat{x}$ is a complex-valued function of angular frequency ω. This transform is defined by

$$\hat{x}(\omega) = \int_{-\infty}^{\infty} x(t) \exp\left(-i\omega t\right) \, \mathrm{d}t \tag{2.36}$$

and the *Inverse Fourier Transform* (IFT) is

$$x(t) = \frac{1}{2\pi} \int_{-\infty}^{\infty} \hat{x}(\omega) \exp\left(i\omega t\right) \, \mathrm{d}\omega. \tag{2.37}$$

Since the FT is complex-valued, it may be written in polar coordinates. Then, both an amplitude and phase spectrum may be derived from it. However, here we are only concerned with the amplitude or more specifically, the *power spectral density* (PSD), given by

$$S_{xx}(\omega) = \langle \hat{x}(\omega) \hat{x}^*(\omega) \rangle \tag{2.38}$$

where * denotes the complex conjugate. Additionally, if $x(t)$ is WSS, then the PSD is just the FT of the auto-covariance, $\sigma^2 R_{xx}(\tau)$ (Wiener-Khintchine theorem)

$$S_{xx}(\omega) = \sigma^2 \int_{-\infty}^{\infty} R_{xx}(\tau) \exp\left(-i\omega\tau\right) \, \mathrm{d}\tau. \tag{2.39}$$

2.6.2 Gaussian White Noise

The probability density function of Gaussian White Noise (GWN), $\xi(t)$, is the Gaussian distribution where μ_ξ is the mean and $\langle\xi(t)\xi(t')\rangle = \sigma_\xi^2\delta(t-t')$ is the autocovariance. To compute the following properties of GWN, without loss of generality, we assume $\mu_\xi = 0$ and $\tau = t' - t$. First we have the autocorrelation

$$\begin{aligned}
R_{\xi\xi}(\tau) &= \frac{\langle \xi(t)\,\xi(t')\rangle}{\sigma_\xi^2} \\
&= \frac{\sigma_\xi^2\delta(t-t')}{\sigma_\xi^2} \\
&= \delta(t'-t) \\
&= \delta(\tau)\,. \qquad (2.40)
\end{aligned}$$

Next the mean-squared displacement (see Sect. 2.6.1) is computed in a straight-forward manner

$$\begin{aligned}
K_\xi(\tau) &= \left\langle [\xi(t+\tau) - \xi(t)]^2 \right\rangle \\
&= \left\langle \xi^2(t+\tau)\right\rangle - 2\left\langle \xi(t+\tau)\xi(t)\right\rangle + \left\langle \xi^2(t)\right\rangle \\
&= \sigma_\xi^2 - 2\sigma_\xi^2\delta(\tau) + \sigma_\xi^2 \\
K_\xi(\tau) &= 2\sigma_\xi^2\left[1 - \delta(\tau)\right]. \qquad (2.41)
\end{aligned}$$

Finally, the power spectral density of GWN is computed via the Wiener-Khintchine theorem and has a trivial value, namely its variance, independent of frequency

$$
\begin{aligned}
S_{\xi\xi}(\omega) &= \sigma_\xi^2 \int_{-\infty}^{\infty} R_{\xi\xi}(\tau) \exp\left(-i\omega\tau\right) \,\mathrm{d}\tau \\
&= \sigma_\xi^2 \int_{-\infty}^{\infty} \delta(\tau) \exp\left(-i\omega\tau\right) \,\mathrm{d}\tau \\
S_{\xi\xi}(\omega) &= \sigma_\xi^2. \qquad (2.42)
\end{aligned}
$$

2.6.3 Ordinary Brownian Motion

The probability density function of ordinary Brownian motion (oBm), also known as the Wiener process, $W(t)$, is also the Gaussian distribution

$$
p_W(x,t) = \frac{1}{\sqrt{4\pi D t}} \exp\left(-\frac{1}{2}\frac{x^2}{2Dt}\right) \qquad (2.43)
$$

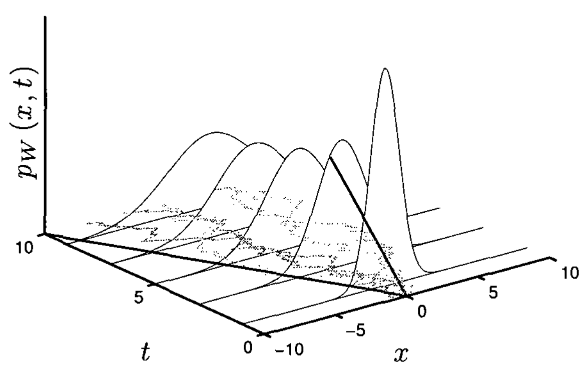

Figure 2.6 – Probability density of the Wiener process shown with five independent realizations. Notice how the variance increases linearly with time.

where the mean is $\mu_W = 0$ and the variance is $\sigma_W^2 = 2Dt$. In other words, the variance of oBm increases linearly with time. Equation (2.43) is a solution of the partial differential equation (PDE)

$$\frac{\partial p_W(x,t)}{\partial t} = D\frac{\partial^2 p_W(x,t)}{\partial x^2} \tag{2.44}$$

which describes the time evolution of the Gaussian probability density which is a pure diffusion process without drift. Some elementary properties of the Wiener process are that it starts at the origin, $W(0) = 0$, and the mean increment is $\langle W(t') - W(t)\rangle = 0$. In general, it may be shown that the auto-covariance is $\langle W(t)\,W(t')\rangle = 2D\min(t,t')$. However, if $t \leqslant t'$

$$\begin{aligned}\langle W(t)\,W(t')\rangle &= \langle [W(t') - W(t) + W(t)]\,W(t)\rangle \\ &= \langle W(t') - W(t)\rangle + \left\langle W^2(t)\right\rangle \\ &= 2Dt.\end{aligned} \tag{2.45}$$

Similarly, we may compute the mean-squared increment of the Wiener process as

$$\begin{aligned}K_W(\tau) &= \left\langle [W(t+\tau) - W(t)]^2\right\rangle \\ &= \left\langle W^2(t+\tau)\right\rangle - 2\,\langle W(t+\tau)W(t)\rangle + \left\langle W^2(t)\right\rangle \\ &= 2D\,(t+\tau) - 4Dt + 2Dt \\ K_W(\tau) &= 2D\tau.\end{aligned} \tag{2.46}$$

Next we focus on the PSD of ordinary Brownian motion. However, since oBm is not WSS because its variance $\sigma_W^2 = 2Dt$ is not constant, the application of the Wiener-Khintchine theorem is invalid. We will revisit this in the next section.

2.6.4 Fractional Brownian Motion

A generalization of oBm is *fractional Brownian motion* (fBm) denoted $W_H(t)$. It is a generalization in that it is self-similar, or exhibits *fractal* properties. By definition, fractals are self-similar across a range of scales and Eq. (2.48) below will describe this property. The scaling exponent, H, also known as the *Hurst exponent*, is defined in the region $0 \leqslant H \leqslant 1$. Ordinary Brownian motion is the special case where $H = 1/2$ which is the boundary of two qualitatively different Brownian motions. Where $0 \leqslant H < 1/2$, fBm is described as negatively correlated, anti-persistent, or sub-diffusive. Conversely, where $1/2 \leqslant H < 1$, fBm is positively correlated, persistent, or super-diffusive. Below is a summary of some important properties of fBm. The derivations of the properties are beyond the scope of this thesis [42], however, the definitions are shown since they are important to later sections. All expressions and properties given below may be referred to the oBm equivalents when $H = 1/2$.

- Initial position, without loss of generality

$$W_H(0) = 0. \tag{2.47}$$

- Time scaling is

$$W_H(ct) = c^H W_H(t). \tag{2.48}$$

- The PDF, similarly derived from the fractional FPE [40] is

$$p_{W_H}(x,t) = \frac{1}{\sqrt{4\pi D t^{2H}}} \exp\left(-\frac{1}{2}\frac{x^2}{2Dt^{2H}}\right). \tag{2.49}$$

- The mean of the fBm process (obtained from Eq. (2.49)) [40, 42] is

$$\mu_{W_H} = 0. \tag{2.50}$$

- The auto-covariance [42] is given by

$$\langle W_H(t) W_H(t')\rangle = D\left(t^{2H} + t'^{2H} - |t-t'|^{2H}\right). \tag{2.51}$$

- The mean-squared displacement [42] is

$$K_{W_H}(\tau) \sim \tau^{2H}. \tag{2.52}$$

- The PSD [21] via the Wigner-Ville spectrum (which is a time-frequency distribution that considers non-stationarity), averaged over time is

$$S_{W_H W_H}(\omega) = \frac{2D}{|\omega|^{2H+1}}. \tag{2.53}$$

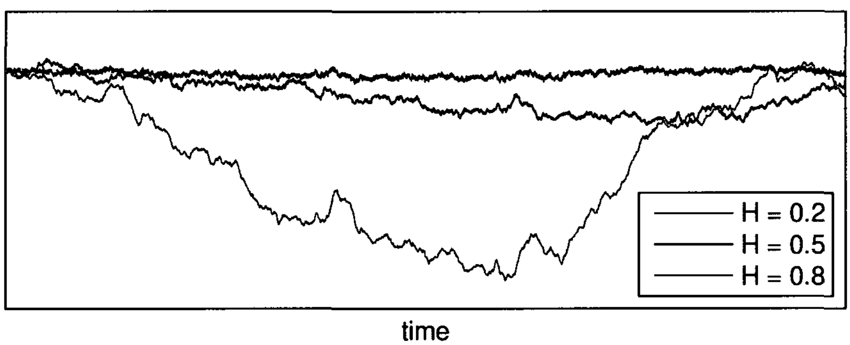

Figure 2.7 – Fractional Brownian motion, $W_H(t)$, for $H = 0.2, 0.5, 0.8$.

In Fig. 2.7, we present three realizations of fBm, one is anti-persistent, another one is ordinary and the last one persistent fBm. All three fBm realizations were produced with a *wavelet*-based algorithm [3], all using the same random Gaussian sequence of numbers. The only difference between all three fBm realizations is the Hurst exponent, as an attempt to show its effect. Notice that the degree of non-stationarity increases with H. This is obvious if one considers the the mean-squared displacement given by Eq. (2.52).

2.7 Stochastic Calculus

Stochastic calculus extends the methods of calculus to stochastic processes such as ordinary Brownian motion (Wiener process). There exists two formulations of stochastic calculus based on two different integrals: Itō, named after Kiyoshi Itō, and Stratonovich, after Ruslan Stratonovich. We consider the Itō formulation of stochastic calculus since it is the most useful for general classes of processes. The general form of a first order autonomous stochastic differential equation (SDE) [36] is

$$\frac{\mathrm{d}x}{\mathrm{d}t} = f\left(x,t\right) + h\left(x,t\right)\xi\left(t\right) \tag{2.54}$$

where x and ξ are functions of t. The noise intensity h, is a function of x, and ξ is a Gaussian white noise process whose mean is $\langle\xi(t)\rangle = 0$ and autocorrelation is $\langle\xi(t)\xi\left(t'\right)\rangle = \delta\left(t-t'\right)$. Then, the Itō interpretation of Eq. (2.54) in differential form is

$$\mathrm{d}X_t = f\left(X_t\right)\,\mathrm{d}t + h\left(X_t\right)\,\mathrm{d}t\xi_t \tag{2.55}$$

where $X_t \equiv x(t)$ by following the convention for variables in stochastic calculus, therefore we also have $\xi_t \equiv \xi(t)$. Defining $\mathrm{d}W_t \equiv \mathrm{d}t\xi_t$, Eq. (2.55) becomes

$$\mathrm{d}X_t = f\left(X_t\right)\,\mathrm{d}t + h\left(X_t\right)\,\mathrm{d}W_t. \tag{2.56}$$

As an example, we choose a simple SDE such as the one-dimensional Langevin equation (ordinary Brownian motion of a particle in a parabolic potential, also known as the Ornstein–Uhlenbeck process)

$$\frac{\mathrm{d}x}{\mathrm{d}t} = -ax + b\xi \tag{2.57}$$

where x is the position, a is the damping term and b is the intensity of the noise. If we consider the Itō formulation of stochastic calculus, then Eq. (2.57) becomes

$$\mathrm{d}X_t = -aX_t\,\mathrm{d}t + b\,\mathrm{d}W_t. \tag{2.58}$$

Equation (2.58) is exactly solvable [36] as follows

$$X_t = X_0 \exp(-at) + b\exp(-at)\int_0^t \exp(as)\,\mathrm{d}W_s \tag{2.59}$$

where $0 \leqslant s \leqslant t$. In this description, stochastic dynamics may be viewed from the perspective of Brownian or Wiener paths, also known as realizations. For given initial conditions, the solution will depend on the random numbers chosen to implement the Wiener process, *i.e.*, on the Wiener path. Comparisons to experiment are done by averaging trajectory statistics, such as solution means and moments, across multiple realizations. However, instead of treating stochastic dynamics from the path point of view, we may equivalently describe them with an evolving probability density. Such an approach is given by the Fokker–Planck equation (FPE) (or the forward Kolmogorov equation) (2.60)

$$\frac{\partial}{\partial t}p(x,t) = -\frac{\partial}{\partial x}\{D_1(x,t)p(x,t)\} + \frac{\partial^2}{\partial x^2}\{D_2(x,t)p(x,t)\} \tag{2.60}$$

where $p(x,t)$ is the probability density, $D_1(x,t)$ is the drift function and $D_2(x,t)$ is the diffusion function. Recall Eq. (2.44), which is a linear case of the FPE, more specifically, one where the drift and diffusion functions are $D_1 = 0$ and $D_2 = D$, respectively. It also has an analytic solution given by Eq. (2.43). It is possible to transform an Itō SDE into a FPE [35] by using $D_1(x,t) = f(x,t)$ and $D_2(x,t) = \frac{1}{2}g(x,t)$ (this is easily generalizable for an N-dimensional system). Let us use Eq. (2.58) as an example

$$\frac{\partial p(x,t)}{\partial t} = -a\frac{\partial p(x,t)}{\partial x} + \frac{b}{2}\frac{\partial^2 p(x,t)}{\partial x^2} \tag{2.61}$$

where $D_1(x,t) = a$ and $D_2(x,t) = b/2$. The drift and diffusion functions, respectively $D_1(x,t)$ and $D_2(x,t)$, may be placed in front of the partial derivatives since they are homogenous with respect to x. While Eq. (2.61) is solvable, generally for nonlinear SDEs the FPE is not exactly solvable, even for the steady solutions $p(x,t=\infty)$.

2.8 Nonlinear Time Series Analysis

2.8.1 Phase Space Reconstruction

The first recurrence plots (RP) [18] were introduced over two decades ago. This method makes use of a dynamical technique known as phase space reconstruction (PSR) (or attractor reconstruction) [2] which we first describe. The concept of PSR is quite simple: deterministic dynamical systems represented as $\dot{\mathbf{x}}(t) = f(\mathbf{x}(t))$, linear or nonlinear, and of any finite dimension, may be reconstructed from a single dynamical observable. Stochastic systems may use PSR, albeit the reconstruction will be degraded. A one-dimensional time series, obtained at times, $t = i\Delta t$ which gives a set of state values $\{x_i\}$ where $i = 1, \ldots, N$ can be used to reconstruct the entire set of state variables by using Taken's embedding theorem [73]. The idea is that vectors made up of the same scalar variable but sampled at different time can be used:

$$\mathbf{x}_i = \begin{bmatrix} x_i & x_{i+\tau} & \cdots & x_{i+(d-1)\tau} \end{bmatrix}^T \tag{2.62}$$

where $\mathbf{x}_i \in \mathbb{R}^d$, $i = 1, \ldots, M$, $M = N - (d-1)\,\tau$, d is the embedding dimension, and τ is the lag. The optimal lag, τ, is determined from the first minimum of the average mutual information (AMI) of the time series $\{x_i\}$ [23, 1]. In the most general case, AMI is needed since it is a nonlinear measure of correlation between a variable and a time-delayed version of the same variable. The dimension d is chosen by observing the percentage of false nearest neighbors (FNN) as a function of embedding dimension. Trajectories cannot intersect in phase space since trajectories have a unique future for each phase space point. However, if the embedding dimension is too low intersections can arise within the embedding space, causing false nearest neighbors. With increasing dimension, the percentage of FNN decays, and eventually saturates at some level. The minimum dimension which has this percentage is usually chosen as d. Thus, with these values for τ and d, PSR is performed via Eq. (2.62) and we may proceed to the RP.

2.8.2 Recurrence Quantification Analysis

Due to the stochastic nature of postural sway data, microstates are not as predictable as a completely deterministic system even if the statistics (macrostates) are known. Yet, small features in the time series may eventually repeat themselves even though such systems do not display strong periodicity. In other words, there could be some underlying determinism to some degree. With relatively high noise levels, the more traditional methods of Fourier analysis do not perform as well at identifying time series frequency components. Fourier analysis for the PSD only gives reliable results when averaging over realizations since errors on estimates are large [58]. Further, the PSD discards phase information.

To find recurrent structures in the reconstructed phase space, we use the recurrence plot [48], $\mathbf{R}_{i,j}$ which is a square matrix representing recurrences of $\mathbf{x}_i$ and $\mathbf{x}_j$ within some neighborhood given by a Euclidean d-dimensional hypersphere with radius ϵ. If $\mathbf{x}_j$ is inside the sphere centered at $\mathbf{x}_i$, then $\mathbf{R}_{i,j} = 1$, otherwise, 0. In mathematical terms

$$\mathbf{R}_{i,j} = H\left(\epsilon - \|\mathbf{x}_i - \mathbf{x}_j\|\right) \tag{2.63}$$

where H is the Heaviside function and $\|.\|$ denotes the Euclidean distance (L_2-norm). Figures 2.8, 2.9 and 2.10 explain the variety of recurrence plots for their respective systems.

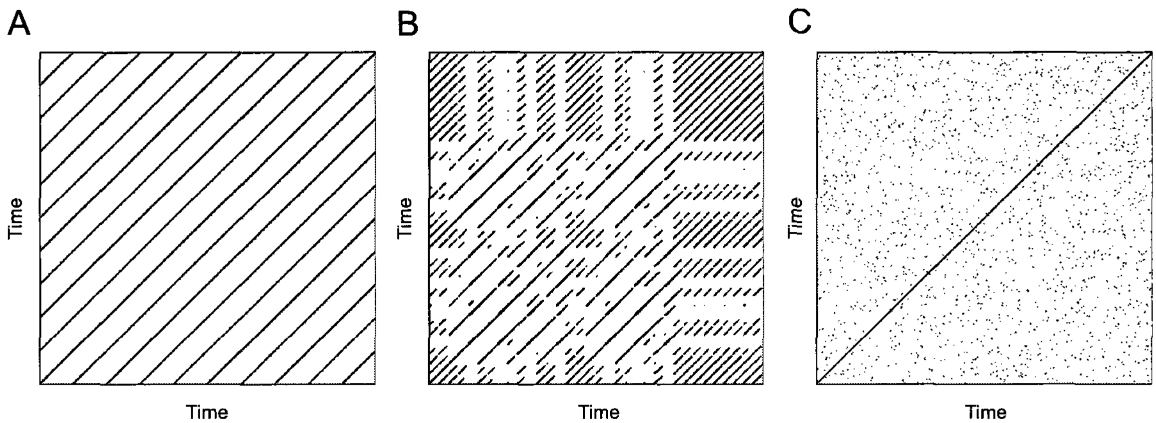

Figure 2.8 – Recurrence plots of known dynamics. (a) Periodic motion with one frequency, (b) the chaotic Rössler system, and (c) uniformly distributed noise [48].

From the RP matrix, many dynamical measures may be computed [88, 80, 77, 49, 44, 48]. Among these measures, recurrence rate (RR) is the ratio of recurrent elements in $\mathbf{R}_{i,j}$ to total elements in $\mathbf{R}_{i,j}$ (excluding $\mathbf{R}_{i=j}$)

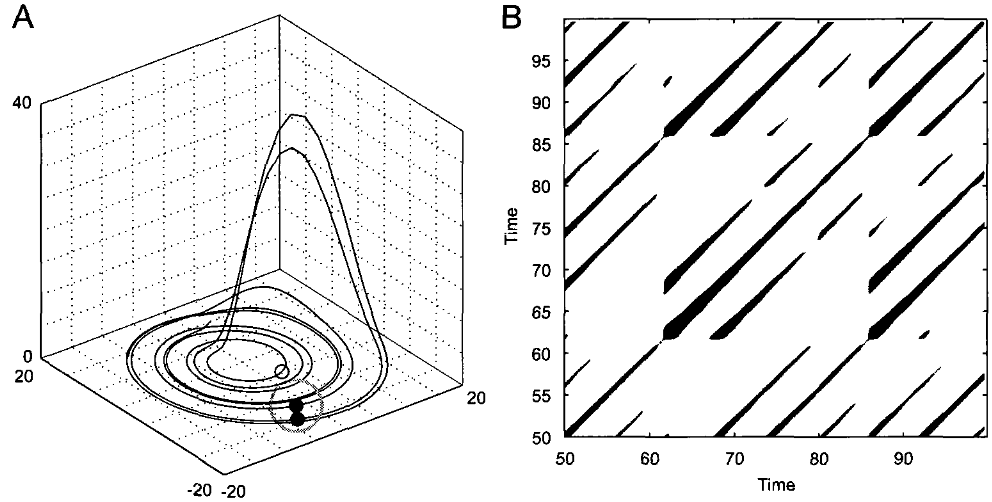

Figure 2.9 – Chaotic Rössler system in 3 dimensions and its recurrence plot. (a) Segment of the phase space trajectory of the Rössler system, with $a = 0.15$, $b = 0.20$, $c = 10$, visualized by using its three components and (b) its corresponding recurrence plot (a zoomed portion). A phase space vector at j which falls into the neighborhood (grey circle in (a)) of a given phase space vector at i is considered as a recurrence point (black point on the trajectory in (a)). This is marked with a black point in the RP at the position (i, j). A phase space vector outside the neighborhood (empty circle in (a)) leads to a white point in the RP. The radius of the neighborhood for the RP is chosen here as $\epsilon = 5$; L_2-norm is used [48].

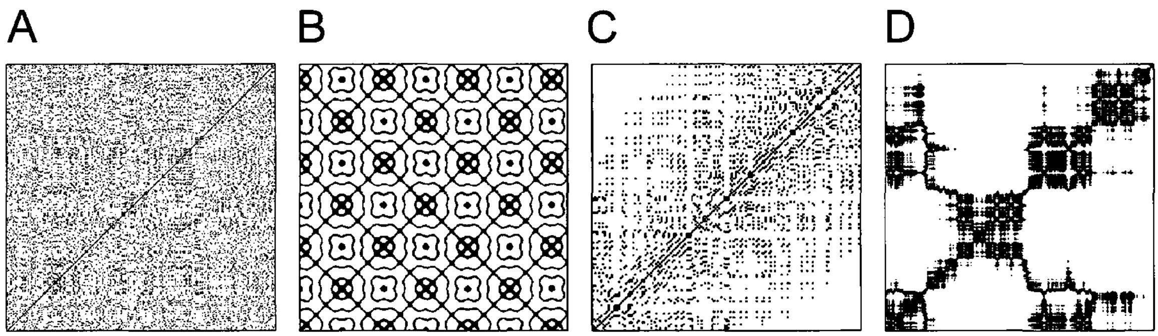

Figure 2.10 – Characteristic typology of recurrence plots. (a) Homogeneous (uniformly distributed white noise), (b) periodic (super-positioned harmonic oscillations), (c) drift (logistic map corrupted with a linearly increasing term $x_{i+1} = 4x_i(1 - x_i) + 0.01i$ (d) disrupted (Brownian motion). These examples illustrate how different RPs can be. The used data have the length 400 (a,b,d) and 150 (c), respectively; RP parameters are $d = 1$, $\epsilon = 0.2$ (a, c, d) and $d = 4$, $\tau = 9$, $\epsilon = 0.4$ (b); L_2-norm. [48].

$$RR = \frac{2}{M\,(M-1)} \sum_{i=1}^{M} \sum_{j=i+1}^{M} \mathbf{R}_{i,j}. \tag{2.64}$$

2.8.3 Largest Lyapunov Exponent

The largest Lyapunov exponent (LLE), λ_1, characterizes the average rate of divergence of trajectories in a dynamical system. If the system is known and assuming its global behavior is not divergent (*i.e.*, motion is confined to a bounded part of phase space), λ_1 is computed by letting two trajectories of the system initially begin near one another in phase space. As the system moves forward in time, and if the system is chaotic, the two trajectories will diverge exponentially from one another until they have reached the characteristic size of the attractor. The divergence is given as

$$\mathrm{div}(t) = C \exp\left(\lambda_1 t\right) \tag{2.65}$$

where C is a constant.

Therefore, the average logarithmic divergence, $\langle \ln\left(\mathrm{div}\right) \rangle$, plotted against time will have a positive linear slope from time $t \approx 0$ to $t = t_c$ (scaling region), where t_c denotes the time when $\langle \ln\left(\mathrm{div}\right) \rangle$ plateaus (*i.e.*, takes on a mean slope of zero), due to the trajectories reaching the bounds of the attractor. For example, the Lorenz equations are given by

$$\begin{cases} \dot{x} = a\,(y - x) \\ \dot{y} = x\,(b - z) - y \\ \dot{z} = xy - cz \end{cases} \tag{2.66}$$

where a, b, c are constants. If we choose a, b, c such that the system is chaotic, then it has an attractor as shown in Fig. 2.11. The system's trajectory moves from one lobe to the other in a 'twisted' figure-8. Yet, the trajectory never crosses itself since it is nonperiodic.

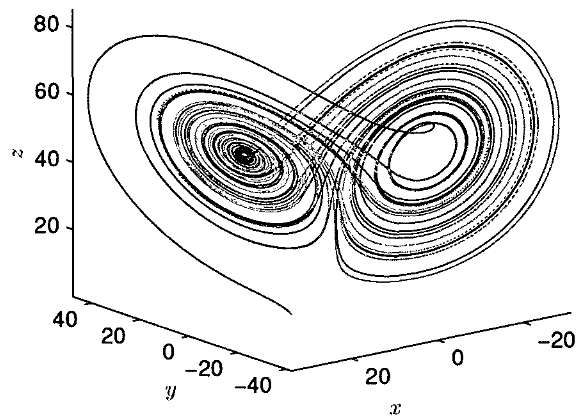

Figure 2.11 – Lorenz system in chaotic regime (from Eq. (2.66)) where $a = 16$, $b = 45.92$ and $c = 4$, shown for 50 seconds. Color indicates time evolution where it begins as black, to red and ends as yellow.

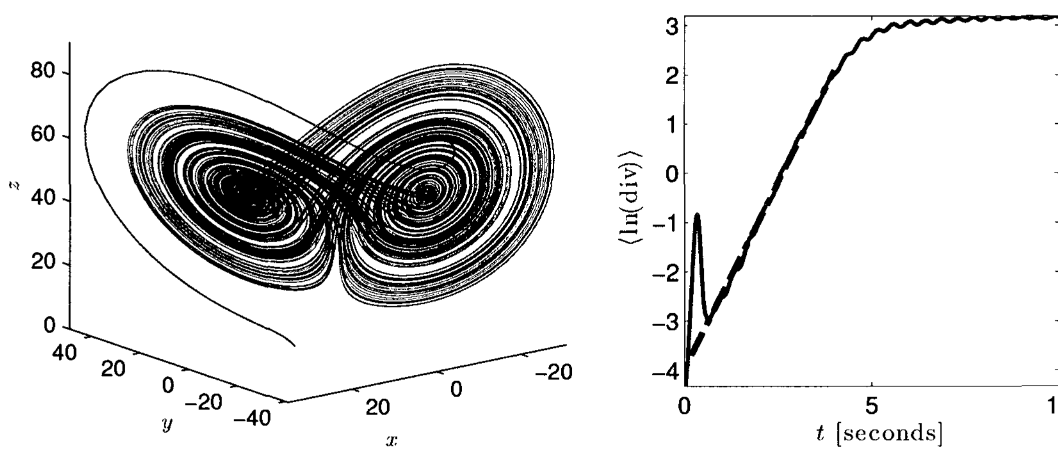

(a) Two chaotic Lorenz attractors.

(b) Exponential divergence of the chaotic Lorenz attractor.

Figure 2.12 – Exponential divergence of the chaotic Lorenz attractor. (a) Two different trajectories of the Lorenz attractor (one blue, the other red) beginning very close to each other yet occupying different areas of phase space. (b) The blue line displays $\langle \ln(\text{div}) \rangle$ and the slope of the black dashed-dotted line is obtained by the linear regression of $\langle \ln(\text{div}) \rangle$ from $t = 0.5$ to $t_c = 4$ seconds (the "scaling region"). It is here $\lambda_1 \approx 1.52$.

If the system is unknown and we are given only experimental data, the computation is significantly more involved; nevertheless, the concept is similar. After completing PSR, one may use an algorithm [66] to compute λ_1. This is valid insofar as the data are relatively long (many data points), the dimension of the attractor is relatively low, and there must be low noise. However, in general, as the embedding dimension increases, λ_1 decreases until it becomes constant, for larger dimensions. The dimension at which λ_1 seems to reach a constant is the proper embedding dimension as the dynamics have completely unfolded.

Due to their high dimensionality, the divergence of stochastic systems cannot be computed by the method reported in [66]. As they have reported, the scaling region becomes larger and generates a λ_1 that decreases as the embedding dimension increases. This may be understood intuitively since stochastic systems are simply random fluctuations, and similarly to the probabilities of their trajectories which may go one way or another equally, so does the divergence, whereby the mean is close to zero. Stochastic systems do not diverge exponentially but more diffusionally. Furthermore, Lyapunov calculations cannot reveal the underlying determinism if noise is moderate or strong.

In the next chapter we will describe our experiment and model of delayed visual feedback based on the work described in Sect. 2.1.3.

Chapter 3

Stochastic two delay-differential model of delayed visual feedback effects on postural dynamics

by

Jason Boulet[1,2,*], Ramesh Balasubramaniam[2,3], Andreas Daffertshofer[4] and André Longtin[1,2]

[1]*Department of Physics and* [2]*Centre for Neural Dynamics, University of Ottawa, Ottawa, Ontario K1N 6N5, Canada*

[3]*Department of Kinesiology, McMaster University, Hamilton, Ontario L8S 4L8, Canada*

[4]*Research Institute MOVE, VU University Amsterdam, van der Boechorststraat 9, 1081BT Amsterdam, The Netherlands*

[*]*corresponding author:* `jboul079@uottawa.ca`

3.1 Abstract

We report on experiments and modeling involving the 'visuo-postural control loop' in upright stance. We experimentally manipulated an artificial delay to the visual feedback during standing, presented at delays ranging from zero to one second in increments of 250 milliseconds. Using stochastic delay differential equations, we explicitly modeled the center-of-pressure (COP) and center-of-mass (COM) dynamics with two independent delay terms for vision and proprioception. A novel 'drifting fixed point' hypothesis was used to describe the fluctuations of the COM with the COP being modeled as a faster, corrective process of the COM. The model was in good agreement with the data in terms of probability density functions, power spectral densities, short and long-term correlations (Hurst exponents) as well the critical time between the two ranges.

3.2 Introduction

Delays are an important feature of any biological control system. The feed forward propagation of neural activity from sensors to the central nervous system, as well as from the central nervous system to muscles, can involve delays of hundreds of milliseconds. Delays complicate all control tasks involving sensors and effectors in any feedback configuration. This is because the controller, even if it is distributed, typically has a delayed response to errors detected between the desired and current states of the system. The study of such control systems with one or many feedback loops, and their robustness to sources of random fluctuations, is receiving ever more attention [71].

The postural control system is a canonical example of a neurological control system. Understanding its function is particularly important in the clinical realm, *e.g.*, in the context of aging. In fact, the control of posture degrades as we get older, and an understanding of the components of this control system and how they change with age is of paramount importance. In addition to delays in visual processing, there are delays on the order of hundreds of milliseconds in the purely proprioceptive control of posture based on mediated feedback from the muscles that apply torque to the ankle and other joints of the lower limb. Visual cues are also important for stabilizing what is essentially an inverted (multi-segmented) 'pendulum', and this visual processing also involves large delays.

It is essential to be able to perturb the healthy postural control system to gain a better understanding of its function, and of its dysfunction under pathological conditions. While it is not readily possible to extend or shorten the proprioceptive delay, it is possible to extend the visual delay, as has been done in two recent studies of posture control [67, 79]. This same strategy has also been used to study finger position control [25]. It is known that symmetric systems with an unstable equilibrium, such as the inverted pendulum, can exhibit many different behaviors as parameters are changed. This is because their dynamics are organized around a co-dimension two bifurcation known as a Takens-Bogdanov bifurcation (in its symmetric version; see [61]), which arises when a pitchfork bifurcation meets a Hopf bifurcation. That same work showed how chaos may develop as non-linearities are changed, adding a potential deterministic source of variability in the associated control problems. The addition of a second delay, as we do here to account for visual feedback, brings us into unexplored dynamical territory.

In this paper, we first report new experimental measurements of posture control in healthy humans in which the visual delay is artificially increased by as much as one second. The variable that was measured and treated to extensive analysis was the center-of-pressure (COP) recorded using a force plate. We computed the probability densities of the fluctuations in anterio-posterior (AP) deviations from an upright position, as well as their spectral properties and Hurst exponents across delay conditions. This goes beyond [79], which concentrated on how the low- and high-frequency components of the sway behaved as a function of delay. Additionally, we summarize a novel dynamical model of postural control mediated by proprioceptive and visual feedback, which is based on the inverted pendulum. The model incorporates thus two delays associated with the corresponding control loops: proprioception and vision. The model also includes noise, which appears essential to simulate the 'random walk' executed by the COP. More noise is added to the slowly and randomly wandering fluctuation of the equilibrium position of the model to replicate the ongoing corrections to the position as the body shifts position during postural tasks. By making these fluctuations state-dependent, a better qualitative agreement between model and data is found. Postural fluctuations are known to exhibit different short and long-term correlations [13]. Here, our model was thus used to explore the stability of the system as a function of its delays, especially in terms of the cut-off between regimes of short and long-range correlations.

Numerous models of postural dynamics have been proposed over the past two decades. [10] used an elastic pinned polymer, modeled with a stochastic partial differential equation. Their model accounted for the characteristic mean-squared displacement and correlation functions typically seen in postural sway; however, it lacked an explicit control mechanism, which is our primary interest here. [34] used high order linear and optimal control theory models to estimate postural states. Higher order models require many parameters and thus are very complex. These models make use of Kalman filters and therefore, states are evaluated instantaneously, lacking any minimal processing delay. Moreover, [22] adopted the so-called vector-integration-to-end-point model to describe the COP dynamics, which was originally proposed by [5] to explain the emergence of typical properties of reaching such as a speed-accuracy trade-off and a bell-shaped velocity profile. They identified the COP as to-be-controlled (or to-be-minimized) difference between actual position and the target position (in quiet stance the origin) and implement the distinction between short- and long-term correlation by letting the drift coefficient of its dynamics depend on its correlation function (which led to a super-diffusive short-term regime).

A simpler approach to modeling postural control has been based on the dynamics of the inverted pendulum. The validity of the inverted pendulum as a model for upright quiet stance has been studied by [24, 83], showing the relationship between COP and the center-of-mass (COM). [19, 53] have extended this approach to include noise, *i.e.*, they treated the system as a stochastic delay differential equation. In both cases, control was delayed, and discontinuous since it was dependent on a constant threshold of 'displacement'. This produces co-existing oscillations around each threshold, which were not evident in the data, but the more realistic global fluctuations due to noise-induced switches had Hurst exponents that agreed with experiment. In the same context, a simple continuous control model was proposed by [86]. More recently, [71] has worked on delay effects in the human sensory system while balancing. More recent developments show stabilizing effects of noise [51], [7]. The analysis of stochastic delay differential equations in the context of posture control may benefit from techniques such as small delay approximations [27], or two-state approximations if and when bistability is present [78].

To summarize, we focus on a two-delay stochastic differential equation to understand how generic features of postural sway are related to several system parameters. Apart from providing a proper testing ground for the potential impact of vision on posture control, this approach allows for probing more deeply the boundary between short-term, persistent (non-corrective) and more long-term, anti-persistent (corrective) fluctuations, *e.g.*, determining how it depends on delays in the control loops and on the noise sources. Section 3.3 describes the experimental methods (data acquisition and analysis). Section 3.4 presents the empirical findings as a function of delay conditions: time series, standard deviations, power spectra, probability density, and Hurst exponent estimates. Finally, the model is developed and analyzed in Sect. 3.5 and we conclude in Sect. 3.6.

3.3 Methods

3.3.1 Experiment

Eight males and six females aged 25.6 ± 3.0 years with masses and heights of 72 ± 11 kg and 173 ± 9 cm, respectively, participated in the experiment approved by the University of Ottawa ethics review board. They signed an informed consent prior to participation.

Participants had no cognitive or physical impairments. A participant's task was to stand on a force plate (Advanced Mechanical Technology, Inc., AMTI) with feet at a comfortable separation as straight as possible with hands at their side in an upright stance. For visual conditions they looked at a 19 inch display, which showed a black background and a red dot at the center representing the fixed target. A smaller white dot represented their COP and was displayed in real-time or with additional visual delay under experimental control. The experiment consisted of six conditions: eyes closed, and eyes open with delayed visual feedback of 0, 250, 500, 750, and 1000 milliseconds (ms). There were five trials for each condition, with a total of thirty trials per subject. Each trial lasted 120 seconds.

All footwear other than ones with elevated heels or ankle-constrictions were allowed. Participants stood on the same area on the force plate for all trials. Markers were placed on the force plate to remember foot positions from trial to trial. Initial foot positions were determined before the first trial by finding the area on the force plate where participants stood upright and maximized the overlap of their COP with the target with minimal effort. Previous studies [79, 67] used instead the mean position of the COP's first second of the trial as the target. The problem with that approach is that one second may not be enough time for initial COP transients to settle and consequently a less 'balanced' target might be used. That is, our technique aimed to find a better centered subject-specific target.

3.3.2 Data analysis

Force plate data was sampled at 1000 Hz for AP and medio-lateral (ML) components. We will only consider the AP data for this article. These data were down-sampled offline to 100 Hz for analysis in Matlab (The Mathworks, Natick, MA). Afterwards, 4 seconds at the beginning and 1 second at the end were removed to discard transients for a total of 115 seconds. Probability density functions (PDF) were computed on the first three consecutive 30 second blocks, each with its mean removed. For every one of the six conditions, the PDFs were averaged over the 3 blocks for each subject, then across trials and finally across all participants. Power spectral densities (PSD) were computed similarly via the Welch periodogram function with a non-overlapping Hamming window. Standard deviations were computed with the same partitioning. Mean-squared displacements were computed in 10 second blocks and averaged over 10 blocks per trial. They were averaged over all trials per participant and then over participants. A similar treatment of mean-squared displacement was given by [12]. The first quantity estimated from the mean-squared displacement was the critical time τ_c defined by the first time that the Hurst exponent crosses $H = 0.5$. We note that this also defines the boundary between the aforementioned two regimes of persistent and anti-persistent behavior. A linear regression was then applied to the log-log of the mean-squared displacement $K(\tau)$ vs. lag τ on $[0.1, \tau_c]$ and $[\tau_c, 10]$ seconds, where the slopes of the fit were divided by 2 to give H_s and H_l respectively. The slopes were divided by 2 for fractional Brownian motion (fBm) since, $\left\langle [\Delta r(\tau)]^2 \right\rangle \propto \tau^{2H}$ [43, 55].

3.4 Results

For the sake of legibility, results for the data and model are presented simultaneously in the figures below, even though the model will only be presented in Sect. 3.5. First, let us refer to Fig. 3.1, which shows the COP for (a) no-vision, (b) 0 ms delay and (c) 750 ms delay, where all time series were mean-centered. The condition with no-vision was noticeably less stationary than the conditions with visual feedback, which suggested that visual feedback acted as an additional stabilizing, and likely, a corrective mechanism. By and large, Fig. 3.2 confirms this observation by displaying the mean (across participants) standard deviation of the COP time series for all experimental conditions; error bars represent the standard deviation over all participants and trials. It is interesting to note that, within error, the standard deviation varied little across visual delays.

To disentangle effects in different time scales, Fig. 3.3 presents the mean power spec-

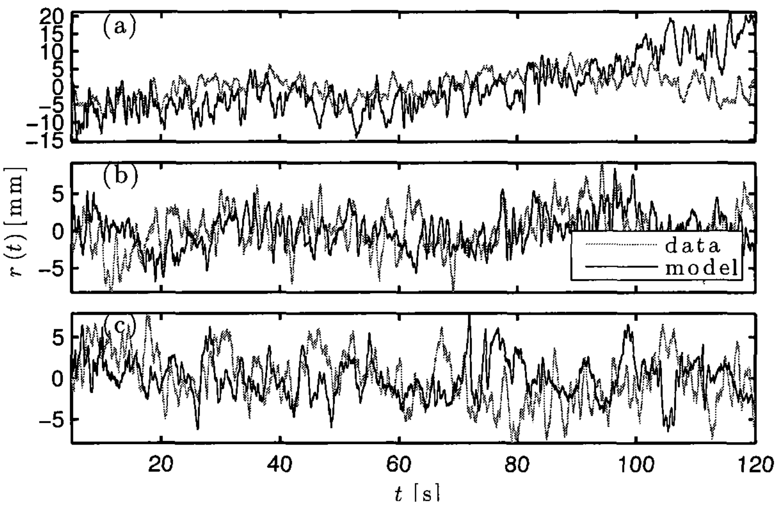

Figure 3.1 – COP time series for (a) No-vision, (b) 0 ms delay and (c) 750 ms delay.

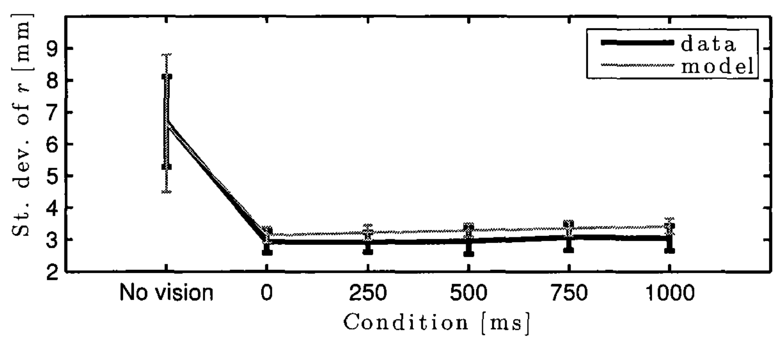

Figure 3.2 – Standard deviation of COP time series for all conditions.

tral density PSD, $S_{rr}(f)$, averaged over participants for the same conditions as in Fig. 3.1. There was more power at lower frequencies for the no-vision condition, since there appeared to be a slow, drift-like process; *cf.* also Fig. 3.1. A feature seen across all conditions was the 'elbow' in the middle of the curve, which divided the spectrum into two $1/f^{\alpha}$-type regimes. This is characteristic of a multi-fractal [43]. If we proceed by assuming that the no-vision condition has more drift, as suggested by the time series and the PSD, then its PDF, P_r, should have a relatively larger variance. Fig. 3.4 clearly demonstrates this fact, whereas the two PDFs for visual feedback conditions were approximately the same regardless of delays (only two are shown here). We then computed

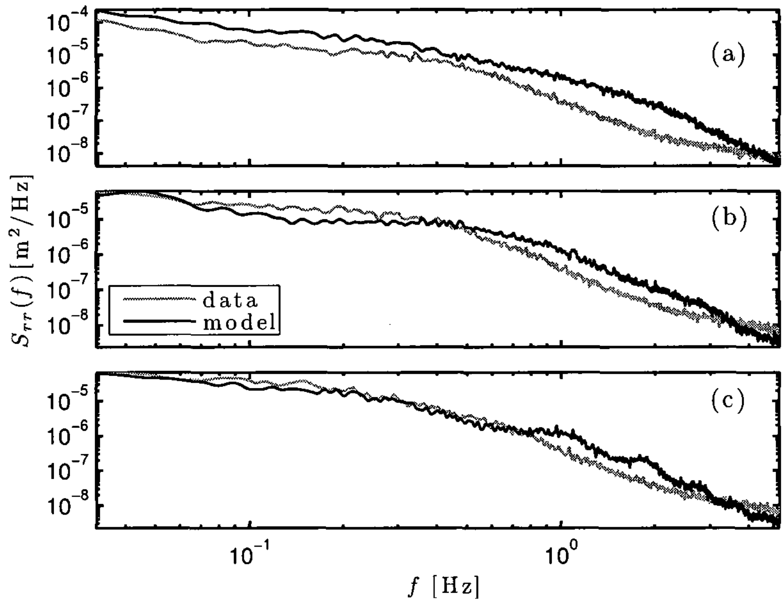

Figure 3.3 – PSDs for (a) No-vision, (b) 0 ms delay and (c) 750 ms delay.

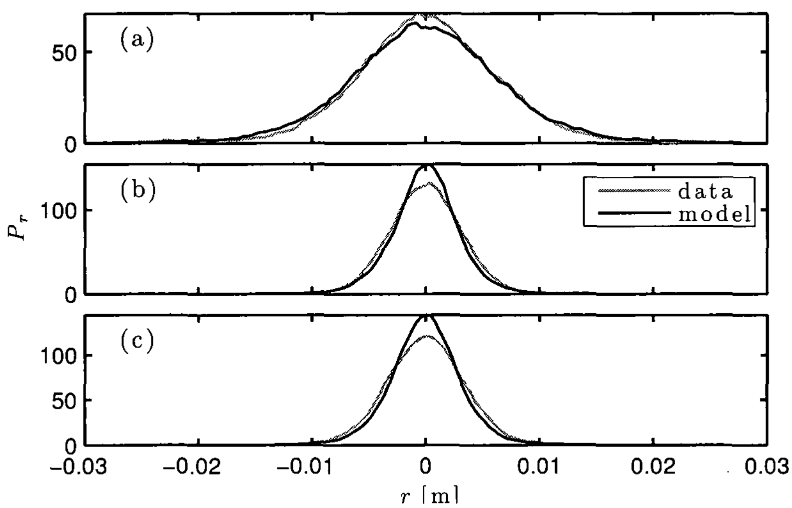

Figure 3.4 – PDFs for (a) No-vision, (b) 0 ms delay and (c) 750 ms delay.

the mean-squared displacement $K(\tau)$, and from it, the short- and long-term correlations quantified via the corresponding Hurst exponents, H_s and H_l, as well as the critical time, τ_c. We note that for ordinary Brownian motion (oBm) $H = 0.5$ holds, since $\left\langle [\Delta r(\tau)]^2 \right\rangle \propto \tau \left(\propto \tau^{2H}\right)$. Fig. 3.5 shows a schematic representation of the calculation of these quantities. Not only did we see mutli-fractal behavior in the PSD, but in the mean-squared displacement as well. Therefore, it can be detected from the time and frequency domains. Fig. 3.6 shows the average values of H_s, H_l and τ_c across all participants. In

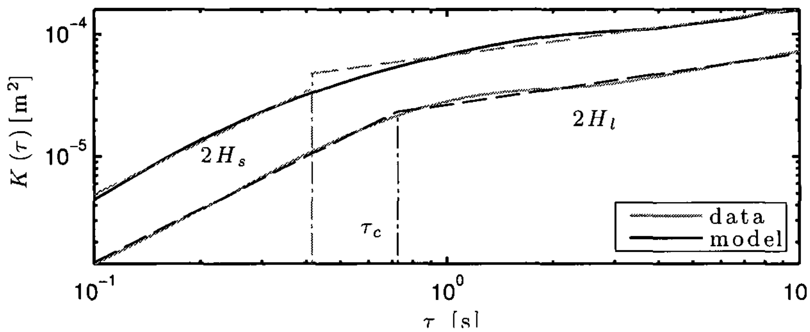

Figure 3.5 – Mean-squared displacement for the no-vision condition.

fact, the Hurst exponents agreed with previous studies; *i.e.*, H_s is between 0.5 and 1 and the range of H_l is from 0 to 0.5 for all conditions. Collins and De Luca [14] have shown a significant difference between eyes open and eyes closed conditions for H_l. Similarly, Fig. 3.6 reveals a clear difference in the long-term Hurst exponent for the no-vision and visual feedback conditions. The critical times, however, were the quantities of most interest since they define the boundaries of distinct control regimes [12]. Across all conditions, even without vision, the critical times are ≈ 0.5 seconds. Therefore, it appears that the artificial visual delay was not a major contributor to the value of τ_c.

3.5 Model

3.5.1 Inverted pendulum dynamics

In the models [86, 19] for postural sway along the AP direction, the body is likened to an overdamped, inverted pendulum, which is considered as the 'plant'; see also below and, *e.g.*, [81]. From Fig. 3.7, the inverted pendulum is a rigid mass-less rod connected to a point of mass m, and L is the distance from the origin to the COM. From this, one can obtain the moment of inertia $I = mL^2$. There also exists a viscous damping force at the

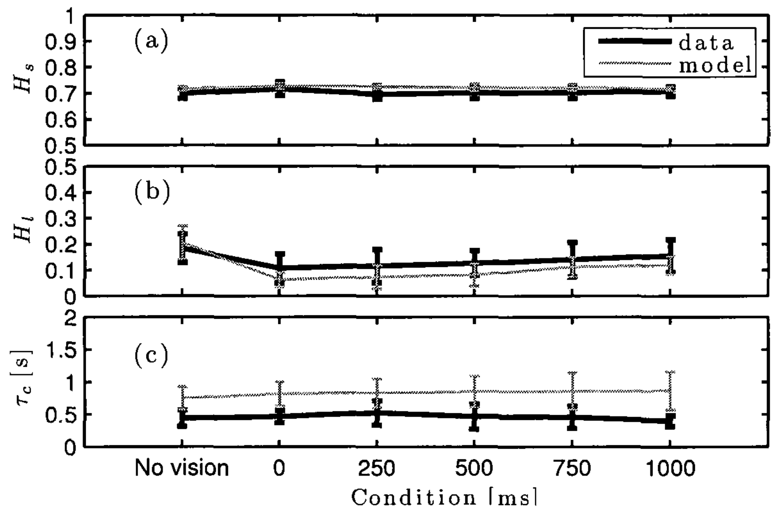

Figure 3.6 – (a) Short- H_s and (b) long-range Hurst exponents H_l and (c) critical times.

origin (not shown) proportional to the angular velocity. In combination, this leads to an equation for rotational equilibrium in the yz-plane where θ is the angle in that plane measured from the vertical direction

$$I\ddot{\theta} + \beta\dot{\theta} - mgL\sin\theta = 0. \tag{3.1}$$

One can simplify Eq. (3.1) by assuming that the sway angle θ does not deviate any

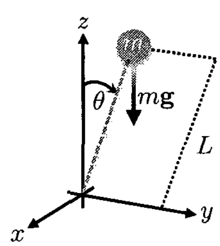

Figure 3.7 – Inverted pendulum free-body diagram where x represents ML and y, AP.

greater than 5 degrees, rendering a small angle approximation to first order from the Taylor expansion proper: $\sin\theta \approx \theta + \mathcal{O}(\theta^3)$, which yields

$$I\ddot{\theta} + \beta\dot{\theta} - mgL\theta = 0. \tag{3.2}$$

As indicated above, [81] stated that postural sway is overdamped for healthy participants with eyes open that here provided the condition $\beta\dot{\theta} \gg I\ddot{\theta}$. Because of $\theta = y/L$, Eq. (3.2) reduces to $\dot{y} = mgLy/\beta$. Henceforth, we will replace y with r and $\varepsilon = mgL/\beta$ and write

$$\dot{r} = \varepsilon r. \tag{3.3}$$

Since we were restricting the dynamics to a first order system, the potential function can be given as $V(r) = ar^2$, that is, the only stable position can be $r = 0$, otherwise r diverges. This type of stability may generally be referred to as unstable equilibrium where any perturbation from the equilibrium will move the system away from this point. In terms of the inverted pendulum, the only stable state refers to the completely upright state.

3.5.2 Noise

Postural perturbations for quiet standing is traditionally modeled with Gaussian white noise denoted as $\xi(t)$, which is a wide sense stationary process. This means that the first and seconds moments remain constant over time. Mathematically, its mean is $\langle\xi(t)\rangle = 0$ and autocorrelation function is $R_{\xi\xi}(t-t') = \langle\xi(t)\xi(t')\rangle = \delta(t-t')$, whereas the PSD is $S_{\xi\xi}(f) = 1$; the latter follows via the Wiener-Khintchine relation. To avoid confusion with other works, it should be noted that in this paper, all Gaussian white noise processes have a variance equal to 1.

3.5.3 Feedback

The previously described inverted pendulum dynamics is intrinsically unstable at its fixed point. However, when observed experimentally, quiet standing appears fairly stable, and suggests that there must be a stabilizing mechanism, which exists to counteract this phenomenon [19]. In the framework of continuous stochastic delay equations (see also

[86]), a self-stabilizing model should be of the form

$$\dot{r} = \varepsilon r + f(r) + \sqrt{2D_r}\xi_r \tag{3.4}$$

where D_r is a one-dimensional diffusion constant. In the same context, for eyes open, [86] proposed that the feedback function $f(r)$ should take the form of a smoothed on-off switch at some delayed time τ_{prop} for proprioception at the ankles, and therefore, Eq. (3.4) becomes

$$\dot{r} = \varepsilon r - \kappa \tanh\left[r\left(t - \tau_{\text{prop}}\right)/\rho\right] + \sqrt{2D_r}\xi_r \tag{3.5}$$

where κ is the strength of the proprioceptive feedback and ρ is a characteristic length scale (which we set equal to 1 m). Since $r \ll \rho$, we may linearize Eq. (3.5) about its fixed point $r^* = 0$, which gives

$$\dot{r} = \varepsilon r - \kappa r\left(t - \tau_{\text{prop}}\right) + \sqrt{2D_r}\xi_r. \tag{3.6}$$

Redmond *et al.* [61] showed that the deterministic part of such systems have a Takens-Bogdanov bifurcation as their core organising center. In addition, the stationary solution regime of Eq. (3.6) can be described in terms of ε, κ and τ_{prop} (where $D_r \geqslant 0$) [37] where all parameters are positive (for the remainder of the paper as well) and $\kappa > \varepsilon$ as follows:

$$\tau_{\text{prop}} < \tau_{\text{crit}} = \frac{\cos^{-1}(\varepsilon/\kappa)}{\sqrt{\kappa^2 - \varepsilon^2}}. \tag{3.7}$$

If this condition is not satisfied, a sub- or supercritical Hopf bifurcation will appear with angular frequency $\omega_{\text{crit}} = \sqrt{\kappa^2 - \varepsilon^2}$ [41]. In fact, since such oscillations are not manifested in the time series or PSD of the experimental data, it is likely that this condition is satisfied. Equation (3.6) however, cannot reproduce both eyes-closed and eyes-open conditions since the eyes-closed condition is non-stationary due to a slow drift process as seen from the time series and PSD in Figs. 3.2 (a) and 3.3 (a). To explain this drift process, we turn to Zatsiorsky and Duarte [87] who make reference to a migrating reference point (rambling), which we shall refer to dynamically as a 'drifting fixed point'. This drifting fixed point may be modeled as an independent Wiener process, which is also a position, by adding it onto Eq. (3.6)

$$\dot{r} = \varepsilon r - \kappa r\left(t - \tau_{\text{prop}}\right) + \sqrt{2D_r}\xi_r + s \tag{3.8}$$

$$\dot{s} = \sqrt{2D_s}\xi_s \tag{3.9}$$

where D_s is a second diffusion constant and $\xi_r(t)$ and $\xi_s(t)$ are independent Gaussian white noise processes.

We further wished to include visual feedback to explain both eyes closed and eyes open data in a single model. Comparing Figs. 3.2, 3.3 and 3.4, we noticed that the drift process seemed negligible for eyes open compared to the case of eyes closed. Hence, we proposed, as earlier, to model visual feedback similarly to the proprioceptive feedback. The visual feedback, however, must be corrective, *i.e.*, directed towards the origin. Including this as part of Eq. (3.9) to minimize drift results in a doubly-delayed Langevin equation. This inclusion reduces power in the PSD at low drift frequencies, and the variance of the PDF decreases, as seen experimentally. Equation (3.9) then becomes

$$\dot{s} = -\gamma \tanh\left[r\left(t - \tau_{\text{vis}}\right)\right] + \sqrt{2D_s}\xi_s. \tag{3.10}$$

We note that this equation is still valid for eyes closed since we may simply choose $\gamma = 0$. As for the visual delay τ_{vis}, it is composed of two parts: an intrinsic minimal visual delay, and the experimental perturbative delay which is 0, 250, 500, 750 or 1000 ms. For all simulations we used 200 ms for the minimum visual processing delay. A further reduction can be made to Eq. (3.10), again by the linearization of the hyperbolic tangent function using the similar argument *i.e.*, $s \ll 1$ m, and upon redefining $a_r \equiv \sqrt{2D_r}$ and $a_s \equiv \sqrt{2D_s}$

the final form of the model is

$$\dot{r} = \varepsilon r - \kappa r\left(t - \tau_{\text{prop}}\right) + a_r\xi_r + s \tag{3.11}$$

$$\dot{s} = -\gamma r\left(t - \tau_{\text{vis}}\right) + a_s\xi_s. \tag{3.12}$$

Figures 3.1 to 3.6 refer to these equations as the 'model'. Again, s is the drifting fixed point. It is called as such because (deterministically) when $\dot{s} = 0$, $r^* = 0$, but if, temporarily, $\dot{s} \neq 0$, $r^* = s/(\kappa - \varepsilon)$. Hence, the fixed point of r drifts as a function of the slow fluctuations of s. When $\gamma = 0$ (no visual feedback), s is just the Wiener process and thus, non-stationary; otherwise, vision acts as a corrective mechanism which keeps the drifting fixed point stationary. As one would expect, with relatively small visual delays, compared to the large delays, the system is more corrective as seen by the lower long-range Hurst exponents (see Figs. 3.6 (a) and (b)), yet the short-term Hurst exponents do not vary significantly across all visual delay conditions as well as without vision.

3.5.4 Comparison of model with data

Figure 3.1 shows how the model replicates the experimental data in terms of the fast corrective r-dynamics and the s-dynamics for the no visual and delayed visual feedback cases with non-stationarity and stationarity, respectively. The standard deviations of the realizations of r in Fig. 3.2 show a similar pattern to the data as well. All PSDs of the model in Fig. 3.3 display the same two regimes similar to the data, and although the quantitative agreement is not strong, it is acceptable for this coarse level of modeling. Figure 3.4 shows that the model has the same PDF as the data for the no-vision case and for the delayed visual feedback. In particular, the variance is similar except for a higher peak at the origin.

Further, as Figs. 3.5 and 3.6 illustrate, the addition of the delayed visual feedback term to the s-dynamics produces lower values of the anti-persistent Hurst exponents (H_l) with respect to the no-vision condition as seen in the experimental data. Additionally, in Fig. 3.6 the short- and long-term Hurst exponents are all in the same range for the model and data. However, this is not true for the critical times, where the model has larger values than the data. Nevertheless, the values of τ_c for the model are less than 1 second which agrees with previous studies. Moreover, the critical times are flat across all visual delays, similar to the data.

3.5.5 Range of parameters

When simulating the model, we used subject-specific parameters for ε, κ and τ_{prop}. We attempted to model each participant in the experiment individually: $\varepsilon = mgL/\beta$, where m denotes the participant's mass, L represents the distance from the force plate to the COM, which is approximated by dividing the participant's height by 2 and the damping coefficient β could be given by [83]. To fulfill $\kappa > \varepsilon$, we fixed $\kappa = 1.5\varepsilon$ and $\tau_{\text{prop}} = 0.6\tau_{\text{crit}}$. As stated earlier, $\tau_{\text{vis}} = 200 + \{0, 250, 500, 750, 1000\}$ ms and $\gamma = 0.2$ s^{-1} for all participants. Lastly, the noise coefficients were $a_r = 1.8 \times 10^{-3}$ and $a_s = 1.2 \times 10^{-3}$ m s$^{-1/2}$. The choice of these parameters was made simply to fit the model to the data in terms all results shown earlier. The stability of the two-delay model was, however, far from being known in any detail. Therefore, we performed a numerical stability analysis on $r(t)$ in terms of τ_{prop} and τ_{vis}, where solutions with a standard deviation greater that 1 m are unbounded. Otherwise, we attempted to detect a fixed point or a marginally stable oscillation (since the system is linear). To detect a marginally stable oscillation. we computed the mean of the PSD in range of $\omega_{\text{crit}}/2\pi \pm 0.1$ Hz. If this value was greater than the mean of the PSD in the range $[0, \omega_{\text{crit}}/2\pi - 0.1]$ Hz, and greater than some threshold value of 10^{-4} m^2/Hz, it was labeled a marginally stable oscillation; otherwise it was a fixed point solution.

Fig. 3.8 shows the resulting numerically-determined stability diagram. We chose typical parameter values for $\varepsilon = 2$ and $\kappa = 1.5\varepsilon = 3$ Hz, and the noise coefficients were $a_r = a_s = 0$ m s$^{-1/2}$ since we were investigating the deterministic case. Solutions were computed for 1210 seconds and the first half of each solution is discarded to remove

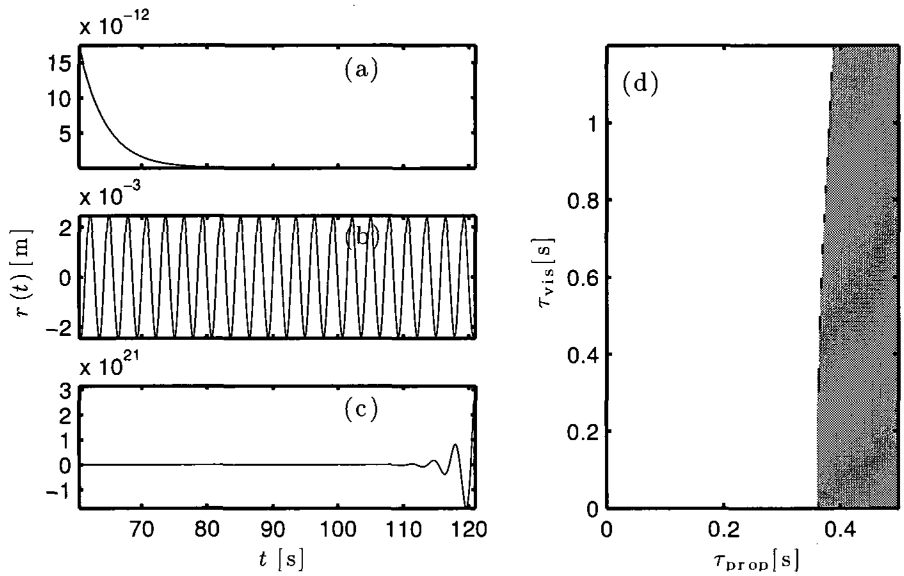

Figure 3.8 – For all time series $\tau_{\text{vis}} = 0.5$ s and (a) $\tau_{\text{prop}} = 0.2$ s, (b) $\tau_{\text{prop}} = 0.365$ s and (c) $\tau_{\text{prop}} = 0.450$ s. (d) Stability diagram: white, fixed point solution; black, marginally stable solution; grey - unbounded solution.

transients. Initial history functions were constant and lasted for 1 second; where $r_0 = 0.001$ and $s_0 = 0$ m. We then decided to investigate the stability of the two-delay subspace within the experimentally realistic range of $\tau_{\text{prop}} = [0, 0.5]$ and $\tau_{\text{vis}} = [0, 1.2]$ seconds. It is clear that the model was stable in our experimental regime, since τ_{prop} did not exceed ≈ 0.35 s and the maximum value of τ_{vis} was 1.2 seconds. One may also notice that the marginally stable oscillatory regime acts as a small boundary region separating the stationary and unbounded solution regimes.

3.5.6 Further analysis

Dependence of the critical time on delays

Let us recall Fig. 3.6 (c) where we have the critical time τ_c in relation to the experimental visual delay. This Fig.shows that τ_c is almost constant, however, we used the model to gain a better understanding of τ_c in terms of τ_{prop} and τ_{vis}. We averaged the values of τ_c over 25 realizations. Fig. 3.9 reveals that the critical time is predominantly a function of the proprioceptive delay, τ_{prop}.

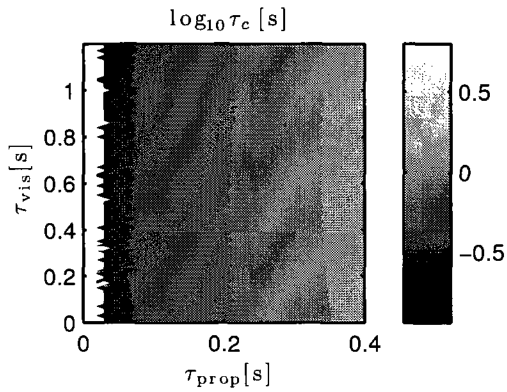

Figure 3.9 – Critical time τ_c as a function of proprioceptive delay τ_{prop} and visual delay τ_{vis}. White color on this Fig.indicates τ_c does not exist between 0.1 and 10 seconds. The same parameters are used here as in Fig. 3.8, but with noise.

Another interpretation of the relationship between COM and COP

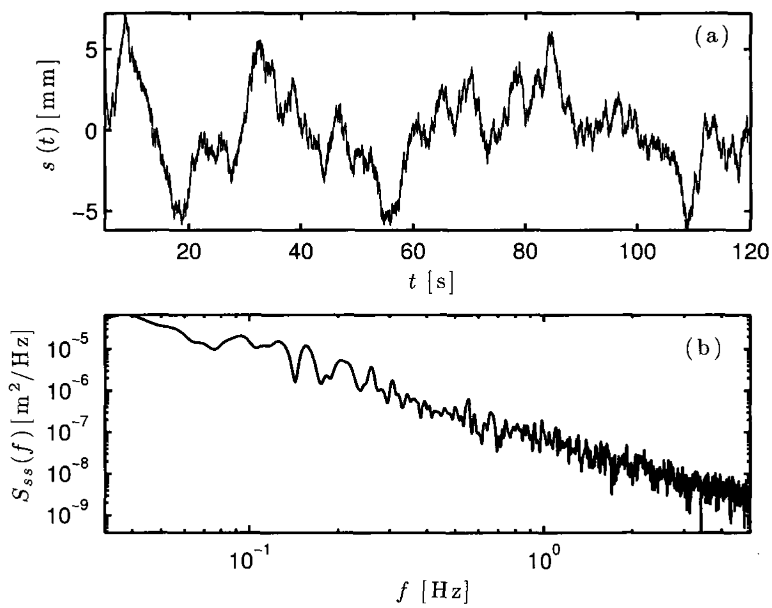

Figure 3.10 – (a) A sample realization of $s\,(t)$ for experimental visual delay of 750 ms and its (b) corresponding PSD.

We next compared the model's outcome to the empirical time series. Shown in

Fig. 3.10 (a) is a single realization of $s(t)$. Contrasting this to a typical realization of $r(t)$ in Fig. 3.1 (a), one may notice that $s(t)$ does not oscillate as fast as $r(t)$. If comparing the respective PSDs in Figs. 3.10 (b) and 3.3 (c), $S_{rr}(f)$ appears greater than $S_{ss}(f)$ between approximately 0.1 and 1 Hz. Hence, it seems that $s(t)$ is a low-pass filtered version of $r(t)$.

If we assume that $r(t)$ represents the COP and $s(t)$, the COM, then, this phenomenon has already been reported by [83, 8] and [87] from a biomechanical perspective. Yet, our model is defined in the time domain by Eqs. (3.11) and (3.12). Thus, because of the time-delayed term in Eq. (3.12), one may interpret $s(t)$ as a exponentially decaying memory process of $r(t)$.

Alternative models

During the process of model identification, we have tried numerous models including the following

$$\dot{r} = \varepsilon r - \kappa r\left(t - \tau_{\text{prop}}\right) - \gamma r\left(t - \tau_{\text{vis}}\right) + a_r \xi_r \tag{3.13}$$

where all variables and parameters have the same meaning as above. One problem with this model is that it undergoes large oscillations as τ_{vis} increases. The other problem is that there exists no mechanism to produce the drift-like process for eyes closed conditions. Another alternative is

$$\dot{r} = \varepsilon r - \kappa r\left(t - \tau_{\text{prop}}\right) - \gamma r\left(t - \tau_{\text{vis}}\right) + a_r \xi_r + s \tag{3.14}$$

$$\dot{s} = -\epsilon s + a_s \xi_s \tag{3.15}$$

where $\epsilon \ll a_r, a_s$. Even when ϵ is this small, the PDFs remain very narrow relative to the data and the power is much lower at low frequencies than in the data when there is delayed visual feedback.

3.6 Concluding remarks

We have presented new experimental data on posture control in healthy subjects in the presence of visually delayed feedback. The data reveal that visual feedback reduces the standard deviation of the postural sway, as expected [14], but it is not sensitive to the visual delay in the range investigated. This contrasts with the low frequency behavior [79]. We have also shown how the critical time separating persistent and anti-persistent behavior is well defined in the data, and furthermore, that it is not very sensitive to the visual delay. Moreover, the model shows the general phenomenon that achieves the short- and long-term corrections. We have proposed a novel modeling approach to such two-feedback posture control using a system of stochastic delay differential equations with two delays and noise, as well as a drifting fixed point meant to represent the slower fluctuation of the COM. The model qualitatively reproduces the main characteristics of our empirical findings with physiologically motivated parameter choices. The model further shows how, generically, the combination of delayed feedback and noise produces the proper diffusive short- and long-term fluctuations. Finally, it enables us to show how the critical time is mainly a function of proprioceptive delay.

3.7 Acknowledgements

We thank James Jun and Maarten van den Heuvel for the very informative discussions which aided us with the experimental apparatus.

Chapter 4

Methods

4.1 Experimental Methods

4.1.1 Equipment

When a human subject stands on force plate (FP), stresses are applied to four strain-gauge transducers (one in each quadrant of the force plate) which change the resistance of the coils they are made of. Every coil is located on a Wheatstone bridge. Compression due to applied stress, increases the length of the coil and thereby increasing its resistance which decreases the voltage over the coil. Depending on the configuration of the Wheatstone bridge, this corresponds to an increase or decrease in voltage. Consequently, these voltages on six channels may be converted to corresponding forces $\mathbf{F}$ and torques $\boldsymbol{\tau}$ as a function of time for the orthogonal x, y and z components. The force place used is manufactured by Advanced Mechanical Technology, Inc. (AMTI) (OR6-7, 2000 pound capacity). This force plate is connected to an amplifier (Amp) (AMTI MSA-6). For our force plate and amplifier, the conversion goes as follows. The gain factor is

$$GF = \left(1 \times 10^{-6} \frac{\mathrm{V}}{\mu\mathrm{V}} V_{\mathrm{ex}} GS\right)^{-1}$$

where the excitation voltage is $V_{\mathrm{ex}} = 10$ V, the amplifier gain is $G = 4000$, the sensitivities are $S = 0.0878$ $(\mu\mathrm{V/N})\mathrm{V}_{\mathrm{ex}}^{-1}$ for F_z, $S = 0.7913$ $(\mu\mathrm{V/N\,m})\mathrm{V}_{\mathrm{ex}}^{-1}$ for τ_x and $S = 0.7905$ $(\mu\mathrm{V/N\,m})\mathrm{V}_{\mathrm{ex}}^{-1}$ for τ_y. Once we have the gain factor for each channel, we only need the voltages at the output of the amplifier, $\{V_{\mathrm{amp}}\}$ to compute the respective vertical force and antero-posterior (AP) and medio-lateral (ML) torques: $\{F_z, \tau_x, \tau_y\} = \{V_{\mathrm{amp}}\}GF$. After amplification, the signal is routed to an analog serial connector (National Instruments BNC-2111 board). At this stage, the signals are still analog and unfiltered, however, we must collect them in a computer, which requires digitization (quantization and discretization). To achieve this we use an analog to digital converter (ADC) (National Instruments PCI 6220 board, 16-bit, 100 KS/s) at a sampling frequency of $F_s = 1000$ samples/second placed within a personal computer (PC) (2.4 GHz Pentium™, 1 GB RAM). From here, real-time computation and collection of the force and torque data is stored to disk and retrieved (also, in real-time) to compute the center of pressure (COP) (shown below) and display it on a 19 inch LCD panel (resolution: 1280×1024 pixels, refresh rate: 60 Hz) via the Matlab™ Data Acquisition toolbox and a custom code and graphical user interface (GUI) (see A.2.1). The COP displayed on the LCD was amplified by a factor of 5 for better visibility. The effects of amplifying the COP on a display in the context of DVF experiments has been studied [68] and revealed no significant effects on any characteristic postural control measures (see Sect. 2.6.1). The LCD display was placed 80 cm away from the subject, at eye-level. Within our code, the COP coordinate $r_i = (x_i, y_i)$ is computed component-wise by

$$x_i = \frac{\tau_{x,i}}{F_{z,i}} \tag{4.1}$$

$$y_i = \frac{\tau_{y,i}}{F_{z,i}}. \tag{4.2}$$

where $i = F_s t$ is the discretized time index. Once the COP coordinate is computed it is delayed by the experimental visual delay time τ_{v}, (where the discretized visual delay is $j = F_s\tau_v$) to give $r_{i-j} = (x_{i-j}, y_{i-j})$, then displayed onto the LCD as a small white dot upon a black background. This dot is only displayed at the maximum refresh rate of the LCD, 60 Hz. Drawn simultaneously onto the LCD is a slightly smaller red dot representing a stationary target at the origin. In terms of precision of the COP, we placed a mass on the FP, three different times in three different locations and recorded for two minutes. These gave us stationary times series for the x and y COP coordinates. The standard deviations for each time series were averaged to give $\sigma_x = \pm 0.568$ mm and $\sigma_y = \pm 0.564$ mm.

$$\xrightarrow{\{F_z, \tau_x, \tau_y\}(t)} \boxed{\text{FP}} \rightarrow \boxed{\text{Amp}} \xrightarrow{\{V_{\text{amp}}\}(t)} \boxed{\text{ADC/PC}} \xrightarrow{\{V_{\text{amp}}\}_i} \boxed{\text{Matlab/Code}} \xrightarrow{r_{i-j}} \boxed{\text{LCD}}$$

Figure 4.1 – Circuit diagram for experimental devices where FP is the force plate and Amp is the amplifier.

4.1.2 Human Subjects

For this study, we were interested in postural control in a healthy population. We selected our participants from a pool of university students. Their measured data is given in Table 4.1.

4.1.3 Procedure

Task

The experimental task assigned to each participant is to perform postural control. Participants were asked to conform the body to a straight, upright and rigid configuration with their hands at their sides, only using their ankles for any postural adjustments. There were six types of postural control tasks, each of which lasted for two minutes. The first was to stand on a force plate with eyes closed (no vision task) and to attempt to remain as stationary as possible. The last five tasks consisted of standing on a force plate

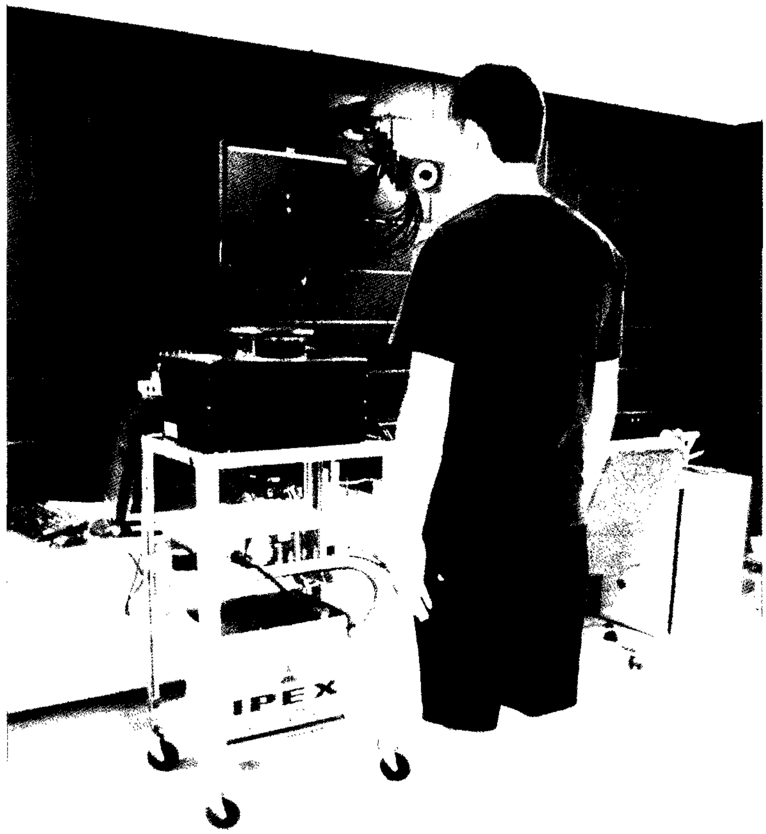

Figure 4.2 – Image of a subject standing on the force plate while maintaining a rigid stance. The LCD monitor shows the fixed target as well as the COP point. The subject tries to maintain the COP on the target.

and looking at a visual display which showed their COP in real time, represented as a white dot. The aim of these tasks was to maintain their bodies in the same rigid fashion, such that they aligned or overlapped their visual COP white dot onto the slightly larger red stationary target dot for the length of the trial. Unbeknownst to the participant

Table 4.1 – Human subject parameters: sex, age, mass and height.

Subject	Sex	Age [yr]	Mass [kg]	Height [cm]
AJ	F	23	63.6	170
AK	M	23	84.1	183
AT	F	22	59.1	163
BR	M	26	73.2	172
CB	F	24	61.4	152
DA	M	29	77.3	178
DG	M	28	81.8	178
EH	M	33	75.0	178
JS	F	25	57.7	168
JW	M	24	88.6	185
KT	F	28	54.0	173
MN	F	23	75.0	180
TC	M	24	85.0	174
TK	F	27	71.8	168
Mean	–	25.6	72.0	173
Standard deviation	–	3.05	11.1	8.64

was that each of these five tasks were different in the sense that the visual white dot was delayed by 0, 250, 500, 750, or 1000 milliseconds. These types of trials were called "delayed visual feedback" (DVF).

Protocol

Prior to the start of experimentation, each participant was required to read and accept the ethical consent form (Appendix C) reviewed by the University of Ottawa Research Ethics Board. Participants were allowed to wear shoes except for those with elevated heels and/or ankle constricting structures.

Each task was repeated five times for a total of thirty trials. In an attempt to remove possible effects of learning, the serial organization of trial execution used a block uniformly-distributed pseudo-randomized order. A block consisted of one trial of each type of task. Hence, in each block, all trials were randomly permuted. Therefore, in total, there were five blocks, each with a unique permutation of trials.

Participants were allowed to familiarize themselves with an instantaneous visual condition (0 ms delay) trial with feet at a comfortable distance in a fixed position and with a rigid body, hands on their side on the force plate. After practicing for a few minutes, they were asked to move their feet on the force plate and observe their COP trajectory onscreen while trying to place their COP marker on the target, in a effort to find a location on the force plate that minimized their effort to keep their marker on the target. Once this approximate location was found, it was marked on the force plate and all trials were performed here. This placement was done for each participant.

Before each trial, participants were asked to step off the force place to allow the experimenter to clear the electrical charge accumulated by the force plate during the previous trial. Participants were then asked to step back onto the force plate, when ready, to perform the next trial. If the trial was a no vision task, subjects were asked to close their eyes and they were told to reopen them at the end of the trial. If the trial type was DVF, the subjects were asked to place the white dot on the red target dot onscreen. After each trial was completed, the experimenter viewed the recorded COP time series to verify proper collection and writing to the disk of the COP data.

4.2 Numerical Methods

Initially, all of our data, whether simulated or experimental, had 121000 data points per trial since trials lasted 121 seconds and were collected at 1000 Hz. To remove possible transients, we discarded the first five seconds of each trial and the last second. Also, we *downsampled* the data by a factor of ten, which left us with $N = 11500$ data points. Downsampling by a factor F refers to removing the last $F - 1$ data points for every F data points.

4.2.1 Integration of Mathematical Models

In our work, we need to numerically integrate linear and nonlinear SDEs. For the Itō SDE (2.56) the Euler–Maruyama SDE integration scheme [36] was used, which is:

$$Y_{n+1} = Y_n + f(Y_n)\Delta t + g(Y_n)\Delta W_n. \tag{4.3}$$

where ΔW_n is the difference of two sequential samples of the Wiener process. To compute ΔW_n, we generate a sequence of independent ("δ-correlated") Gaussian noise samples ξ_n with mean $\mu = 0$ and variance $\sigma^2 = 1$ via the Ziggurat algorithm [45]. The increments of the Wiener process are then simply $\Delta W_n = \sqrt{\Delta t}\xi_n$, which is due to the fact that the stochastic differential $(\,\mathrm{d}W_t)^2$ behaves as $\mathrm{d}t$ in the mean squared sense [36]. Since the Euler–Maruyama scheme is an approximation of an SDE, the *absolute error criterion* [36] is evaluated as

$$\epsilon = E\left(|Y_n - X_n|\right) \tag{4.4}$$

where E denotes the expectation, $n = t/\Delta t$ is the sample at time t, Y_n is the approximation of the solution from the Euler–Maruyama method, and X_n is the exact solution at sample n. An approximation of a SDE, Y_n converges with strong order $\chi > 0$ where $\Delta t \in [0, 1]$ if there exists a constant $C > 0$ such that

$$\epsilon(\Delta t) = C\Delta t^{\chi}. \tag{4.5}$$

We wish to validate the Euler–Maruyama scheme by performing an error analysis for time steps $\Delta t = 2^{-m}$ s, where $m = 1, 2, \ldots, 10$. As a test function we used the Ornstein–Uhlenbeck process since its exact solution is known (see Eq. (2.59)). The Euler–Maruyama form of this process is

$$Y_{n+1} = Y_n - aY_n\Delta t + b\Delta W_n. \tag{4.6}$$

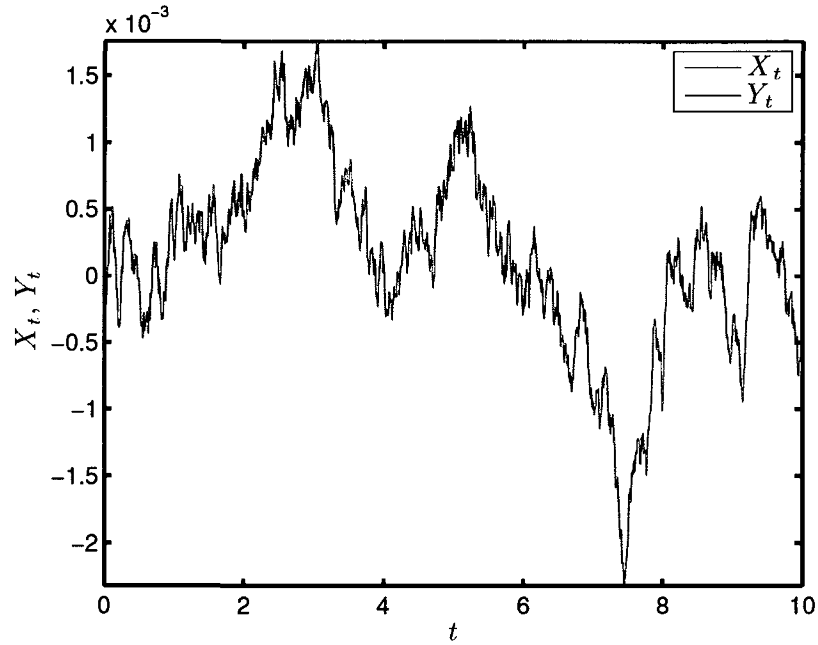

Figure 4.3 – One realization of the exact solution and Euler–Maruyama approximation of the Ornstein–Uhlenbeck process for 10 seconds, where $\Delta t = 0.01$ seconds. Notice how the exact and approximate solutions are indistinguishable.

One realization and exact solution of the Ornstein–Uhlenbeck process for a time step of $\Delta t = 0.01$ seconds is shown in Fig. 4.3. Numerically, we evaluate the absolute error criterion of the Euler–Maruyama scheme by simulating Ornstein–Uhlenbeck process for $N_{\mathrm{R}} = 1000$ realizations from $t_i = 0$ and $t_f = 10$ seconds for each time step as follows

$$\epsilon(\Delta t) = \frac{1}{NN_{\mathrm{R}}}\sum_{k=1}^{N_{\mathrm{R}}}\sum_{n=1}^{N}|Y_{k,n} - X_{k,n}| \tag{4.7}$$

where $N = (t_f - t_i)/\Delta t$, is the total number of samples per realization and k denotes the number of the realization. Figure 4.4 shows the results of this analysis.

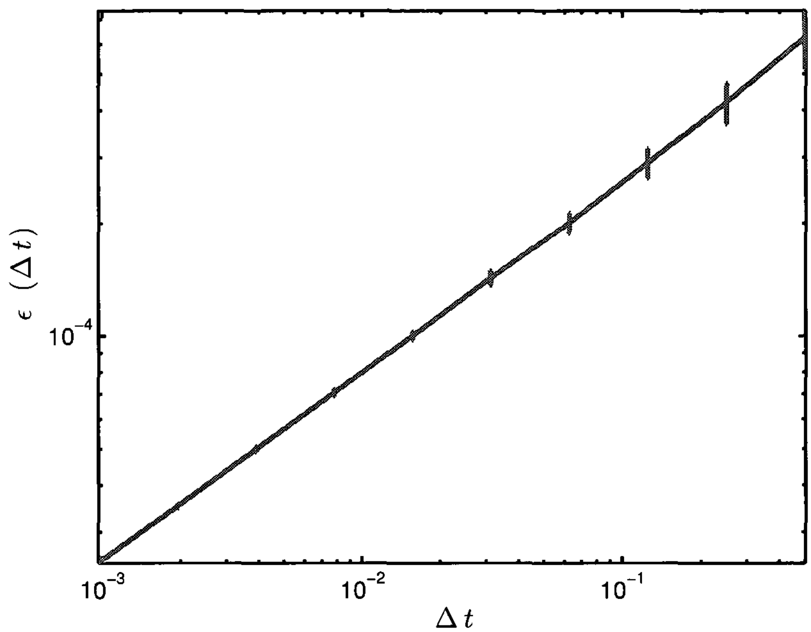

Figure 4.4 – Global truncation error per sample of the Euler–Maruyama scheme (simulated). This was averaged over 1000 realizations per Δt for ten seconds. Error bars show standard deviation over all realizations.

From the slope of Fig. 4.4, the Euler–Maruyama integration scheme converges with strong order $\chi = 0.5$ which means it has slower convergence than the standard Euler method which converges with strong order $\chi = 1.0$. Therefore, a requirement to use the Euler–Maruyama method is a relatively small time step.

Time Step

For all numerical computation of stochastic differential equations (SDE) with the Euler–Maruyama integration scheme we have chosen a time step of $\Delta t = 0.01$ seconds since from Fig. 4.4, the absolute error criterion is less than 10^{-4} per sample. From sampling theory, it is known that the sampling frequency (in samples per unit time) is $F_s = 1/\Delta t$. The maximum possible detectable frequency of a discretely sampled signal to allow for perfect reconstruction is called the Nyquist frequency, F_N [59], which admits to the condition, $2F_N \leqslant F_s$. This is of specific interest for our data and numerical integration of SDEs since the Nyquist frequency $F_N = F_s/2 = 2/\Delta t = 50$ Hz is at least one order of magnitude greater than the phenomena we are interested in.

Initial Conditions for Stochastic Delay Differential Equations

Just as a first order ODE requires one initial condition to determine its time evolution, the delay differential equation needs a history function which, in discrete time, is a vector spanning the discretized time interval $[-\tau, 0]$. To approximate an unbiased random walk, we used the Wiener process as the initial history functions for any stochastic delay differential equation (SDDE).

4.2.2 Power Spectral Density

For the PSD and PDF estimation, each trial of 115 seconds, $r(t)$ which from now on is the x component of the COP, underwent a mean-removal (or mean-centering) for every 30 seconds. This form of 'constant-piecewise-detrending' removed some of the non-stationarity. We used the first three, thirty second intervals of $r(t)$, and independently computed the PSD and PDF of each interval and then averaged them over these intervals, to obtain an average PSD and PDF for every trial.

For input data r_n (which is the discrete version of $r(t)$) of length N, PSDs were computed using the Matlab$^{\mathrm{TM}}$ periodogram function. In order ideally interpolate the PSD, we *zero padded* r_n [59] which is defined as

$$\tilde{r}_n(M) = \begin{cases} r_n, & |n| < N/2 \\ 0, & \text{otherwise} \end{cases} \tag{4.8}$$

where $M = 10N$ which was also the length of the data used to compute the fast Fourier Transform (FFT) as required for a PSD. A Hamming window of that length (M) was used to reduce spectral leakage. The Fourier Transform expects truly periodic measured signal intervals in order to build the frequency domain representation of a perceived-repetitive signal of infinite length. When the signal is not periodic in nature, the Fourier Transform will introduce sharp discontinuities into the signal which are then processed into sinusoids. The spectral energy from these sinusoids spreads across FFT bins from the fundamental frequency peak. Hence, by choosing an appropriate window, the amplitude of the discontinuities at the beginning and end of the window are attenuated, thereby reducing spectral leakage. The periodogram [59] is a non-parametric method of estimating the PSD of a random signal, and in discrete form is given by

$$S_{rr}(n) = \frac{\dfrac{2}{F_s}\left|\sum_{n=1}^{M} w_n \tilde{r}_n \exp\left(-i2\pi f n\right)\right|^2}{\dfrac{1}{M}\sum_{n=1}^{M} |w_n|^2} \tag{4.9}$$

and the Hamming window is

$$w_n = 0.54 - 0.46\cos\left(\frac{2\pi n}{M}\right), \tag{4.10}$$

where $1 \leqslant n \leqslant M$.

4.2.3 Probability Density Functions

The PDFs for $r(t)$ were computed by the Matlab$^{\mathrm{TM}}$ histogram function with 201 bins on a fixed r-axis with the range of $[-0.04, 0.04]$ meters.

4.2.4 Mean-Squared Displacement and Hurst Exponent

We use stabilogram-diffusion analysis [12] to compute the mean-squared displacement (see Sect. 2.6.1) and consequently, Hurst exponents, which we outline in detail below. The plots used in this analysis display the mean-squared displacement of the time series as a function of lag. This is done as follows in a discrete manner

$$K(m) = \frac{1}{N-m} \sum_{n=1}^{N-m} \left[r(n+m) - r(n)\right]^2, \tag{4.11}$$

where m is the discrete lag time. It should be noted that as m increases, the length of the sequence being summed decreases. The variance of $K(m)$ increases with m because less data is used in the average of Eq. (4.11) (this is why we divide by $N - m$, the number of points left, instead of N). From now on we will refer to the continuous analog of $K(m)$ as $K(\tau)$, where $\tau = m\Delta t$ is the lag time in seconds. Our data spans from 0 to 115 seconds, therefore, τ could also span this time. However, in practice, similar studies [12, 50] use the range $\tau = [0, 10]$ seconds, since after 10 seconds, $K(\tau)$ approaches a constant, or on average, the COP trajectory has reached its outer bounds and therefore, the MSD is saturated.

From the stabilogram-diffusion plot, there are some quantities of interest we wish to compute. First, the stabilogram-diffusion plot is usually shown on a log-log scale where the general shape of the MSD is $K(\tau) \propto \tau^{2H}$, where H is the Hurst exponent, for fractional Brownian motion (see Sect. 2.6.4). From this plot, there are typically two regimes of slopes of the mean-squared displacement for COP data which are usually $0.5 < H_s \leqslant 1$ on the short time scale, and on the long time scale we have $0 \leqslant H_l < 0.5$. The different slopes are separated by a critical time, τ_c, that separates the two regimes which is defined as the first time when $H = 0.5$.

Therefore, the quantities of interest are H_s, H_l and τ_c. To compute these quantities, we begin by partitioning r into 10 sections of equal length in a serial fashion. We then compute $K(\tau)$ on each section and average over each section to obtain $\langle K(\tau)\rangle$, which will be referred to herein simply as $K(\tau)$. The lag axis τ spans from 0 to 11.5 seconds since we chopped up r into 10 pieces, however, all points before 0.1 and after 10 seconds are discarded due to end effects. To detect the critical time τ_c, we must find the time at which $H = 0.5$, therefore we must differentiate $K(\tau)$ on a log-log scale, hence

$$H(\tau) = \frac{1}{2} \frac{\mathrm{d}\left[\log_{10} K(\tau)\right]}{\mathrm{d}\left[\log_{10} \tau\right]}. \tag{4.12}$$

We then apply a centered moving average of order 5 to H to remove the noisy effects of numerical differentiation. An algorithm then starts at $\tau = 0.1$ seconds and moves forward in time until it detects two points that satisfy the following condition: $H(m) > 0.5$ and $H(m+1) < 0.5$. The critical time is then the average of the two discrete lag times

$$\tau_c = \left(m + \frac{1}{2}\right) \Delta t. \tag{4.13}$$

Once we determine τ_c, we simply perform a linear regression and extract the slope from $[0.1, \tau_c]$ seconds and divide it by 2, (since $K(\tau) \propto \tau^{2H}$, see Sect. 2.6.4) to determine H_s and likewise on $[\tau_c, 10]$ seconds for H_l.

4.2.5 Recurrence Quantification Analysis

We computed the phase space reconstruction parameters, namely the optimal lag τ and embedding dimension d, for every trial. The lag was found by computing the first minimum of the average mutual information for each trial. Recurrence Quantification Analysis was performed for individual trials using the median lag determined for each condition (table 4.2). After calculating the percentage of False Nearest Neighbors as a function of embedding dimension, we chose the first embedding dimension that had the percentage of FNNs less than or equal to 3 percent. Again, the median values of the embedding dimensions per condition are shown in table 4.3. For every trial, we computed $\mathbf{R}_{i,j}$ for a set of threshold values. These values of ϵ were 1 to 20 percent (with increments of 1 percent) of maximum Euclidean distance of the reconstructed phase space. After this process was done for all trials in a particular condition, we computed the mean recurrence rate of all trials that were between 0.01 and 2 percent and chose the closest associated threshold value (rounded to the nearest positive integer), ϵ for RQA for that condition, as shown in table 4.4. We used the fastest and most robust algorithms for these relatively computationally intensive calculations. For RQA, we used the Commandline Recurrence Plots algorithm (`www.agnld.uni-potsdam.de/~marwan/6.download/rp.php`).

Table 4.2 – Lag, τ [ms], averaged across all trials and subjects.

Condition	Median	St. deviation	Minimum	Maximum
EC	129	28.8	67	204
0	78	21.9	49	157
250	94	21.9	60	194
500	107	25.0	46	174
750	113.5	30.8	57	175
1000	99	36.2	53	237

Table 4.3 – Embedding dimension, d, averaged across all trials and subjects.

Condition	Median	St. deviation	Minimum	Maximum
EC	4	0.5	3	4
0	4	0	4	4
250	4	0	4	4
500	4	0	4	4
750	4	0	4	4
1000	4	0.2	3	4

4.2.6 Largest Lyapunov Exponent

The mean logarithmic divergence of time series (see Sect. 2.8.3) was computed as a function of time by using the TIme SEries ANalysis (TISEAN) package, notably the `lyap_r`

Table 4.4 – Percent threshold of the maximum Euclidean distance, ϵ, averaged across all trials and subjects.

Condition	Mean	Rounded mean	St. deviation
EC	5.33	5	2.07
0	5.98	6	2.07
250	6.09	6	2.15
500	6.12	6	2.20
750	6.22	6	2.16
1000	5.82	6	2.08

algorithm (`www.mpipks-dresden.mpg.de/~tisean/`). The TISEAN algorithms were provided by the Nonlinear Dynamics and Time Series Analysis Group at the Max Planck Institute for the Physics of Complex Systems in Dresden, Germany. The linear scaling region's slope, λ_1 was extracted from time 0 to 0.5 seconds by performing a linear regression on that region for all trials. Chapter 6 shows the graphical details of why the scaling region is chosen to be [0,0.5] seconds. This process was repeated from dimension 1 to 8 to find the proper embedding dimension to use for computing the LLEs.

In the next chapter we present the development and analysis of the model presented in Chap. 3.

Chapter 5

Model Analysis

5.1 Introduction

In this chapter, we address the modeling attempts that led to the final model in Chap. 3. We discuss the success and failures of these preliminary models in reproducing features of the experimental data. We also explore the stability of the linear model of Chap. 3 as well as its nonlinear counterpart through multiple methods: numerical eigenvalue determination, delay-space stability via envelope detection and small delay approximation. Finally, we consider the effect of noise on the probability distribution of the linear model and we show that in the experiment's range of parameters, the linear and nonlinear models are in good agreement in terms of the power spectral densities.

5.2 Alternative Models

We have given validation to a model when it has been in close agreement with the data's (i) power spectral density, (ii) the probability distribution and (iii) the mean-squared displacement or corresponding Hurst exponents. However, throughout the course of model-building, it has become obvious just by the visual comparison of enough realizations of the model to the time series of the COP data that, if they are too different at this stage, then the model will not satisfy (i), (ii) and (iii). The easiest measures with which to assess agreement are the PSDs and PDFs. From Chap. 3 it should be clear that the data shows relatively high power at low frequencies for the conditions with no vision. The reason for this can be seen from Fig. 3.1. The scale is larger in Fig. 3.1(a), which shows the no vision condition than for Figs. 3.1(b) and 3.1(c), where there is visual feedback. There appears to be more drift or non-stationarity when vision is not present than for the DVF conditions. Consequently, the probability densities will be broader, and have larger variance. With this in mind, we will consider the alternative models shown in Chap. 3 to show the development of model iterations which led to the final model.

The first of these alternative models is given by Eq. (3.13) shown below

$$\dot{r} = \varepsilon r - \kappa r\left(t - \tau_{\text{prop}}\right) - \gamma r\left(t - \tau_{\text{vis}}\right) + a_r \xi_r. \tag{3.13}$$

We first attempted this model since it is a direct extension of Yao *et al.* [86] through the addition of delayed visual feedback. However, the main drawback of this equation is that it could not produce the large drifts found in the no vision condition ($\gamma = 0$). In Fig. 5.1, we show one simulation (one realization each) of three experimental conditions. The no vision condition, does not lead to larger variance and low frequency fluctuations (this is supported by PDF and PSD analyses, not shown). Therefore, it did not satisfy (i) and (ii), and hence could not be used to describe the experimental dynamics.

As a next iteration to the model, we attempted to add a weak drift-like behavior to the dynamics by introducing an additive (with respect to $\dot{r}$) Ornstein–Uhlenbeck process with $\epsilon \ll a_r, a_s$ which resulted in Eqs. (3.14) and (3.15):

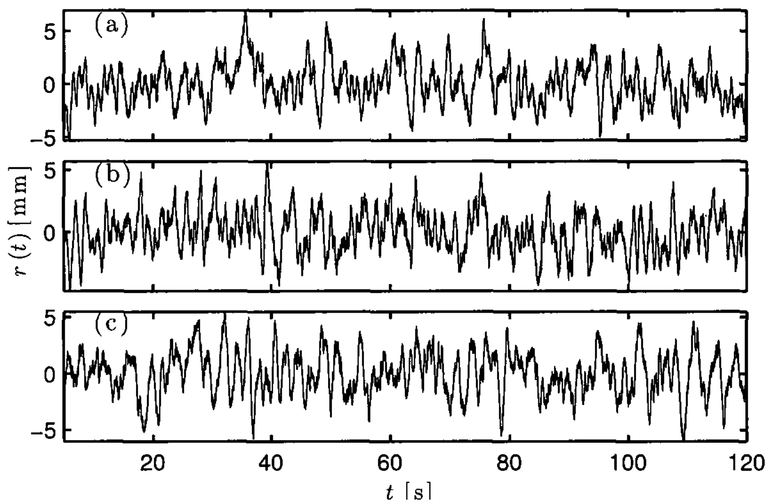

Figure 5.1 – Sample realizations of alternative model 1, Eq. (3.13), where the conditions are (a) no vision, (b) the 0 ms visual delay and (c) the 750 ms.

$$\dot{r} = \varepsilon r - \kappa r\left(t - \tau_{\text{prop}}\right) - \gamma r\left(t - \tau_{\text{vis}}\right) + a_r \xi_r + s \tag{3.14}$$

$$\dot{s} = -\epsilon s + a_s \xi_s. \tag{3.15}$$

From Fig. 5.2, in all conditions it is apparent that there is more drift than in Fig. 5.1 and due to the damping term, $-\epsilon s$, the drift must be bounded. However, the delayed visual feedback is not contributing to reducing the level of drift as we have observed experimentally since drift is added irrespective of the state of the variable r and the experimental condition.

To improve on this situation, we used drift as a condition-dependent dynamical variable. That is, drift was turned on for all conditions, however, it was modulated by negative feedback directly when vision was available. This reduced the scale of postural sway for DVF conditions, and as a result, (i) and (ii) were satisfied, giving Eqs. (3.11) and (3.12)

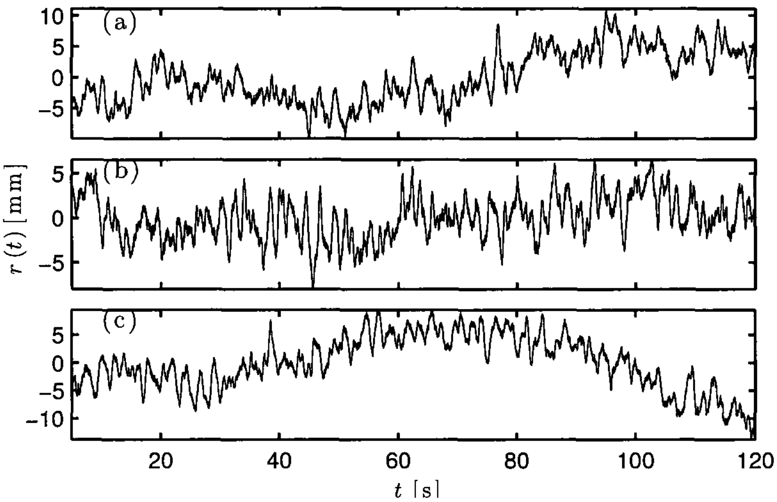

Figure 5.2 – Sample realizations of alternative model 2, Eqs. (3.14) and (3.15), where the conditions are (a) no vision, (b) the 0 ms visual delay and (c) the 750 ms.

$$\dot{r} = \varepsilon r - \kappa r\left(t - \tau_{\text{prop}}\right) + a_r \xi_r + s \tag{3.11}$$

$$\dot{s} = -\gamma r\left(t - \tau_{\text{vis}}\right) + a_s \xi_s. \tag{3.12}$$

Mathematically, when eyes are closed, the visual feedback strength $\gamma = 0$, and therefore, $\dot{s} = a_s \xi_s$ which means s is the Wiener process. This is the model that was deemed most satisfactory to reproduce the main data features without adding too many "fitting" parameters. It is thus a useful parsimonious dynamical systems model of visually guided postural sway. Nevertheless, when eyes are closed, the variance of s increases linearly with time, and is thus a non-stationary process driving $\dot{r}$. As a consequence, the variance of r grows proportionally to how much time has elapsed (see Sect. 2.6.3). Therefore to keep s stationary, as an extension to this model, we may introduce a restoring force term $-\epsilon s$ to Eq. (3.12) which gives

$$\dot{r} = \varepsilon r - \kappa r\left(t - \tau_{\text{prop}}\right) + a_r \xi_r + s \tag{3.11}$$

$$\dot{s} = -\epsilon s - \gamma r\left(t - \tau_{\text{vis}}\right) + a_s \xi_s. \tag{5.1}$$

There exists another possibility such that the process driving $\dot{r}$ obeys stationarity. Instead of simply adding s to Eq. (3.11), a nonlinear saturating function, $f(s)$ could be added instead

$$\dot{r} = \varepsilon r - \kappa r\left(t - \tau_{\text{prop}}\right) + a_r \xi_r + f(s) \tag{5.2}$$

$$\dot{s} = -\gamma r\left(t - \tau_{\text{vis}}\right) + a_s \xi_s. \tag{3.12}$$

Again, the saturation function could be $f(s) = \tanh(s/\varphi)$ where $\varphi > 1$.

5.3 Linear Model

5.3.1 Stability of the Linear Deterministic Model

In this section, we compute the eigenvalues of the linear model used in Chap. 3 to determine the boundaries of stability. This refers to regions in parameter space in which the solutions will be bounded (stable). Let us first consider the deterministic versions ($a_r = a_s = 0$) of Eqs. (3.11) and (3.12) below

$$\dot{r} = \varepsilon r - \kappa r\left(t - \tau_{\text{prop}}\right) + s \tag{5.3}$$

$$\dot{s} = -\gamma r\left(t - \tau_{\text{vis}}\right). \tag{5.4}$$

with the positive set of parameters $\{\varepsilon, \kappa, \gamma, \tau_{\text{prop}}, \tau_{\text{vis}}\}$. A list of parameters used to simulate the COP of each participant is shown in Appendix B. Equations (5.3) and (5.4) may be rewritten by differentiating Eq. (5.3) once with respect to time, and then combining with Eq. (5.4) to yield

$$\ddot{r} = \varepsilon \dot{r} - \kappa \dot{r}\left(t - \tau_{\text{prop}}\right) - \gamma r\left(t - \tau_{\text{vis}}\right). \tag{5.5}$$

From this, we may use the ansatz $r(t) = r(0)\exp(\lambda t)$, where $\lambda \in \mathbb{C}$ to obtain the corresponding characteristic equation:

$$\lambda^2 - \varepsilon\lambda + \kappa\lambda\exp\left(-\lambda\tau_{\text{prop}}\right) + \gamma\exp\left(-\lambda\tau_{\text{vis}}\right) = 0. \tag{5.6}$$

This characteristic equation does not have an analytical solution since it contains a transcendental function, namely the W-Lambert function $W(z)$ defined implicitly as $z = W(z)\exp[W(z)]$. If we consider the eigenvalues that are purely imaginary, $\lambda = i\omega$, which usually lie at the boundary between stability and instability (see Sect. 2.3), then we may separate the real and imaginary parts of (5.6), obtaining equations for ω:

$$\omega^2 - \kappa\omega\sin\omega\tau_{\text{prop}} - \gamma\cos\omega\tau_{\text{vis}} = 0 \tag{5.7}$$

$$\varepsilon\omega - \kappa\omega\cos\omega\tau_{\text{prop}} + \gamma\sin\omega\tau_{\text{vis}} = 0. \tag{5.8}$$

Solutions to these equations define curves in parameter space across which stability changes may occur. There exists no analytical solution to Eqs. (5.7) and (5.8) either. Therefore, we must resort to numerical solutions. Conveniently, TRACE-DDE [4] is a Matlab™ toolbox for numerical stability analysis of linear DDEs. We use this public domain software to compute eigenvalues for our linear model, which may be written in matrix from as:

$$\begin{bmatrix} \dot{r}(t) \\ \dot{s}(t) \end{bmatrix} = \begin{bmatrix} \varepsilon & 1 \\ 0 & 0 \end{bmatrix} \begin{bmatrix} r(t) \\ s(t) \end{bmatrix} + \begin{bmatrix} -\kappa & 0 \\ 0 & 0 \end{bmatrix} \begin{bmatrix} r(t-\tau_{\text{prop}}) \\ s(t-\tau_{\text{prop}}) \end{bmatrix} + \begin{bmatrix} 0 & 0 \\ -\gamma & 0 \end{bmatrix} \begin{bmatrix} r(t-\tau_{\text{vis}}) \\ s(t-\tau_{\text{vis}}) \end{bmatrix}. \tag{5.9}$$

Figure 3.8(d), considers the delay-space stability diagram—*i.e.*, the stability boundary confined to a 2-dimensional subspace $(\tau_{\text{prop}}, \tau_{\text{vis}})$. We shall confirm the stability in these regions by computing the respective eigenvalues. For Fig. 3.8(a), we have the fixed point solution regime. If we choose $\varepsilon = 2$, $\kappa = 3$, $\gamma = 0.2$, $\tau_{\text{prop}} = 0.2$, $\tau_{\text{vis}} = 0.5$, we obtain the eigenvalues shown in Fig. 5.3(a). Notice how all eigenvalues have negative real parts, confirming the globally stable fixed point solution. Now, if we change, $\tau_{\text{prop}} = 0.45$, and keep all other parameters constant, we obtain the eigenvalues in Fig. 5.3(b), which shows two dominant eigenvalues with positive real parts, making the solution globally unstable, or unbounded. Therefore, as the proprioceptive delay increases, posture becomes unstable (see Fig. 5.3).

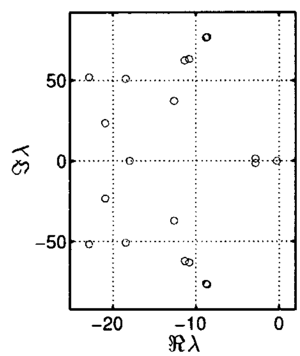

(a) $\tau_{\text{prop}} = 0.2$ s

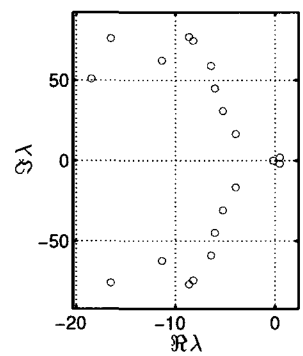

(b) $\tau_{\text{prop}} = 0.45$ s

Figure 5.3 – Eigenvalues for regions of stability in Fig. 3.8 (a) and (c).

The boundary separating the fixed point and unbounded regimes has marginal stability. This means that on one side, we have stability and on the other, instability. In this system, the instability emerges through two dominant eigenvalues with the negative real part becoming positive. Therefore, the eigenvalues corresponding to the boundary of marginal stability are completely imaginary as shown in Fig. 5.4 where $\tau_{\text{prop}} = 0.365$.

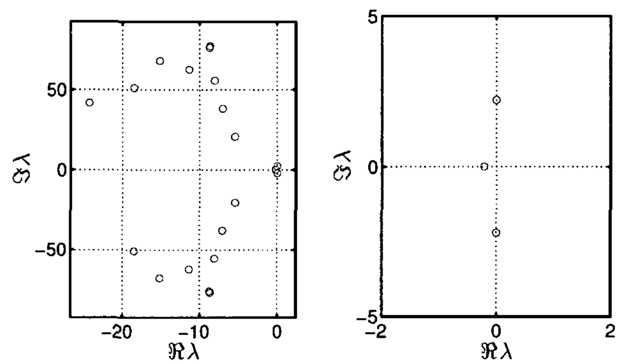

(a) 20 eigenvalues (b) zoom to origin

Figure 5.4 – Marginally stable oscillations: subcritical Andronov–Hopf bifurcation where where the parameters for Eq. (5.9) are $\varepsilon = 2$, $\kappa = 3$, $\gamma = 0.2$, $\tau_{\text{prop}} = 0.365$, $\tau_{\text{vis}} = 0.5$; stability region shown in Fig. 3.8 (b).

Another set of parameters, $\varepsilon = 2$, $\kappa = 3$, $\gamma = 1.85$, $\tau_{\text{prop}} = 0.2$, $\tau_{\text{vis}} = 0.5$, shows marginally oscillatory behavior as evidenced by the eigenvalues of Eq. (5.9) shown in Fig. 5.5. Therefore, increasing the visual feedback strength, γ, and keeping all other parameters constant, also results in destabilization if $\gamma > 1.85$ Hz.

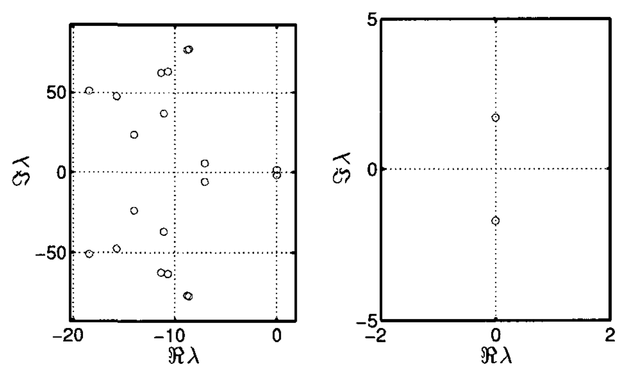

(a) 20 eigenvalues (b) zoom to origin

Figure 5.5 – Marginally stable oscillations: subcritical Andronov–Hopf bifurcation where $\tau_{\text{prop}} = 0.2$ s, $\gamma = 1.85$ Hz

Therefore, we have found that there exists two independent possibilities for which the linear system will become unstable: (i) increasing the proprioceptive delay, τ_{prop}, beyond some critical value which is parameter-dependent, similar to [37], and (ii) increasing the visual feedback strength, γ.

5.3.2 Power Spectral Density

From Chap. 3, the linear model describes the data very well. However, to confirm the validity of the linear model over the experimental range, we may obtain an analytical expression for the PSD of Eqs. (3.11) and (3.12). We then compare it to the PSD of the simulated linear model, then to the PSD of the simulated nonlinear model. We show the PSD for a range of visual feedback strengths. To begin, let us compute the Fourier Transform of Eqs. (3.11) and (3.12):

$$i\omega\hat{r} = \varepsilon\hat{r} - \kappa\exp\left(-i\omega\tau_{\text{prop}}\right)\hat{r} + a_r\hat{\xi}_r + \hat{s} \tag{5.10}$$

$$i\omega\hat{s} = -\gamma\exp\left(-i\omega\tau_{\text{vis}}\right)\hat{r} + a_s\hat{\xi}_s \tag{5.11}$$

we then multiply Eq. (5.10) by $i\omega$ which gives

$$-\omega^2\hat{r} = i\omega\varepsilon\hat{r} - i\omega\kappa\exp\left(-i\omega\tau_{\text{prop}}\right)\hat{r} + i\omega a_r\hat{\xi}_r + i\omega\hat{s}. \tag{5.12}$$

Now we may substitute Eq. (5.11) into Eq. (5.12) which returns an expression in terms of $\hat{r}$ only

$$-\omega^2\hat{r} = i\omega\varepsilon\hat{r} - i\omega\ \kappa\exp\left(-i\omega\tau_{\text{prop}}\right)\hat{r} - \gamma\exp\left(-i\omega\tau_{\text{vis}}\right)\hat{r} + i\omega a_r\hat{\xi}_r + a_s\hat{\xi}_s \tag{5.13}$$

and after collecting all $\hat{r}$ terms we are left with

$$\left[-\omega^2 - i\omega\varepsilon + i\omega\kappa \exp\left(-i\omega\tau_{\text{prop}}\right) + \gamma \exp\left(-i\omega\tau_{\text{vis}}\right)\right] \hat{r} = i\omega a_r \hat{\xi}_r + a_s \hat{\xi}_s. \tag{5.14}$$

Therefore, the Fourier Transform of r is

$$\hat{r} = \frac{i\omega a_r \hat{\xi}_r + a_s \hat{\xi}_s}{-\omega^2 - i\omega\varepsilon + i\omega\kappa \exp\left(-i\omega\tau_{\text{prop}}\right) + \gamma \exp\left(-i\omega\tau_{\text{vis}}\right)}. \tag{5.15}$$

Knowing that the PSD of r may be expressed as $S_{rr}(\omega) = \langle \hat{r}\hat{r}^* \rangle$ and $\langle \hat{\xi}_r \hat{\xi}_r^* \rangle = \langle \hat{\xi}_r \hat{\xi}_s^* \rangle = \langle \hat{\xi}_s \hat{\xi}_s^* \rangle = 1/2\pi$, we obtain

$$S_{rr}(\omega) = \frac{1}{2\pi} \frac{a_s^2 + a_r^2 \omega^2}{\left(\omega^2 - \kappa\omega \sin \omega\tau_{\text{prop}} - \gamma \cos \omega\tau_{\text{vis}}\right)^2 + \left(\varepsilon\omega - \kappa\omega \cos \omega\tau_{\text{prop}} + \gamma \sin \omega\tau_{\text{vis}}\right)^2}. \tag{5.16}$$

From Figs. 5.6 (the 0 ms DVF condition) and 5.7 (the 750 ms DVF condition), the analytical PSDs of the linear model (a) are similar the numerical PSD of the linear model (b). Here, all numerical PSDs have been averaged over 1000 realizations. Furthermore, by comparing the numerical PSDs of the linear (b) and nonlinear (c) models, they appear to be very similar. With this progression, it should be clear that the spectral components of the linear and nonlinear models are identical for the parameters, $\varepsilon = 2$, $\kappa = 3$, and $\tau_{\text{prop}} = 0.2$. Therefore, in terms of frequency components, the linear model is equivalent to the nonlinear model.

5.3.3 Effect of Noises

To ascertain the effect of both noise intensities, a_r and a_s, we compute the probability densities (for 1000 realizations) of the linear model as a function of one noise intensity

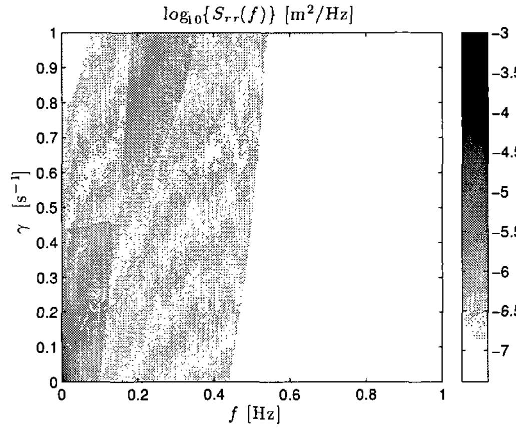

(a) Analytical PSD of linear model

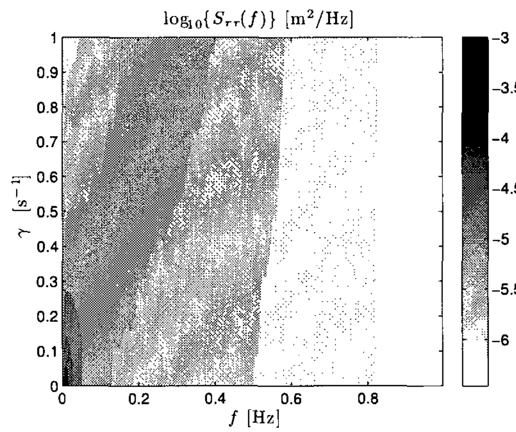

(b) Numerical PSD of linear model

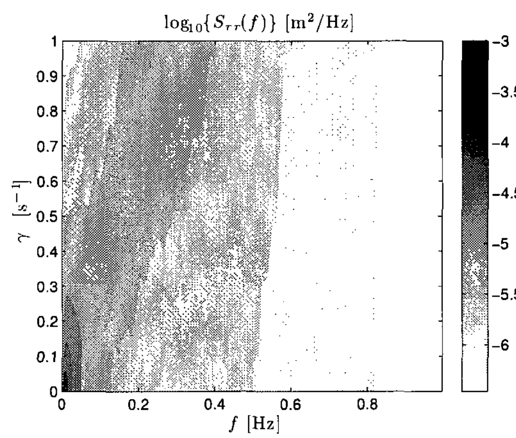

(c) Numerical PSD of hyperbolic tangent model

Figure 5.6 – PSD for $\tau_{\text{vis}} = 0$ ms while varying γ from 0 to 1 s^{-1}.

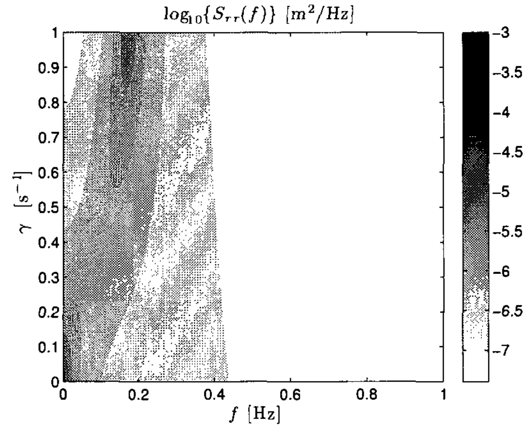

(a) Analytical PSD of linear model

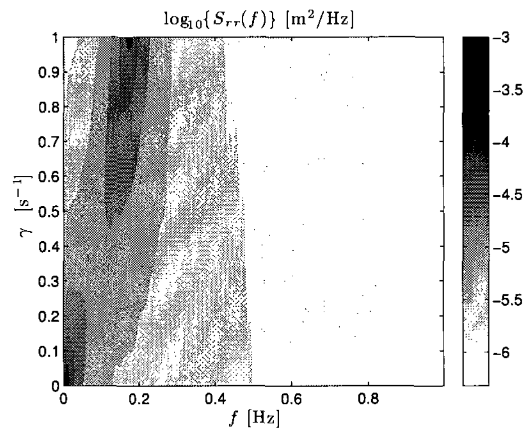

(b) Numerical PSD of linear model

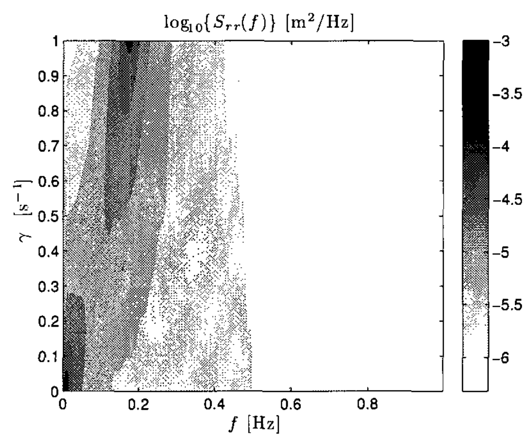

(c) Numerical PSD of hyperbolic tangent model

Figure 5.7 – PSD for $\tau_{\text{vis}} = 750$ ms while varying γ from 0 to 1 s^{-1}.

while holding the other constant for the following experimental conditions: no vision, 0 ms DVF and 750 ms DVF. Figure 5.6 shows the probability density $p(r)$ of r while varying the noise intensity a_r and Fig. 5.7 shows $p(r)$ as a function of a_s. There does not appear to be much difference within Figs. 5.6 and 5.7. However, if we compare both of these figures, *i.e.*, the probability densities as functions of both types of noise intensities, then it may appear that the variance of $p(r)$ as a function of a_s (in Fig. 5.7) has a larger variance, yet the probability density decreases as the noise intensity increases relative to Fig. 5.6. Perhaps a direct way of illustrating this is to plot the standard deviation σ_r, of r, as a function both noise intensities.

Figure 5.10 shows the standard deviations of the probability densities of r while co-varying noise intensities a_r and a_s, shown in Figs. 5.8 and 5.9. It is now clear that in all experimental conditions (even without vision) that the noise intensity a_r, responsible for musculoskeletal noise is more dominant than a_s, the noise intensity responsible for drift.

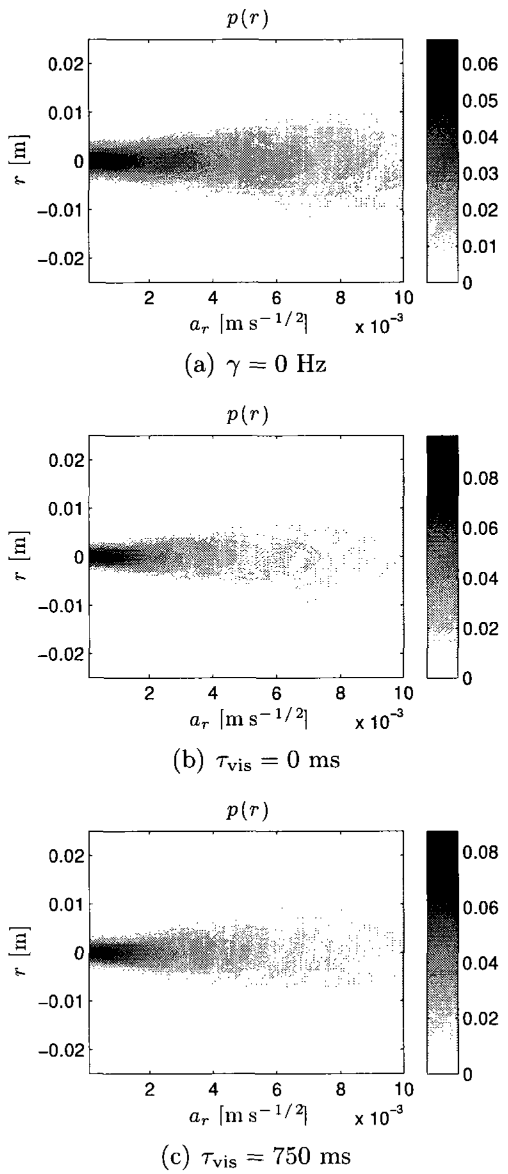

(a) $\gamma = 0$ Hz

(b) $\tau_{\text{vis}} = 0$ ms

(c) $\tau_{\text{vis}} = 750$ ms

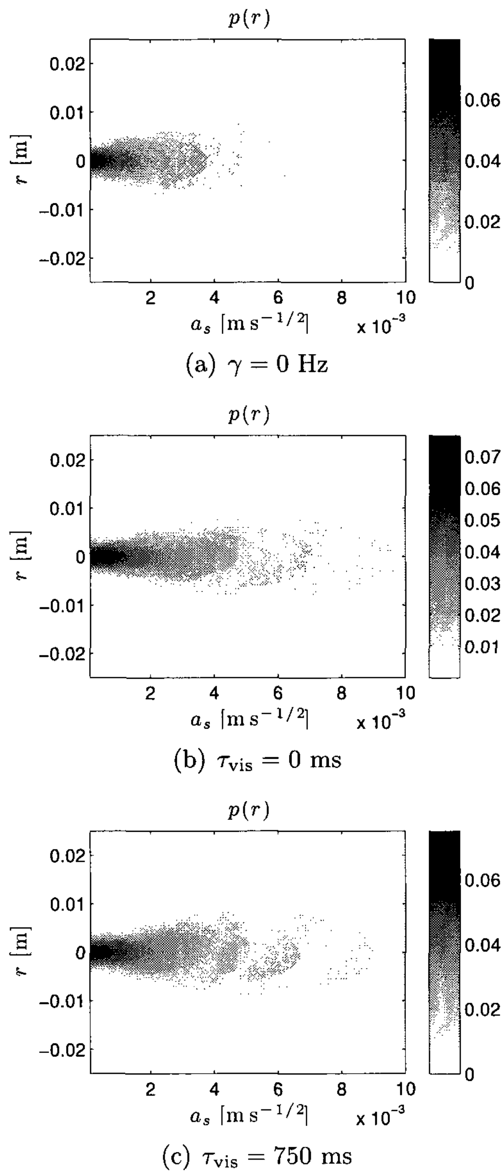

(a) $\gamma = 0$ Hz

(b) $\tau_{\text{vis}} = 0$ ms

(c) $\tau_{\text{vis}} = 750$ ms

Figure 5.8 – Probability density functions for different values of a_r from 0.0001 to 0.01 ms$^{-1/2}$ and $a_s = 0.0018$ ms$^{-1/2}$.

Figure 5.9 – Probability density functions for different values of a_s from 0.0001 to 0.01 ms$^{-1/2}$ and $a_r = 0.0012$ ms$^{-1/2}$.

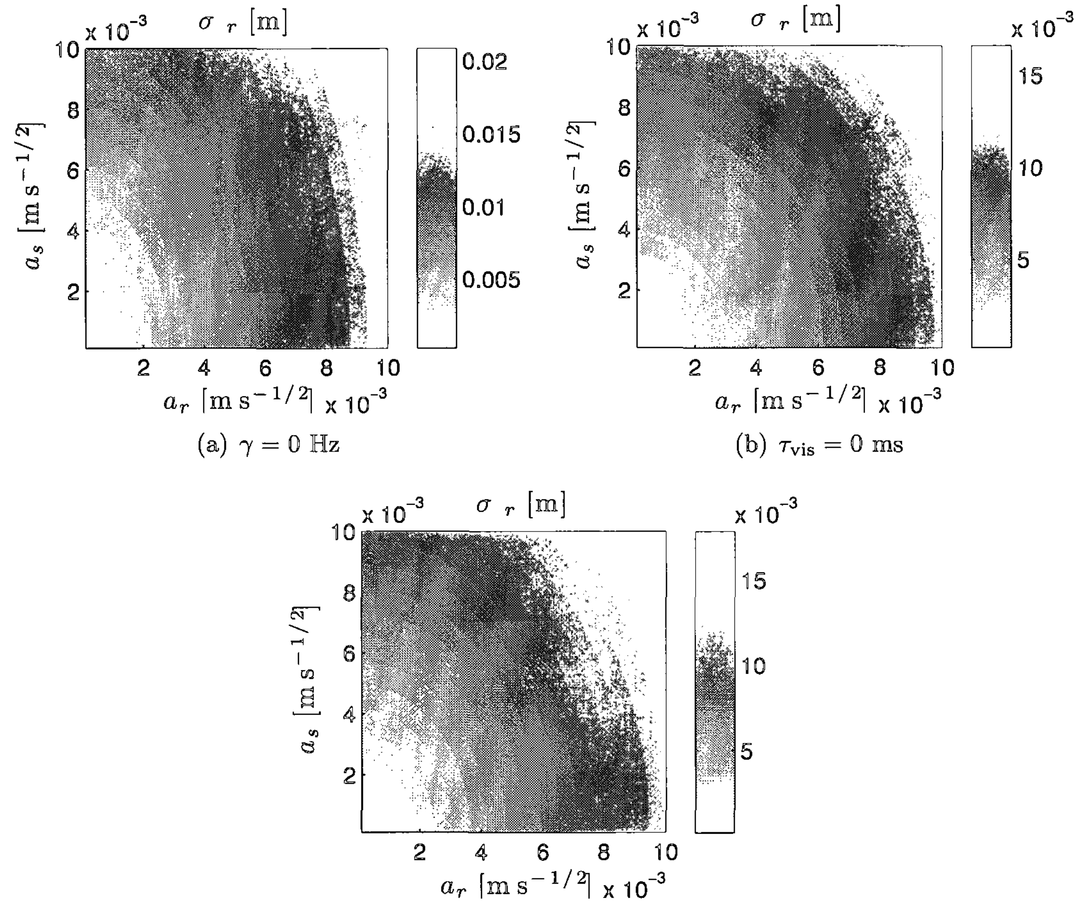

(a) $\gamma = 0$ Hz

(b) $\tau_{\text{vis}} = 0$ ms

(c) $\tau_{\text{vis}} = 750$ ms

Figure 5.10 – Standard deviation of r as a function of the noise intensities Standard deviation of r as a function of the noise intensities a_r and a_s.

5.4 Hyperbolic Tangent Model

5.4.1 Small Delay Approximation

As we have shown earlier, an analytical representation of the stability boundaries cannot be found since there exists no analytical expression for the eigenvalues of the linear model. We have found eigenvalues via numerical methods, however, we lack a systematic approach to solving for the eigenvalues of the system. However, there is a method of approximating DDEs by converting them into ODEs by removing higher-order terms via the Taylor expansion. This works when delays are smaller or equal to other time scales of the deterministic system. It is not clear which modes are kept exactly, but in 2 dimensions as we have here, complex eigenvalues are still possible whereas, only real-valued eigenvalues may arise in a 1 dimensional system. Hence, following the treatment of the small delay approximation of SDDEs by Guillouzic *et al.* [27], we will apply the technique to the general from of our nonlinear model

$$\dot{r} = \varepsilon r - \kappa f\left(r_{\tau_{\text{prop}}}\right) + a_r \xi_r(t) + s \tag{5.17}$$

$$\dot{s} = -\gamma h\left(r_{\tau_{\text{vis}}}\right) + a_s \xi_s(t) \tag{5.18}$$

where $r_{\tau_{\text{prop}}} \equiv r\left(t - \tau_{\text{prop}}\right)$ and $r_{\tau_{\text{vis}}} \equiv r\left(t - \tau_{\text{vis}}\right)$. We may do a Taylor expansion of f and h about $r_{\tau_{\text{prop}}}$ and $r_{\tau_{\text{vis}}}$ respectively

$$\begin{aligned} f\left(r\left(t - \tau_{\text{prop}}\right)\right) &\cong f\left(r(t)\right) + \left[r_{\tau_{\text{prop}}} - r(t)\right] \frac{\partial f\left(r(t)\right)}{\partial r_{\tau_{\text{prop}}}} + \mathcal{O}(2) \\ h\left(r\left(t - \tau_{\text{vis}}\right)\right) &\cong h\left(r(t)\right) + \left[r_{\tau_{\text{vis}}} - r(t)\right] \frac{\partial h\left(r(t)\right)}{\partial r_{\tau_{\text{vis}}}} + \mathcal{O}(2). \end{aligned}$$

Similarly, $r_{\tau_{\text{prop}}}$ and $r_{\tau_{\text{vis}}}$ may be expanded by the Taylor expansion around τ_{prop} and τ_{vis} respectively, shown below

$$\begin{aligned} r\left(t - \tau_{\text{prop}}\right) &\cong r(t) - \tau_{\text{prop}} \dot{r}(t) + \mathcal{O}(2) \\ r\left(t - \tau_{\text{vis}}\right) &\cong r(t) - \tau_{\text{vis}} \dot{r}(t) + \mathcal{O}(2). \end{aligned}$$

From this we have the general approximate expressions of f and h around their respective delays

$$f\left(r_{\tau_{\text{prop}}}\right) \approx f\left(r\left(t\right)\right) - \tau_{\text{prop}}\dot{r}\left(t\right)\frac{\partial f\left(r\left(t\right)\right)}{\partial r_{\tau_{\text{prop}}}}$$
$$h\left(r_{\tau_{\text{vis}}}\right) \approx h\left(r\left(t\right)\right) - \tau_{\text{vis}}\dot{r}\left(t\right)\frac{\partial h\left(r\left(t\right)\right)}{\partial r_{\tau_{\text{vis}}}}.$$

We may obtain similar expressions for f and h without explicit time-dependent delays and derivatives by substituting the model (Eqs. (5.17) and (5.18)) as follows

$$f\left(r_{\tau_{\text{prop}}}\right) \approx f\left(r\left(t\right)\right) - \tau_{\text{prop}}\frac{\partial f\left(r\left(t\right)\right)}{\partial r_{\tau_{\text{prop}}}}\left[\varepsilon r\left(t\right) - \kappa f\left(r_{\tau_{\text{prop}}}\right) + a_r\xi_r\left(t\right) + s\left(t\right)\right]$$
$$h\left(r_{\tau_{\text{vis}}}\right) \approx h\left(r\left(t\right)\right) - \tau_{\text{vis}}\frac{\partial h\left(r\left(t\right)\right)}{\partial r_{\tau_{\text{vis}}}}\left[\varepsilon r\left(t\right) - \kappa f\left(r_{\tau_{\text{prop}}}\right) + a_r\xi_r\left(t\right) + s\left(t\right)\right].$$

Approximate Model Equations

After substituting the above approximate expressions for f and h into $\dot{r}$ and $\dot{s}$, we obtain approximate expressions for $\dot{r}$ and $\dot{s}$ given below

$$\begin{aligned}\dot{r} &\approx \varepsilon r\left(t\right) - \kappa f\left(r\left(t\right)\right) \\ &\quad + \kappa\tau_{\text{prop}}\frac{\partial f\left(r\left(t\right)\right)}{\partial r_{\tau_{\text{prop}}}}\left[\varepsilon r\left(t\right) - \kappa f\left(r\left(t\right)\right) + a_r\xi_r\left(t\right) + s\left(t\right)\right] + a_r\xi_r\left(t\right) + s\left(t\right) \qquad (5.19)\end{aligned}$$

$$\dot{s} \approx -\gamma h\left(r\left(t\right)\right) + \gamma\tau_{\text{vis}}\frac{\partial h\left(r\left(t\right)\right)}{\partial r_{\tau_{\text{vis}}}}\left[\varepsilon r\left(t\right) - \kappa f\left(r\left(t\right)\right) + a_r\xi_r\left(t\right) + s\left(t\right)\right] + a_s\xi_s\left(t\right). \qquad (5.20)$$

After grouping terms we have

$$
\begin{aligned}
\dot{r} &\approx \varepsilon r(t)\left[1+\kappa\tau_{\text{prop}}\frac{\partial f(r(t))}{\partial r_{\tau_{\text{prop}}}}\right]-\kappa f(r(t))\left[1+\kappa\tau_{\text{prop}}\frac{\partial f(r(t))}{\partial r_{\tau_{\text{prop}}}}\right] \\
&+\kappa\tau_{\text{prop}}\frac{\partial f(r(t))}{\partial r_{\tau_{\text{prop}}}}\left[a_r\xi_r(t)+s(t)\right]+a_r\xi_r(t)+s(t) \qquad (5.21) \\
\dot{s} &\approx -\gamma h(r(t))+\gamma\tau_{\text{vis}}\frac{\partial h(r(t))}{\partial r_{\tau_{\text{vis}}}}\left[\varepsilon r(t)-\kappa f(r(t))+a_r\xi_r(t)+s(t)\right]+a_s\xi_s(t). \qquad (5.22)
\end{aligned}
$$

With the removal of the noise terms we are left with the deterministic dynamics in the small-delay approximation:

$$
\begin{aligned}
\dot{r} &\approx \varepsilon r(t)\left[1+\kappa\tau_{\text{prop}}\frac{\partial f(r(t))}{\partial r_{\tau_{\text{prop}}}}\right]-\kappa f(r(t))\left[1+\kappa\tau_{\text{prop}}\frac{\partial f(r(t))}{\partial r_{\tau_{\text{prop}}}}\right] \\
&+\kappa\tau_{\text{prop}}\frac{\partial f(r(t))}{\partial r_{\tau_{\text{prop}}}}s(t)+s(t) \qquad (5.23) \\
\dot{s} &\approx -\gamma h(r(t))+\gamma\tau_{\text{vis}}\frac{\partial h(r(t))}{\partial r_{\tau_{\text{vis}}}}\left[\varepsilon r(t)-\kappa f(r(t))+s(t)\right]. \qquad (5.24)
\end{aligned}
$$

Linearization

The original system (Eqs. (5.17) and (5.18)) has the fixed point (r^*, s^*) that satisfies

$$
\begin{aligned}
\dot{r} &= \varepsilon r-\kappa f\left(r_{\tau_{\text{prop}}}\right)+s=0=\varepsilon r^*-\kappa f(r^*)+s^* \qquad (5.25) \\
\dot{s} &= -\gamma h\left(r_{\tau_{\text{vis}}}\right)=0=-\gamma h(r^*) \qquad (5.26)
\end{aligned}
$$

but as f and h are tanh functions, we get $(r^*, s^*)=(0,0)$. Since f and h are functions of only one argument, we can simplify using the notation

$$\frac{\partial f(r(t))}{\partial r_{\tau_{\text{prop}}}} \to \left.\frac{\partial f}{\partial r}\right|_{r(t)}$$
$$\frac{\partial h(r(t))}{\partial r_{\tau_{\text{vis}}}} \to \left.\frac{\partial h}{\partial r}\right|_{r(t)}$$

where $f(r(t)) = h(r(t)) = \tanh(r(t))$. We then have:

$$\begin{aligned}
\left.\frac{\partial f}{\partial r}\right|_{r(t)} &= \frac{\partial \tanh(r(t))}{\partial r} \\
&\equiv F(r(t)) \\
&= F(r^*) + [r(t) - r^*] \left.\frac{\mathrm{d}F}{\mathrm{d}r}\right|_{r^*} \\
&= F(0) + r(t) \left.\frac{\mathrm{d}F}{\mathrm{d}r}\right|_{0} \\
\left.\frac{\partial f}{\partial r}\right|_{r(t)} &= \left.\frac{\mathrm{d}f}{\mathrm{d}r}\right|_{0} + r(t) \left.\frac{\mathrm{d}^2 f}{\mathrm{d}r^2}\right|_{0} && (5.27) \\
\left.\frac{\partial h}{\partial r}\right|_{r(t)} &= \left.\frac{\mathrm{d}h}{\mathrm{d}r}\right|_{0} + r(t) \left.\frac{\mathrm{d}^2 h}{\mathrm{d}r^2}\right|_{0}. && (5.28)
\end{aligned}$$

Combining these truncated derivatives of the hyperbolic tangent function with the approximate model Eqs. (5.23) and (5.24) we then have

$$\dot{r} \approx \varepsilon r + \varepsilon\kappa\tau_{\text{prop}} r \left[\left.\frac{\mathrm{d}f}{\mathrm{d}r}\right|_0 + r\left.\frac{\mathrm{d}^2 f}{\mathrm{d}r^2}\right|_0\right] - \kappa\left[f(0) + r\left.\frac{\mathrm{d}f}{\mathrm{d}r}\right|_0\right]\left[1 + \kappa\tau_{\text{prop}}\left(\left.\frac{\mathrm{d}f}{\mathrm{d}r}\right|_0 + r\left.\frac{\mathrm{d}^2 f}{\mathrm{d}r^2}\right|_0\right)\right] \tag{5.29}$$

$$+ \kappa\tau_{\text{prop}}\left[\left.\frac{\mathrm{d}f}{\mathrm{d}r}\right|_0 + r\left.\frac{\mathrm{d}^2 f}{\mathrm{d}r^2}\right|_0\right] s + s$$

$$\dot{s} \approx -\gamma\left[h(0) + r\left.\frac{\mathrm{d}h}{\mathrm{d}r}\right|_0\right] + \gamma\tau_{\text{vis}}\left[\left.\frac{\mathrm{d}h}{\mathrm{d}r}\right|_0 + r\left.\frac{\mathrm{d}^2 h}{\mathrm{d}r^2}\right|_0\right]\left[\varepsilon r - \kappa\left(f(0) + r\left.\frac{\mathrm{d}f}{\mathrm{d}r}\right|_0\right) + s\right]. \tag{5.30}$$

Keeping $\mathcal{O}(r)$, $\mathcal{O}(\tau_{\text{prop}})$ and $\mathcal{O}(\tau_{\text{vis}})$ only, where $f(0) = h(0) = 0$ and defining

$$A_{11} = \left.\frac{\mathrm{d}f}{\mathrm{d}r}\right|_0 \qquad A_{12} = \left.\frac{\mathrm{d}^2 f}{\mathrm{d}r^2}\right|_0$$
$$A_{21} = \left.\frac{\mathrm{d}h}{\mathrm{d}r}\right|_0 \qquad A_{22} = \left.\frac{\mathrm{d}^2 h}{\mathrm{d}r^2}\right|_0$$

the approximate model equations become

$$\dot{r} \approx \varepsilon r + \varepsilon\kappa\tau_{\text{prop}} r A_{11} - \kappa r A_{11}\left(1 + \kappa\tau_{\text{prop}} A_{11}\right) + \kappa\tau_{\text{prop}} A_{11} s + \kappa\tau_{\text{prop}} A_{12} r s + s$$
$$\dot{s} \approx -\gamma r A_{21} + \gamma\tau_{\text{vis}}\left(A_{21} + r A_{22}\right)\left[r\left(\varepsilon - \kappa A_{11}\right) + s\right].$$

However, since $\kappa\tau_{\text{prop}} A_{12} r s$, $\left(\varepsilon - \kappa A_{11}\right) A_{22} r^2$ and $A_{22} r s$ are $\mathcal{O}(2)$, we have to $\mathcal{O}(1)$:

$$\dot{r} \approx \varepsilon r + \varepsilon\kappa\tau_{\text{prop}} r A_{11} - \kappa r A_{11}\left(1 + \kappa\tau_{\text{prop}} A_{11}\right) + \kappa\tau_{\text{prop}} A_{11} s + s$$
$$\dot{s} \approx -\gamma r A_{21} + \gamma\tau_{\text{vis}} A_{21}\left[r\left(\varepsilon - \kappa A_{11}\right) + s\right]$$

and after grouping terms we are left with

$$\dot{r} \approx \left[\varepsilon + \varepsilon\kappa\tau_{\text{prop}} A_{11} - \kappa A_{11}\left(1 + \kappa\tau_{\text{prop}} A_{11}\right)\right] r + \left(1 + \kappa\tau_{\text{prop}} A_{11}\right) s \tag{5.31}$$
$$\dot{s} \approx \left[-\gamma A_{21} + \gamma\tau_{\text{vis}} A_{21}\left(\varepsilon - \kappa A_{11}\right)\right] r + \gamma\tau_{\text{vis}} A_{21} s. \tag{5.32}$$

If however, $f(r(t)) = h(r(t)) = r(t)$ (as in Sect. 3.5), then $A_{11} = A_{21} = 1$ and Eqs. (5.31) and (5.32) reduce to

$$\dot{r} \approx (\varepsilon - \kappa)\left(1 + \kappa\tau_{\text{prop}}\right) r + \left(1 + \kappa\tau_{\text{prop}}\right) s \tag{5.33}$$

$$\dot{s} \approx \gamma\left[(\varepsilon - \kappa)\,\tau_{\text{vis}} - 1\right] r + \gamma\tau_{\text{vis}} s. \tag{5.34}$$

Finally, we have reduced our original nonlinear DDE to a second-order linear ODE. At this point we may perform ordinary linear stability analysis.

Linear Stability Analysis

Equations (5.33) and (5.34) may be rewritten as

$$\dot{r} \approx Ar + Bs \tag{5.35}$$

$$\dot{s} \approx Cr + Ds \tag{5.36}$$

where the coefficients are

$$\begin{aligned} A &\equiv (\varepsilon - \kappa)\left(1 + \kappa\tau_{\text{prop}}\right) < 0 \\ B &\equiv \left(1 + \kappa\tau_{\text{prop}}\right) > 0 \\ C &\equiv \gamma\left[(\varepsilon - \kappa)\,\tau_{\text{vis}} - 1\right] < 0 \\ D &\equiv \gamma\tau_{\text{vis}} > 0 \end{aligned}$$

since, $\varepsilon < \kappa$. From this, we may use linear stability analysis to give an estimate, in terms of our parameters of where the system will become unstable, *i.e.*, the set of parameters where the eigenvalues of the system cross the imaginary axis. The Jacobian of the system is

$$\mathbf{A} = \begin{bmatrix} A & B \\ C & D \end{bmatrix}. \tag{5.37}$$

To find its eigenvalues we compute the characteristic equation

$$\begin{aligned} \det(\mathbf{A} - \lambda\mathbf{I}) = \begin{vmatrix} A-\lambda & B \\ C & D-\lambda \end{vmatrix} &= 0 \\ (A-\lambda)(D-\lambda) - BC &= 0 \\ \lambda^2 - (A+D)\lambda + AD - BC &= 0 \end{aligned}$$

so the eigenvalues are

$$\lambda_{1,2} = \frac{A+D}{2} \pm \frac{\sqrt{(A+D)^2 - 4\,(AD-BC)}}{2}.$$

Since we are interested in purely imaginary eigenvalues only, $A + D = 0$ must be true, which gives

$$\lambda_{1,2} = \pm i\omega_{\text{crit}} = \pm i\sqrt{BC - AD}.$$

To satisfy this condition, we must have $BC - AD < 0$ or $BC < AD$. The expansion of this inequality results in

$$\begin{aligned}
(1 + \kappa\tau_{\text{prop}})\,\gamma\left[(\varepsilon - \kappa)\,\tau_{\text{vis}} - 1\right] &< (\varepsilon - \kappa)\,(1 + \kappa\tau_{\text{prop}})\,\gamma\tau_{\text{vis}} \\
\left[(\varepsilon - \kappa)\,\tau_{\text{vis}} - 1\right] &< (\varepsilon - \kappa)\,\tau_{\text{vis}} \\
-1 &< 0
\end{aligned}$$

which is always true, therefore the critical frequency is

$$\omega_{\text{crit}} = \sqrt{(1 + \kappa\tau_{\text{prop}})\,\gamma}.$$

This is critical frequency condition satisfied by the parameters of the stability boundary. For the typical parameter values of $\kappa = 3$, $\tau_{\text{prop}} = 0.2$ and $\gamma = 0.2$, $\omega_{\text{crit}} \approx 0.565$ rad/s or $f_{\text{crit}} \approx 0.0900$ Hz. Returning to the condition $\Re\{\lambda_{1,2}\} = 0 = A + D$, gives

$$\tau_{\text{vis}} = \frac{1}{\gamma}\,(\kappa - \varepsilon)\,(1 + \kappa\tau_{\text{prop}})\,.$$

This is the condition satisfied by all the parameters at the stability boundary. Figure 5.11 shows the delay-space stability diagram of the small-delayed approximation (without noise), where the feedback functions are linear, for the fixed set of parameters ε, κ, and γ. In each subfigure of Fig. 5.11 ((a), (b), and (c)), only ε is varied. As ε approaches κ, the stable regime becomes smaller and therefore, the unstable regime grows, which is expected [37]. However, this contrasts with the regions of stability found in Sect. 3.5.5 that are mostly dependent on the proprioceptive delay τ_{prop}. It is important to note that even with the small delay approximation which removes the explicit time dependence of the delay, it is still possible to obtain oscillatory solutions, *i.e.*, $\lambda_{1,2} \in \mathbb{C}$.

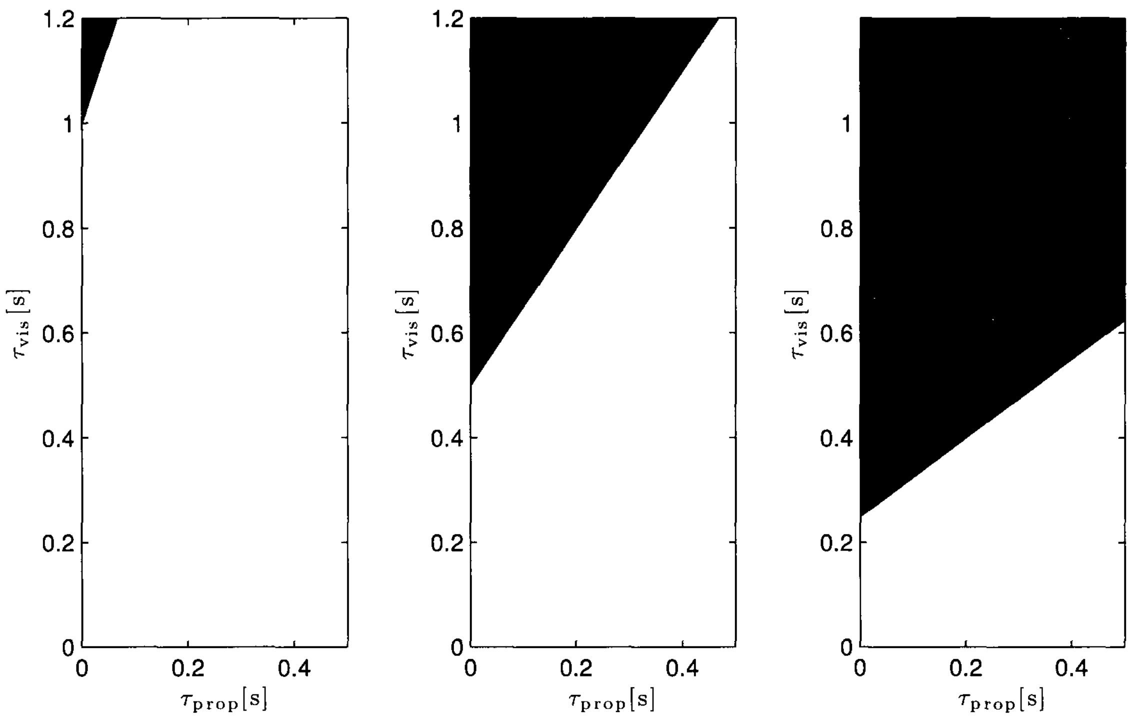

(a) $\varepsilon = 2.8, \kappa = 3, \gamma = 0.2$ (b) $\varepsilon = 2.9, \kappa = 3, \gamma = 0.2$ (c) $\varepsilon = 2.95, \kappa = 3, \gamma = 0.2$

Figure 5.11 – Stability of the model in delay-space via the small delay approximation. White represents the stable regime whereas black represents unstable regime.

5.4.2 Stability of the Nonlinear Deterministic Model

Recall Fig. 3.8(d) in which the stability region was shown in terms of the proprioceptive and visual delays. We will explore this stability region in a larger range of the parameters κ and γ, the proprioceptive and visual strengths, respectively. To detect unbounded solutions, we assumed divergence of the solution, or an increasing envelope. Similarly, we assumed a decreasing envelope for the fixed point solution, and a constant envelope for the oscillatory or limit cycle solution.

All combinations of parameters in Fig. 5.12 return a stability region similar to the one displayed in Fig. 3.8(d) except for Fig. 5.12(b) where the stability region becomes smaller as the proprioceptive strength κ gets closer to the rescaled inertial term ε. Another difference is that the oscillatory solution region is thicker in Fig. 5.12 due to the hyperbolic tangent nonlinearity. In other words, since the nonlinear terms are included, the system admits bounded oscillatory solutions (for limit cycles, see Sect. 2.3). These are seen over a larger are of parameter space compared to the marginally stable oscillatory solutions determined numerically for the linear system.

5.5 Summary

This chapter has extended the analysis of the model (Eqs. (3.11) and (3.12)) put forth in Chap. 3. Alternative models have been explained to show the development of the final model. Aspects of analysis of the linear and nonlinear model have also been given. For the linear model, numerical solutions to the eigenvalues have been found, supporting the results from the stability regime given in Chap. 3. The power spectral density has shown that the linear and nonlinear model contain the same frequency components in the stable experimental operating range. We have also shown that the musculoskeletal noise intensity is more dominant than the 'drift' noise intensity across all experimental conditions. For the nonlinear model, we have performed a small delay approximation to remove the explicit inclusion of the delay terms. This analysis yielded a two approximate SDEs of two SDDEs (Eqs. (3.11) and (3.12)). Upon linearization of the SDEs, linear stability analysis of Eqs. (5.35) and (5.36) (for the deterministic case, where $a_r = a_s = 0$) showed that there exists a boundary between the fixed point and unbounded regimes (in terms of the proprioceptive and visual delay space), yet the eigenvalues do not completely agree with the numerical results of Chap. 3. The results of a center manifold analysis of Eqs. (3.11) and (3.12) (where $a_r = a_s = 0$) may return evidence of the existence limit cycle solutions, however, such an analysis is not trivial. Yet, the added complexity of the nonlinear model is not needed for the experimental set of parameters (shown in Appendix B), hence, such analysis is deemed unnecessary for understanding the theoretical basis of this experiment. Finally, we presented the stability boundaries (via numerical techniques)

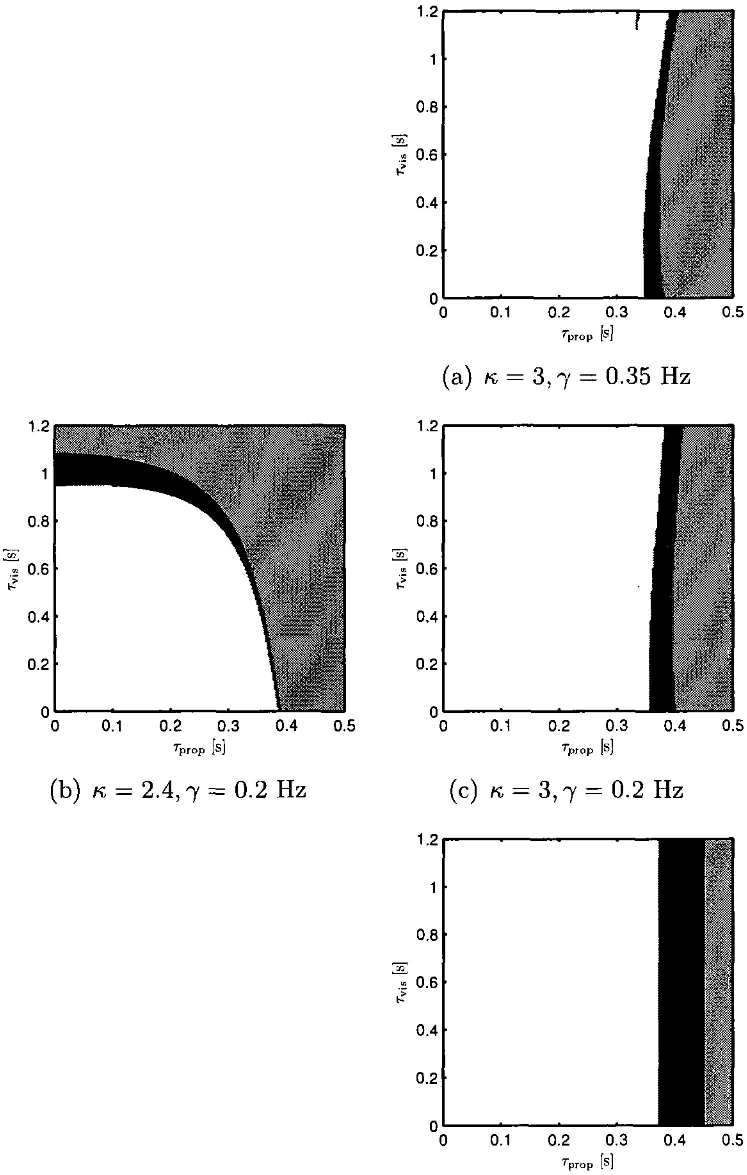

(a) $\kappa = 3, \gamma = 0.35$ Hz

(b) $\kappa = 2.4, \gamma = 0.2$ Hz

(c) $\kappa = 3, \gamma = 0.2$ Hz

(d) $\kappa = 3.2, \gamma = 0.2$ Hz

(e) $\kappa = 3, \gamma = 0$ Hz

Figure 5.12 – Delay-space stability diagrams of the nonlinear model, Eqs. (3.5) and (3.10). Fixed point solutions are shown in white, marginally stable oscillatory solutions are black and unbounded solutions are shown in grey.

of the nonlinear model which differ with the stability boundaries of the linear model (*cf.* Sects. 3.5.5 and 5.4.2) by having a larger regime of marginally stable oscillatory solutions.

Chapter 6

Results of Nonlinear Time Series Analysis

6.1 Introduction

The postural system has many degrees of freedom (DOF) given by the space of joint positions (which is equal to the number of joints times the number of spatial dimensions, *i.e.*, approximately 27). However, not all possible DOF must be recruited to complete a postural task with a relatively small range of motion. Furthermore, it is not trivial to determine the number of active DOF used in such a task from the COP trajectory since all active degrees of freedom are projected onto the anteroposterior-mediolateral (xy) plane. Nevertheless, it is possible to estimate the number of active DOF using phase space reconstruction when the data are relatively noise-free and the dimension of the underlying dynamics is small.

If DOF $\geqslant 3$, deterministic chaos may be present given the combination of nonlinearity of the dynamics and the presence of time delays. Another problem inherent to the analysis of finite COP datasets is the distinction between high dimensional chaos and noise. This consideration arises from the fact that chaos is sometimes indistinguishable from noise (given the high dimensionality of noise) if the embedding dimension is too low (see Sect. 2.8.1). This distinction is crucial because chaos may ensue from a deterministic control mechanism.

Further, there is always some noise present. To address these issues, we began preliminary examinations into the dynamical structure of experimental COP trajectories with visual feedback manipulations via recurrence quantification analysis (RQA), largest Lyapunov exponent (LLE) and mean-squared displacement (MSD) analyses to quantify the influence of DVF on the dynamical structure present in time series and the complexity of COP dynamics.

RQA is not a new technique in the realm of COP data analysis as numerous experiments [11, 64, 62, 70] have made use of it. The Largest Lyapunov Exponent, traditionally the indicator of chaotic behavior (if it is positive), is also prominent in the postural control literature [17, 56, 65, 85]. These studies have shown that experimental LLEs are positive, implying the presence of local exponential divergence in postural dynamics. Finally, the MSD has been used in quantifying the level of sub- and super-diffusion for postural dynamics [12, 14].

6.2 Results

6.2.1 Phase Space Reconstruction

Since phase space reconstruction is required for RQA and LLE, it is important to visually understand the concept. Figure 6.1 shows the COP embedded in three dimensions, for three trials, each corresponding to a different experimental condition for one participant. Notice how the trajectories overlap onto themselves and there is no clear structure, therefore the embedding dimension of 3 is not high enough to enable complete unfolding of the COP—if such an unfolding exists. Similar results are seen across conditions and across participants.

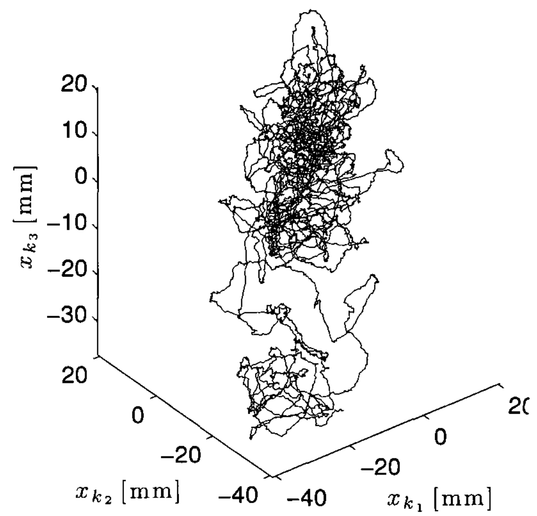

(a) Eyes closed.

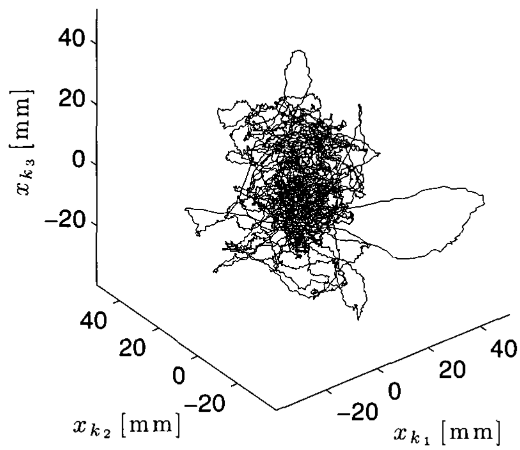

(b) DVF at 0 ms.

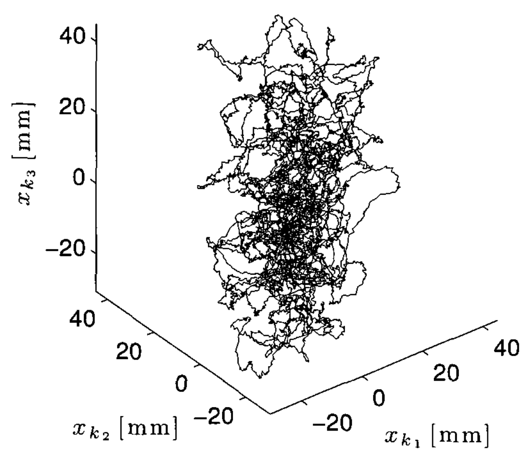

(c) DVF at 750 ms.

Figure 6.1 – Phase space reconstruction of COP in three dimensions where $k_1 = 1, \dots, N-2\tau$, $k_2 = \tau + 1, \dots, N - \tau$ and $k_3 = 2\tau + 1, \dots, N$. For the lags, see Table 4.2.

6.2.2 Recurrence Quantification Analysis

Next we show the recurrence plots (see Sect. 2.8.2) of one participant for trials three and five of all conditions in Figs. 6.2 and 6.3 respectively. The recurrence plots in Figs.

6.2(a) and 6.3(a), representing the no vision condition, are typically more sparse than the other conditions. Indeed, since reconstructed space is normalized by the maximum of its Euclidean norm, and since there is more drift in this condition which results in larger and less frequent corrections, only the neighborhood surrounding these resultant large excursions are deemed "recurrent". However, for the DVF conditions, shown in Figs. 6.2 and 6.3, (b)–(f), there appears to be more frequent recurrences, in smaller clusters. The bounds of the reconstructed COP are smaller and therefore there is a higher density of points in the space, hence more recurrent points. We also see that the DVF conditions display a more 'periodic' behavior due to the many small clusters of recurrent points than the no vision condition, whereas the power spectral density does not reveal such features (see Sect. 2.8.2).

In Fig. 6.4 we show that the mean recurrence rate is within the allowed range of 0.01 to 2 percent, even within the bounds of error. This is the only measure we present here since other detailed measures and their interpretation are beyond the scope of this thesis. Yet, much more information is contained in these recurrence plots about the COP data. The term RQA, or recurrence quantification analysis refers to a set of approximately fifteen measures derived from the recurrence plot [49, 46, 48, 47, 74].

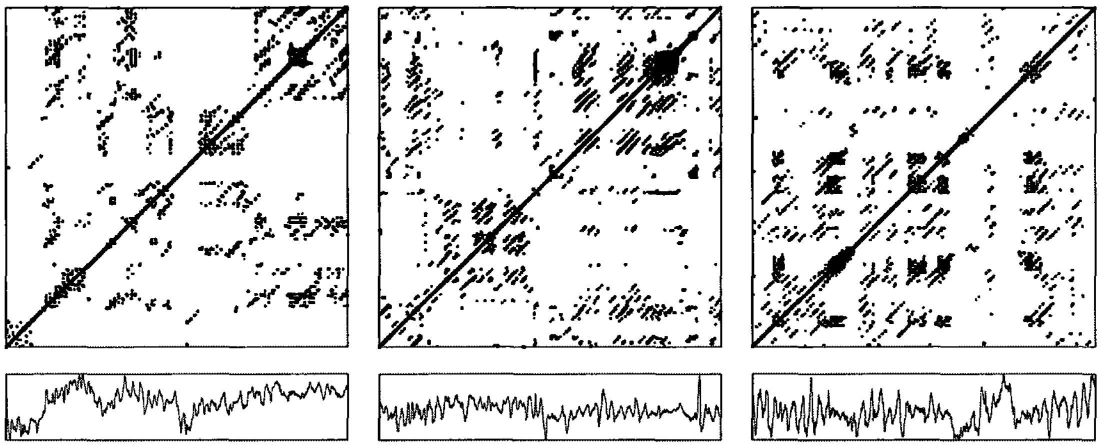

(a) Eyes closed, $\epsilon = 5$ percent. (b) DVF at 0 ms, $\epsilon = 6$ percent. (c) DVF at 250 ms, $\epsilon = 6$ percent.

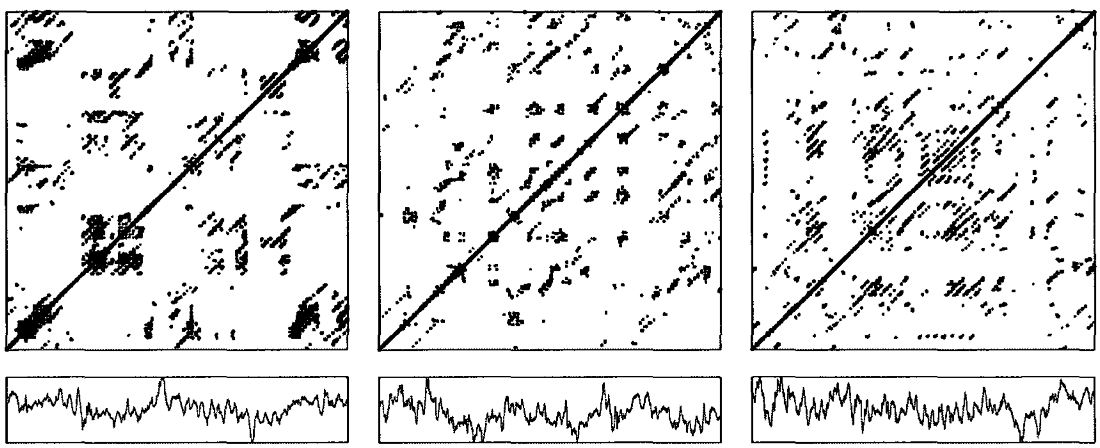

(d) DVF at 500 ms, $\epsilon = 6$ percent. (e) DVF at 750 ms, $\epsilon = 6$ percent. (f) DVF at 1000 ms, $\epsilon = 6$ percent.

Figure 6.2 – Recurrence plots of postural sway from subject KT where black dots represent 1 and white, 0 (see Eq. (2.64) for $\mathbf{R}_{i,j}$). These plots are for the third trial of each condition. All recurrence plot axes are in units of time for 0 to 115 seconds, for a total of 11500 data points. The data used to generate each recurrence plot appear below.

6.2.3 Largest Lyapunov Exponent

We use the same PSR parameters that we used for RQA to reconstruct the COP in embedding dimensions 1 to 8. Notice how Fig. 6.5 shows that the slope of $\langle \ln(\text{div}) \rangle$ in the range 0 to 0.5 seconds decreases with increasing embedding dimension.

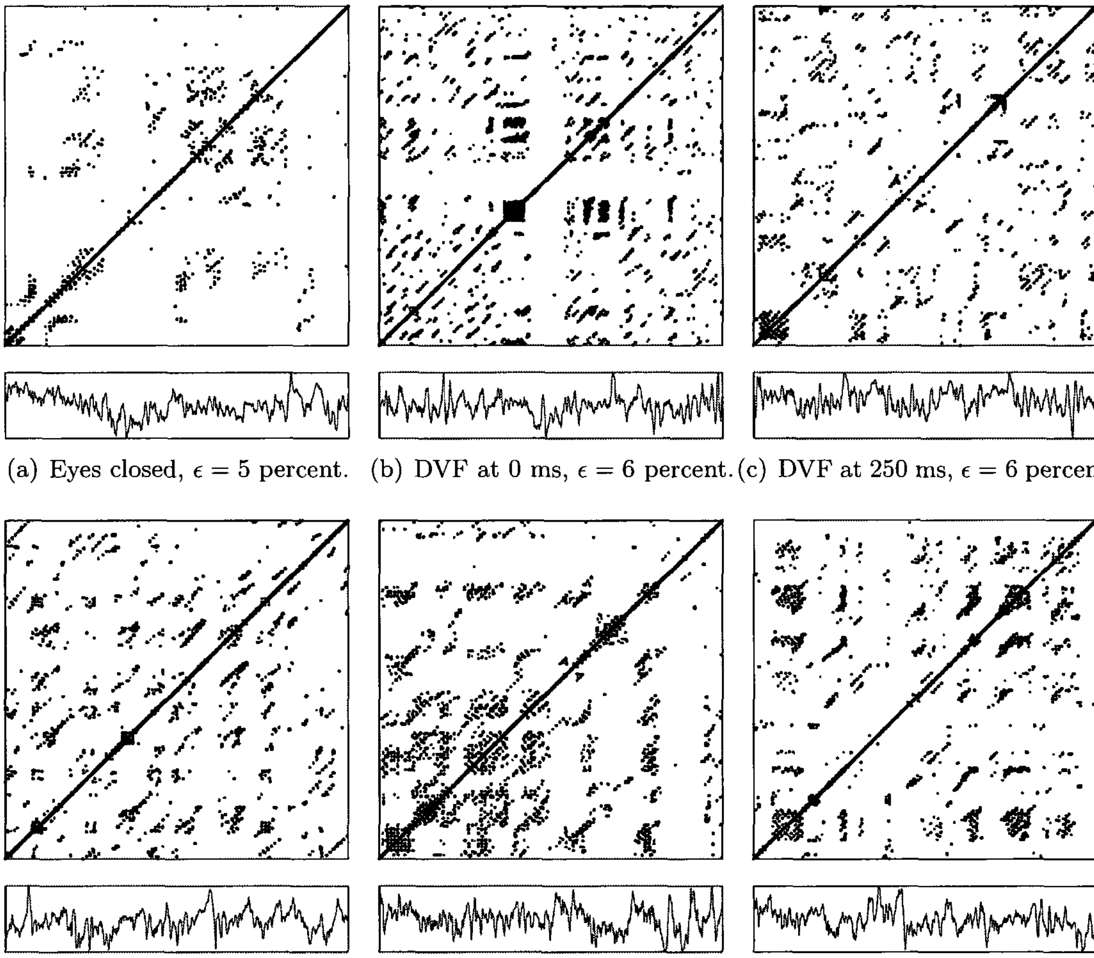

(a) Eyes closed, $\epsilon = 5$ percent. (b) DVF at 0 ms, $\epsilon = 6$ percent. (c) DVF at 250 ms, $\epsilon = 6$ percent.

(d) DVF at 500 ms, $\epsilon = 6$ percent. (e) DVF at 750 ms, $\epsilon = 6$ percent. (f) DVF at 1000 ms, $\epsilon = 6$ percent.

Figure 6.3 – Recurrence plots of postural sway from subject KT where black dots represent 1 and white, 0 (see Eq. (2.64) for $\mathbf{R}_{i,j}$). These plots are for the fifth trial of each condition. All recurrence plot axes are in units of time for 0 to 115 seconds, for a total of 11500 data points. The data used to generate each recurrence plot appear below.

Figure 6.6 shows the largest Lyapunov exponents for all conditions. It is clear that for all conditions, λ_1 does not saturate even at dimension $\leqslant 8$. This is typical of stochastic systems, due to the high dimensionality, or of deterministic systems with a strong noise component. In such cases, a suitable low dimensional embedding space is a hard criterion to satisfy. As shown in Fig. 6.6, there exists no convergence of the LLE, so this type

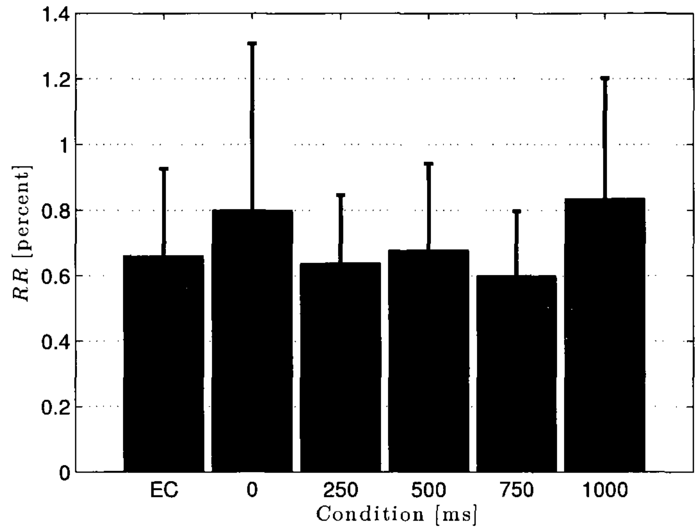

Figure 6.4 – RQA measure RR for all conditions where error bars denote inter-subject standard deviations.

of analysis for this data set is inconclusive in terms of revealing low-dimensional deterministic behavior. Rather it suggests the involvement of a significant noise component. Not only is there is a lack of convergence as the embedding dimension increases, there is also a lack of significant differences between experimental conditions of λ_1, a pattern emerges which shows that the condition with the lowest LLE is the eyes closed or no vision condition. In contrast, the 250 ms DVF condition has the highest LLE.

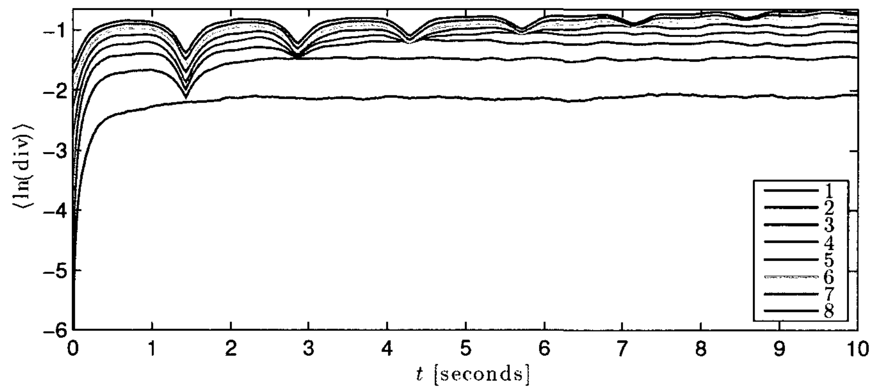

(a) Eyes closed.

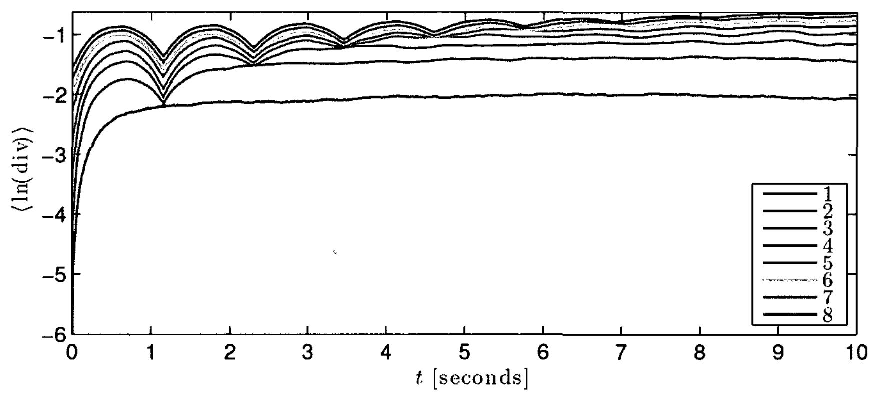

(b) DVF at 0 ms.

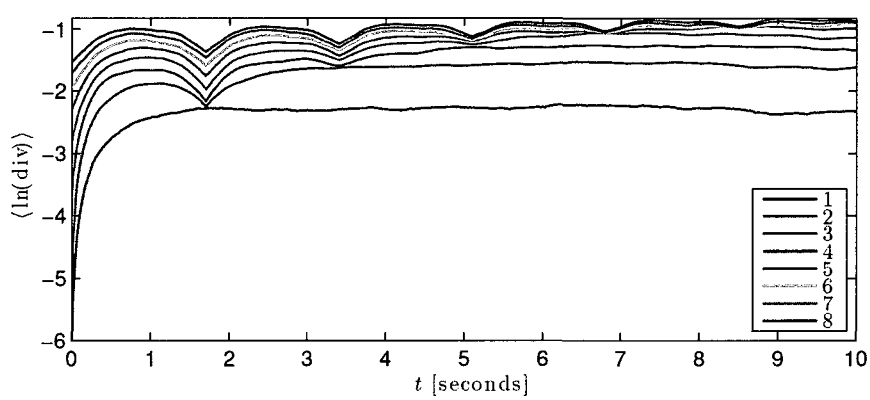

(c) DVF at 750 ms.

Figure 6.5 – Exponential divergence of subject KT for embedding dimensions $d \in \{1, \ldots, 8\}$. These plots are for the fifth trial of each condition.

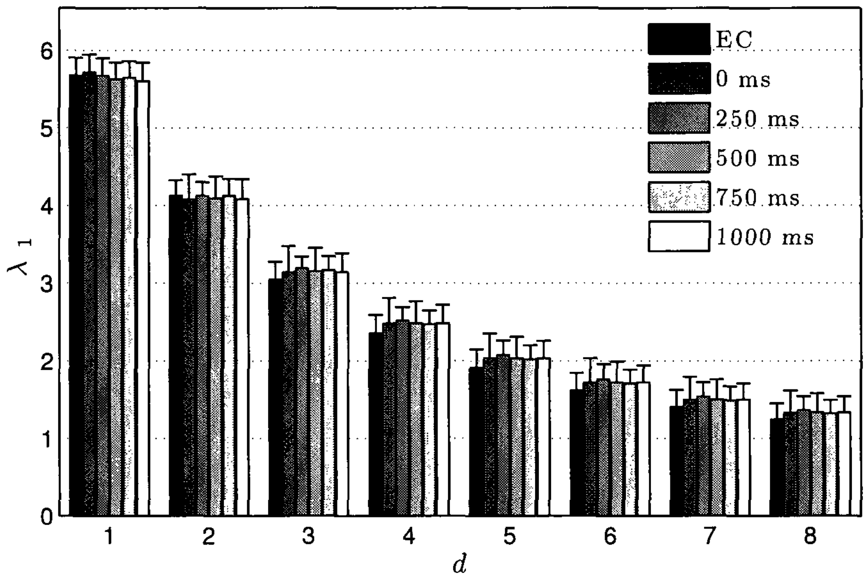

Figure 6.6 – Largest Lyapunov exponent as a function of embedding dimension; error bars denote inter-subject standard deviations.

6.2.4 Mean-Squared Displacement

Finally, we elaborate on the mean-squared displacement data to show its reliability across all trails and participants. Figure 6.7 shows the MSD for the fifth trial of one subject for experimental conditions: no vision, 0 ms and 750 ms DVF. There is a clear linear portion before τ_c, responsible for the short-time scale Hurst exponent H_s. However, past τ_c, more varied patterns are found.

We then averaged all five trials for each condition separately, for the same participant and display the MSD of each trial along with the average MSD of these trials in Fig. 6.8. Notice how the average MSD shows more regularity beyond τ_c than it did for individual trials and approaches linearity. Some information is lost in averaging the MSDs since in the DVF conditions, a few MSDs show oscillatory behavior beyond τ_c. This pattern has been found in another work (experiment and model) [53], in which the model of the postural controller was of a delayed, discontinuous nature rather than of a continuous nature as in our model (see Sect. 3.5).

Finally, we lumped all average-subject MSDs into an average MSD across all partic-

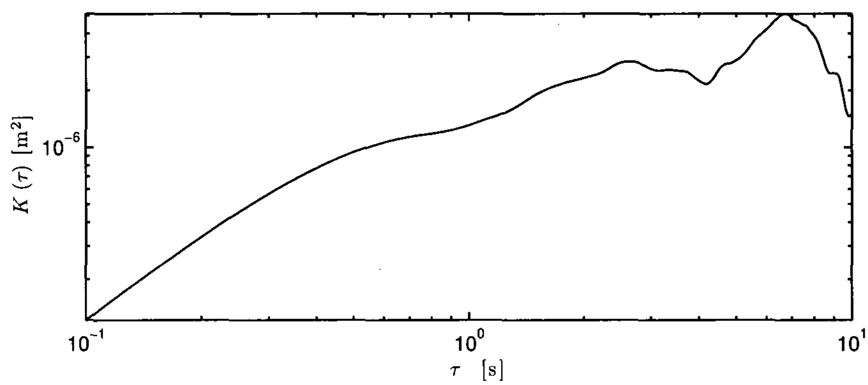

(a) Eyes closed.

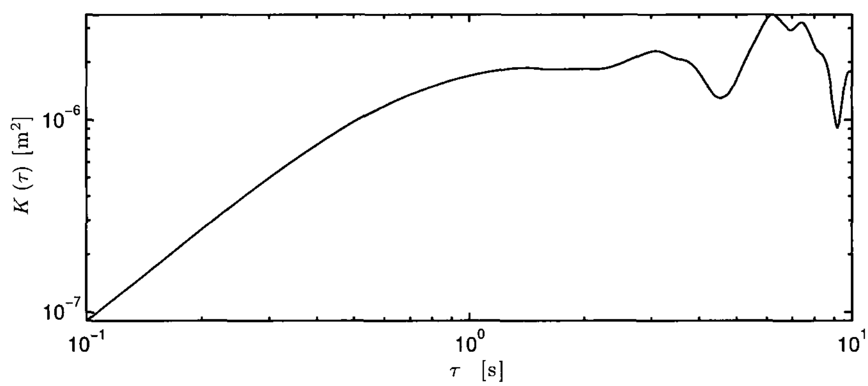

(b) DVF at 0 ms.

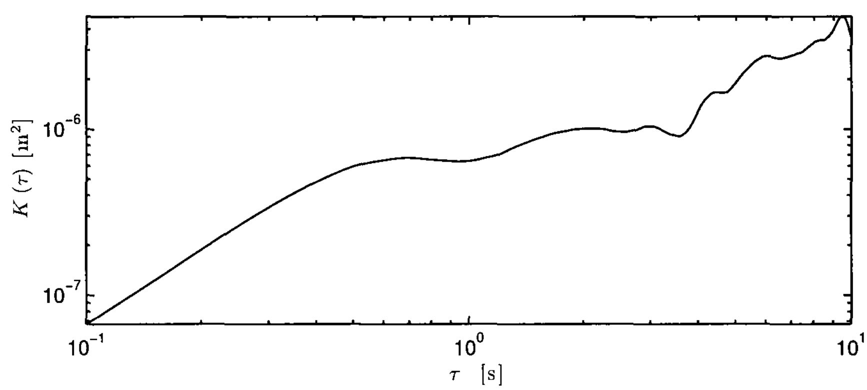

(c) DVF at 750 ms.

Figure 6.7 – Mean-squared displacement for one trial of subject KT.

ipants in Fig. 6.9. The average MSD of all participants is linear before τ_c and almost linear after τ_c. From this curve, we extract the slopes of $K(\tau)$ on either side of τ_c to give

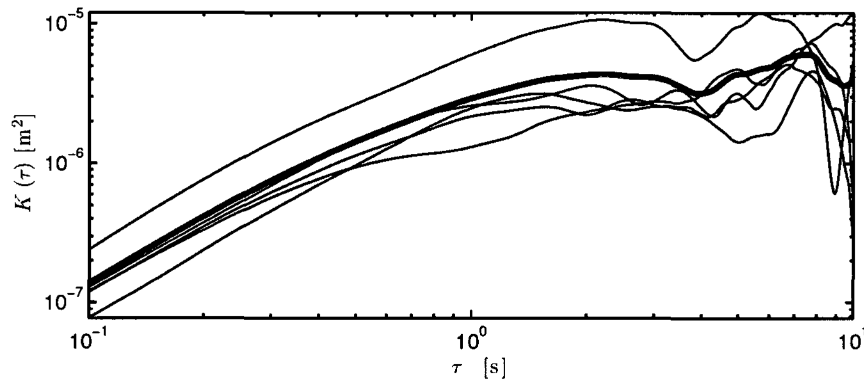

(a) Eyes closed.

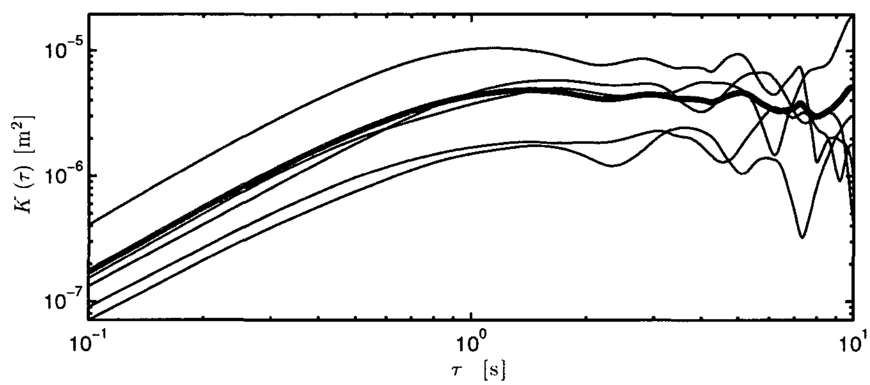

(b) DVF at 0 ms.

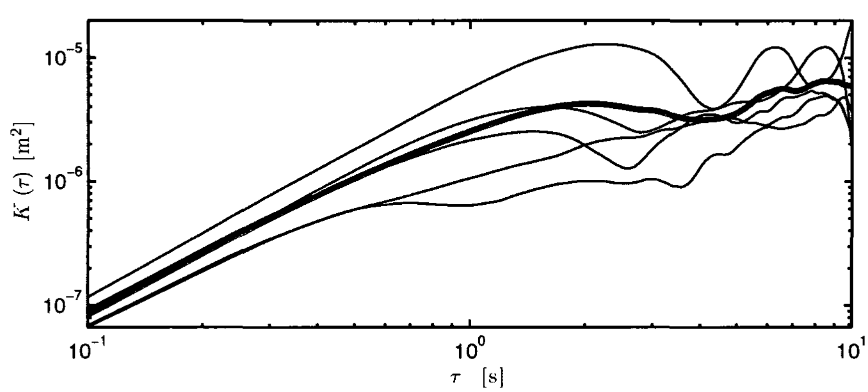

(c) DVF at 750 ms.

Figure 6.8 – Mean-squared displacement for subject KT displayed for all five trials and for the conditions (a) eyes closed, (b) DVF at 0 ms and (c) DVF at 750 ms. The thick blue corresponds to the MSD averaged across all trials.

$2H_s$ and $2H_l$, respectively. These results are given in Chap. 3.

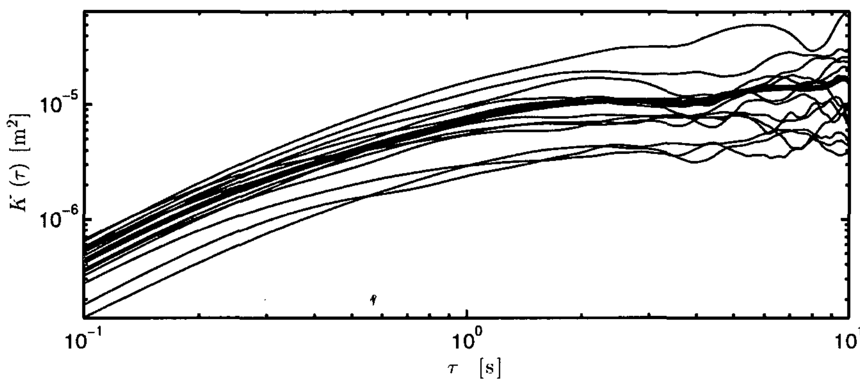

(a) Eyes closed.

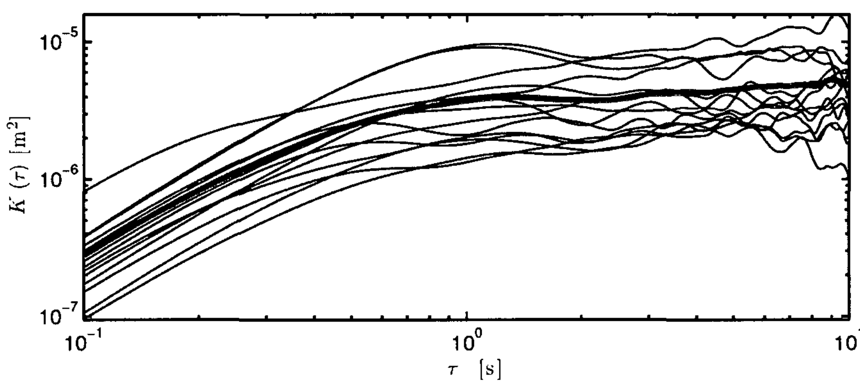

(b) DVF at 0 ms.

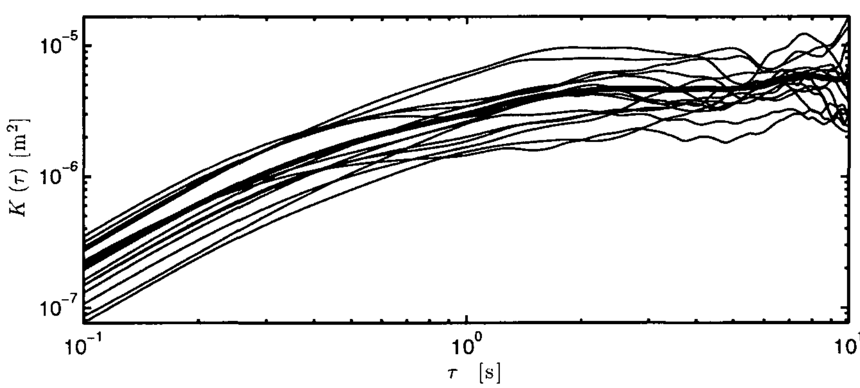

(c) DVF at 750 ms.

Figure 6.9 – Mean-squared displacement displayed for all subjects displayed and for the conditions (a) eyes closed, (b) DVF at 0 ms and (c) DVF at 750 ms. The thick red line corresponds to the MSD averaged over all subjects.

6.3 Discussion

This chapter has applied a few methods of time series analysis applied to COP data. RQA generally shows promise in the presence of noise since [75] has given criterion for selecting the optimal threshold (ϵ) value to determine if recurrence occurs. Whether this is applicable to our data is yet unknown since the full nature of 'noise' is not yet known for our system. Future investigations will include more RQA measures to estimate the deterministic structure of the COP data.

The largest Lyapunov exponent has been shown to be, for the large part, unreliable for our COP data. Perhaps, when the structure of the noise is better understood, a nonlinear filter may be applied to the data to remove the noise so that more valid estimates of the LLE may be obtained.

A future possibility that may apply to these data directly is to validate the measure of any statistic (RQA, LLE, and MSD) by performing surrogate analysis to the data. Essentially, this provides a null hypothesis, whereby the statistical significance of the measure may be tested. This is done by randomly shuffling the phase and preserving the variance of the data before computing the RQA measures and LLE and then repeating the analysis and deciding on wether there is a statistically significant difference. Since RQA and LLE analysis are computationally intensive processes, only the COP data have been processed; it would take a lot more computational time to perform surrogate analysis. To further validate our model from Chap. 3, we will analyze it using the measures described here as well as surrogate analysis.

Finally, using PSR to estimate the dimensionality (embedding dimension) of COP data is a bottom-up approach to the problem. A top-down solution to gather more information about the dimensionality of the postural system would be to experimentally use a motion capture device to record the position (in three dimensions) of markers placed at all joints (and the head). After this, we would construct an orthogonal space of the dimension of the number of time series by computing a covariance matrix. This could be done by computing the covariance of the permutation of all time series. All elements of the covariance matrix are then normalized by the trace of the matrix. Finally, a singular value decomposition would be done on the covariance matrix to return the corresponding eigenvalues. After ordering the magnitude of eigenvalues in a descending fashion, the sum of eigenvalues (starting from the first) that equal 90 percent of the summed eigenvalues, is the effective dimension of the system *i.e.*, the number of degrees of freedom that underlie most of the system's motions. This algorithm is known as principal component analysis [15] and may yield an interesting lower dimensional projection of the postural dynamics influenced by delayed visual feedback.

Chapter 7

Conclusions

This thesis presents a framework for sensory-postural experimentation, modeling and analysis. In particular, we focused on modulating input to the visual system to perturb the postural control system since experimentally, it is difficult to perturb proprioception. We have modulated visual input experimentally by varying the time delay of the visual feedback, which is center of pressure information. We have also removed visual feedback in some instances. We have also modeled the human postural system using simplified nonlinear delay-differential equations. Since the human postural system is unstable without sensory feedback, because we are essentially inverted pendula, it is imperative to know how much feedback is necessary for stability and what the boundaries of stability are. The last part of the thesis contains preliminary nonlinear time series analysis on the COP time series. These revealed the dynamics to be rather noisy and/or high dimensional.

Based on sensory information, the brain makes decisions on how to move the body in a postural task. These decisions translate into movements of body segments. Experimental work on postural sway is usually limited to force plate recordings which are center of pressure measurements. These recordings are just the kinetics of all joints, projected downwards. Therefore if we consider the difference between recorded information (COP) and high-level commands generated in the brain, there is certainly some error.

However, it is not feasible to directly record brain signals due to ethical reasons, and due to the vast density of brain matter which makes it difficult to remove the contribution from neighboring parts. It is easier to change the sensory inputs in a systematic fashion and record the postural output to gain insight into the brain's control. Here we have been concerned with two types on sensory input or feedback, namely proprioception and vision. Since small sensors located in joints and in the feet are used for proprioception, it is difficult to change this sense without drugs or some invasive technique. Therefore the only sensory input that may be exploited non-invasively is vision. This may require special implementation when applied to subjects whose postural control is already impaired, such as the elderly.

In an attempt to model this experimentally recorded COP given the state of visual feedback, we have extended the continuous control model by Yao *et al.* [86] which does not explicitly account for the differential visual inputs. Additionally, we used a novel slow-moving 'drifting fixed point' to account for the large difference in spectral power at low frequencies observed for cases with no visual feedback relative to cases with visual feedback.

The Hurst exponents, quantify the level of corrections or correlations (positive or negative) in the data. We have found that our model generates short- and long-range Hurst exponents that agree well with the behavior of the data. Also, the short-range Hurst exponents do not vary significantly over any of the experimental conditions, an observation that is reproduced by our model. In particular, the long-range Hurst exponents show the same qualitative pattern between the data and model: for no vision, the exponent is higher, indicating there is less control of negative corrections. This is logical given that there is less sensory information due to the lack of vision. For the conditions in which there is delayed visual feedback, the long-range Hurst exponents increase as a function of the delay. And although the trend is not significant, it implies that since there are less corrections at larger visual delays, the visual information is less reliable. The comparative difference between vision and no vision long-range Hurst exponents agrees with experimental data by Collins and DeLuca [14] (even though they did not consider delayed visual feedback). The model has shown that proprioceptive delay is the dominant delay for postural control, probably since proprioception alone must stabilize upright human stance when vision is not available or reliable.

However, it is not as straightforward to assume that more sensory information will better stabilize the system. We have shown by theoretical analysis that more visual feedback destabilizes the model when it is greater than a critical value. We have also numerically shown that proprioceptive delay may destabilize the system by exceeding certain values as well, assuming a constant set of parameters.

Future work will be done on comparing RQA results obtained for models and experimental data. Another problem left unsolved is that of the complete bifurcation analysis of the nonlinear (hyperbolic tangent) model. Once sensory information has passed a linear stability boundary, more input will allow the system to remain stable, but perhaps in an oscillatory state. Therefore, for larger sensory perturbations which move the system outside the fixed point regime, the hyperbolic tangent functions are likely to play a significant role to constrain the resulting motion.

On the experimental front, we must obtain as much information as possible to corroborate and hopefully ameliorate our postural control model. For this thesis, we have only used center of pressure data provided by a force plate. To establish better estimates for proprioceptive and visual delays, recordings from the activation of the human *cortex*, specifically the motor cortices and the muscles along with joint kinematics should be compared. Good candidates for cortex recordings comprise magnetoencephalography (MEG) and electroencephalography (EEG). As for the body recordings, for muscle activation we have electromyography (EMG) and joint kinematics may be recorded via a motion capture system to obtain better estimates for the behavior of the more realistic, higher-dimensional system. Due to decreased receptor sensitivity with age, the proprioceptive delay increases, therefore, measurements should take this into account. However, the same is not true for the visual delay.

Finally, it would be interesting to perform special investigations of disruption of motor control loops on patients with neural deficiencies or brain lesions. Patients with anterior cruciate ligament deficiency have an effective lack of proprioception. This deficiency can be quantified by measuring the neural conduction velocity from foot to spinal chord. Lesions of the supplementary motor area, a specific area of the cerebral cortex known for planning motor trajectories, could also be monitored by recording electrical and magnetic fields with EEG and MEG, respectively. The analysis of postural control data from such patients, using the methods presented in this thesis, would provide valuable information to deepen our understanding of how we stand up, and how we fall.

Appendix A

Code

A.1 Model

A.1.1 Eqs. (3.11) and (3.12): model2DparOBMsepRS.m

```
function [r,s] = model2DparOBMsepRS(N,h,d,dv,a)
%% PARAMETERS
%% DELAY CONDITIONS
%% Proprioceptive delay
M = d(1);
%% Artificial visual + visual respone delay
L = d(2) + dv;
%% Determining largest delay
K = max(M,L);
%% CREATING NOISE VECTORS
nr = a(4)*sqrt(h)*randn(1,N+K+1);
ns = a(5)*sqrt(h)*randn(1,N+K+1);
%% INITIAL (HISTORY) FUNCTIONS
% Positions (Brownian)
r(K+1:N+K) = 0;
r(1:K) = cumsum(nr(1:K));
s(K+1:N+K) = 0;
s(1:K) = cumsum(ns(1:K));
%% Euler Maruyama Integration
for i = K+1:N+K,
    r(i+1) = r(i) + ( a(1)*r(i) - a(2)*r(i-M) + s(i) )*h + nr(i);
    s(i+1) = s(i) + ns(i) - a(3)*r(i-L)*h;
```

```
end
s = s(K+1:N+K);
r = r(K+1:N+K);
end
```

A.2 Experiment

A.2.1 GUI.m

```
function varargout = GUI(varargin)
% GUI M-file for GUI.fig
%      GUI, by itself, creates a new GUI or raises the existing
%      singleton*.
%
%      H = GUI returns the handle to a new GUI or the handle to
%      the existing singleton*.
%
%      GUI('CALLBACK',hObject,eventData,handles,...) calls the local
%      function named CALLBACK in GUI.M with the given input arguments.
%
%      GUI('Property','Value',...) creates a new GUI or raises the
%      existing singleton*.  Starting from the left, property value pairs are
%      applied to the GUI before GUI_OpeningFcn gets called.  An
%      unrecognized property name or invalid value makes property application
%      stop.  All inputs are passed to GUI_OpeningFcn via varargin.
%
%      *See GUI Options on GUIDE's Tools menu.  Choose "GUI allows only one
%      instance to run (singleton)".
%
% See also: GUIDE, GUIDATA, GUIHANDLES

% Edit the above text to modify the response to help GUI

% Last Modified by GUIDE v2.5 02-Mar-2009 12:03:15


% Begin initialization code - DO NOT EDIT
gui_Singleton = 1;
gui_State = struct('gui_Name',       mfilename, ...
                   'gui_Singleton',  gui_Singleton, ...
```

```
                   'gui_OpeningFcn', @GUI_OpeningFcn, ...
                   'gui_OutputFcn',  @GUI_OutputFcn, ...
                   'gui_LayoutFcn',  [] , ...
                   'gui_Callback',   []);
if nargin && ischar(varargin{1})
    gui_State.gui_Callback = str2func(varargin{1});
end

if nargout
    [varargout{1:nargout}] = gui_mainfcn(gui_State, varargin{:});
else
    gui_mainfcn(gui_State, varargin{:});
end
% End initialization code - DO NOT EDIT

% --- Executes during object creation, after setting all properties.
function figure1_CreateFcn(hObject, eventdata, handles)
% hObject    handle to figure1 (see GCBO)
% eventdata  reserved - to be defined in a future version of MATLAB
% handles    empty - handles not created until after all CreateFcns called

% --- Executes just before GUI is made visible.
function GUI_OpeningFcn(hObject, eventdata, handles, varargin)
% This function has no output args, see OutputFcn.
% hObject    handle to figure
% eventdata  reserved - to be defined in a future version of MATLAB
% handles    structure with handles and user data (see GUIDATA)
% varargin   command line arguments to GUI (see VARARGIN)

% Choose default command line output for GUI
handles.output = hObject;

INITDATA;

% UIWAIT makes GUI wait for user response (see UIRESUME)
uiwait(handles.figure1);

% --- Outputs from this function are returned to the command line.
function varargout = GUI_OutputFcn(hObject, eventdata, handles)
% varargout  cell array for returning output args (see VARARGOUT);
% hObject    handle to figure
% eventdata  reserved - to be defined in a future version of MATLAB
```

```
% handles    structure with handles and user data (see GUIDATA)

% Get default command line output from handles structure
varargout{1} = handles.output;

% --- Executes on button press in pushbutton1.
function pushbutton1_Callback(hObject, eventdata, handles)
% hObject    handle to pushbutton1 (see GCBO)
% eventdata  reserved - to be defined in a future version of MATLAB
% handles    structure with handles and user data (see GUIDATA)

set(handles.pushbutton1, 'Enable', 'off');
STARTDEVICE;

function edit1_Callback(hObject, eventdata, handles)
% hObject    handle to edit1 (see GCBO)
% eventdata  reserved - to be defined in a future version of MATLAB
% handles    structure with handles and user data (see GUIDATA)

% Hints: get(hObject,'String') returns contents of edit1 as text
%        str2double(get(hObject,'String')) returns contents of edit1 as a double

% --- Executes during object creation, after setting all properties.
function edit1_CreateFcn(hObject, eventdata, handles)
% hObject    handle to edit1 (see GCBO)
% eventdata  reserved - to be defined in a future version of MATLAB
% handles    empty - handles not created until after all CreateFcns called

% Hint: edit controls usually have a white background on Windows.
%       See ISPC and COMPUTER.
if ispc && isequal(get(hObject,'BackgroundColor'), get(0,'defaultUicontrolBackgroundColor'))
    set(hObject,'BackgroundColor','white');
end

% --- Executes on button press in pushbutton2.
function pushbutton2_Callback(hObject, eventdata, handles)
% hObject    handle to pushbutton2 (see GCBO)
% eventdata  reserved - to be defined in a future version of MATLAB
% handles    structure with handles and user data (see GUIDATA)
CLOSEDEVICE;

% --- Executes when user attempts to close figure1.
```

```
function figure1_CloseRequestFcn(hObject, eventdata, handles)
% hObject    handle to figure1 (see GCBO)
% eventdata  reserved - to be defined in a future version of MATLAB
% handles    structure with handles and user data (see GUIDATA)

CLOSEDEVICE;

% Hint: delete(hObject) closes the figure
delete(hObject);

function edit2_Callback(hObject, eventdata, handles)
% hObject    handle to edit2 (see GCBO)
% eventdata  reserved - to be defined in a future version of MATLAB
% handles    structure with handles and user data (see GUIDATA)

% Hints: get(hObject,'String') returns contents of edit2 as text
%        str2double(get(hObject,'String')) returns contents of edit2 as a double

% --- Executes during object creation, after setting all properties.
function edit2_CreateFcn(hObject, eventdata, handles)
% hObject    handle to edit2 (see GCBO)
% eventdata  reserved - to be defined in a future version of MATLAB
% handles    empty - handles not created until after all CreateFcns called

% Hint: edit controls usually have a white background on Windows.
%       See ISPC and COMPUTER.
if ispc && isequal(get(hObject,'BackgroundColor'), get(0,'defaultUicontrolBackgroundColor'))
    set(hObject,'BackgroundColor','white');
end

% --- Executes on button press in pushbutton3.
function pushbutton3_Callback(hObject, eventdata, handles)
% hObject    handle to pushbutton3 (see GCBO)
% eventdata  reserved - to be defined in a future version of MATLAB
% handles    structure with handles and user data (see GUIDATA)
[FileName,PathName,FilterIndex] = uiputfile();
handles.FileName = FileName;
handles.PathName = PathName;
set(handles.edit3, 'String', [PathName FileName]);
guidata(hObject, handles);

function edit3_Callback(hObject, eventdata, handles)
```

```
% hObject    handle to edit3 (see GCBO)
% eventdata  reserved - to be defined in a future version of MATLAB
% handles    structure with handles and user data (see GUIDATA)

% Hints: get(hObject,'String') returns contents of edit3 as text
%        str2double(get(hObject,'String')) returns contents of edit3 as a double


% --- Executes during object creation, after setting all properties.
function edit3_CreateFcn(hObject, eventdata, handles)
% hObject    handle to edit3 (see GCBO)
% eventdata  reserved - to be defined in a future version of MATLAB
% handles    empty - handles not created until after all CreateFcns called

% Hint: edit controls usually have a white background on Windows.
%       See ISPC and COMPUTER.
if ispc && isequal(get(hObject,'BackgroundColor'), get(0,'defaultUicontrolBackgroundColor'))
    set(hObject,'BackgroundColor','white');
end

% --- Executes during object creation, after setting all properties.
function axes1_CreateFcn(hObject, eventdata, handles)
% hObject    handle to axes1 (see GCBO)
% eventdata  reserved - to be defined in a future version of MATLAB
% handles    empty - handles not created until after all CreateFcns called

% Hint: place code in OpeningFcn to populate axes1

% --- Executes when figure1 is resized.
function figure1_ResizeFcn(hObject, eventdata, handles)
% hObject    handle to figure1 (see GCBO)
% eventdata  reserved - to be defined in a future version of MATLAB
% handles    structure with handles and user data (see GUIDATA)
```

A.2.2 STARTDEVICE.m

```
ai = handles.ai;
set(ai,'LogFileName',[handles.PathName handles.FileName]);
set(ai,'LoggingMode','Disk');

delaytime = str2num(get(handles.edit2, 'String'))/1000; %convert from ms to s
handles.delaytime = delaytime;
```

```
handles.timestarted = now;

guidata(hObject, handles);
start(ai);
```

A.2.3 CLOSEDEVICE.m

```
try
    ai = handles.ai;
    if isrunning(handles.ai),
        stop(handles.ai);
        delete(handles.ai);
        clear handles.ai;
        clf(1);
    end
    set(handles.pushbutton1, 'Enable', 'on');
catch
end
```

A.2.4 INITDATA.m

```
%const
samplingrate = 1000;
displayrate = 100;
totaltime = 121;
displaysamples = samplingrate/displayrate;
handles.PathName = '';
handles.FileName = 'data.txt';

%create an analog object
ai = analoginput('nidaq','Dev2');
addchannel(ai,0,'Fz');
addchannel(ai,1,'Mx');
addchannel(ai,2,'My');

handles.samplingrate = samplingrate;
set(ai, 'InputType', 'SingleEnded');
set(ai,'SampleRate', samplingrate);
set(ai,'SamplesPerTrigger',  samplingrate*totaltime);
```

```
ai.SamplesAcquiredFcnCount = displaysamples;
handles.ai = ai;
ai.SamplesAcquiredFcn = {@SamplesAcquiredFcn, hObject};
handles.ai = ai;
set(handles.figure1,'position',[1180+28 0 1280+74 1024]);
set(handles.axes1, 'Position', [74 0 1280 1024]);

% Update handles structure
guidata(hObject, handles);
```

A.2.5 maximize.m

```
function maximize(hObject, eventdata, handles)
set(hObject,'Poisition',[0,0,1280,1024]);
```

A.2.6 SamplesAcquiredFcn.m

```
function SamplesAcquiredFcn(hObject,eventdata,hObjectGUI)

handles = guidata(hObjectGUI);

if (now - handles.timestarted)*100000 > handles.delaytime,

    ai = handles.ai;
    delaytime = handles.delaytime;
    samplingrate = handles.samplingrate;

    dd = samplingrate * delaytime;
    datavec = peekdata(ai, dd);

    Fzd = datavec(1, 1); %channel1
    Mxd = datavec(1, 2); %channel2
    Myd = -datavec(1, 3); %channel3
    xd = Mxd/Fzd;
    yd = Myd/Fzd;

    set(handles.edit1, 'String', num2str( round((now - handles.timestarted)*100000) ));

    lim = 1;
```

```
    hLine1 = plot(xd,yd,'o');
    set(hLine1, 'Parent',handles.axes1);
    set(hLine1, 'XDataSource','xd','YDataSource','yd');
    set(hLine1, 'XData', [xd], 'YData', [yd]);
    set(hLine1, 'MarkerEdgeColor','w','MarkerFaceColor','w','MarkerSize',20);
    set(handles.axes1, 'Position', [74 0 1280 1024]);
    set(handles.axes1, 'XLim', [-lim lim], 'YLim', [-lim lim], 'Color', [0,0,0]);
    set(handles.axes1,'XTick',[],'YTick',[]) ;
    drawnow;
    set(hLine1, 'XData', 0, 'YData', 0);
    set(hLine1, 'MarkerEdgeColor','r','MarkerFaceColor','r','MarkerSize',30);
    drawnow;

end
```

A.2.7 plotConvertWrite.m

```
clc;
clear all;

trial = '1000_5';

trialNameIn = ['data.txt'];
trialNameOut = [trial, '_XY.txt'];
filepathin = 'C:\\experimentXY\\';
filepathout = 'C:\\experimentXY\\JS\\';

fileNameIn = [filepathin, trialNameIn];
fileNameOut = [filepathout, trialNameOut]

data = daqread(fileNameIn);

x = data(:,2)./data(:,1);
y = -data(:,3)./data(:,1);
clear data;

L = 121*1000;

figure(100)
subplot(2,4,[3,4]);
```

```
plot(1:L,x);
subplot(2,4,[7,8]);
plot(1:L,y);
subplot(2,4,[1,2,5,6]);
plot(x,y);
axis equal;

xy = [x,y];
save(fileNameOut, 'xy', '-ASCII', '-TABS');

clear x;
clear y;
clear xy;

disp('Fin.');
```

Appendix B

Model Parameters per Subject

Table B.1 – Model parameters for each subject: lumped inertial and damping term ε, proprioceptive feedback strength κ, visual feedback strength γ, critical or Andronov–Hopf bifurcation delay τ_{crit}, proprioceptive delay τ_{prop} and minimum visual delay $\min\{\tau_{\text{vis}}\}$.

Subject	ε [Hz]	κ [Hz]	γ [Hz]	τ_{crit} [s]	τ_{prop} [s]	$\min\{\tau_{\text{vis}}\}$ [s]
AJ	1.53	2.30	0.2	0.491	0.294	0.2
AK	2.18	3.27	0.2	0.345	0.207	0.2
AT	1.37	2.05	0.2	0.551	0.331	0.2
BR	1.78	2.68	0.2	0.421	0.253	0.2
CB	1.32	1.98	0.2	0.569	0.341	0.2
DA	1.95	2.92	0.2	0.386	0.231	0.2
DG	2.06	3.10	0.2	0.364	0.219	0.2
EH	1.89	2.84	0.2	0.397	0.238	0.2
JS	1.37	2.06	0.2	0.547	0.328	0.2
JW	2.32	3.49	0.2	0.323	0.194	0.2
KT	1.32	1.99	0.2	0.568	0.341	0.2
MN	1.91	2.87	0.2	0.393	0.236	0.2
TC	2.10	3.15	0.2	0.359	0.215	0.2
TK	1.71	2.57	0.2	0.440	0.264	0.2

Appendix C

Consent Form

Informed consent to participate in a study entitled:

Interaction between standing balance and visual feedback.

I, the undersigned, ____, consent to participate in the research study entitled *Interaction between standing balance and visual feedback.*

Researchers

Ramesh Balasubramaniam, Associate Professor, University of Ottawa,

Jason Boulet, Student, University of Ottawa

Funding Organization

N/A

Objective of the research study

The primary objective is to investigate the effects of visual feedback on balance.

Participation in the study

My participation will require attending a ninety minute session at the Sensorimotor Neuroscience Lab. I will be required to look at a visual target placed at eye level.

Advantage for participation in this study

There will be no immediate benefit to me resulting from participation in the study. This study may help further our understanding of balance control.

Risks

There are minimal risks associated with my participation in this study.

Compensatory Indemnity

N/A

Confidentiality of information

Information from the testing and training sessions will be held in strictest confidence and will not be used except for research purposes. It is understood that my data from will be coded in a way that will ensure anonymity. All data will be associated with a numeric code only. I understand that any published results will be presented with complete anonymity. Data will be pooled for analysis, and all identifying documents will be kept separate from data. I understand that any personal data (*e.g.*, address, telephone number) will be kept in a separate file folder, securely stored and accessible only by the researcher responsible for the project in the laboratory. I understand that all experimental data will be kept in a CD, securely stored and accessible only by the researcher responsible for the project in the laboratory. This information may be kept for up to 5 years once the data have been published and will be destroyed at the end of this period.

Questions concerning this study

I understand that I may ask all my questions regarding this study and they will be answered. These questions may be addressed to Ramesh Balasubramaniam (905.525.9140 ext. 21208), principal investigator or Jason Boulet, student investigator.

Contact person

If I have any questions with respect to the ethical conduct of this study, I may contact the Protocol Officer for Ethics in Research, University of Ottawa, Tabaret Hall, 550 Cumberland Street, Room 159, Ottawa, ON K1N 6N5, tel.: 613.562.5841, email: `ethics@uottawa.ca`.

Withdrawal from the study

I understand that participation is voluntary, and that I may withdraw at any time for any reason, without prejudice. In the event of withdrawal, all of the information gathered will be destroyed and will not be used.

Consent

I declare that I understand this project, the nature and the degree of my participation and the possible disadvantages and risks of the project as listed in this consent form. I have had the opportunity to ask all my questions concerning the different aspects of the study and received responses to my satisfaction.

I, the undersigned, ____, voluntarily accept to participate in this study. I can withdraw from the study at any time for any reason. I have had adequate time to make my decision.

Two copies of this consent form have been signed and I have received one signed copy.

Name of participant ____

Signature of participant ____ Date ________________

Name of investigator ____

Signature of investigator ____ Date ________________

University of Ottawa, Faculty of Health Sciences

Bibliography

[1] H. D. I. Abarbanel, R. Brown, J. Sidorowich, and L. Tsimring. The analysis of observed chaotic data in physical systems. *Rev Mod Phys*, 65, 1993. (page 37)

[2] H. D. I. Abarbanel and M. B. Kennel. Local false nearest neighbors and dynamical dimensions from observed chaotic data. *Phys Rev E*, 47(5):3057–3068, 1993. (page 36)

[3] P. Abry. The wavelet-based synthesis for fractional brownian motion proposed by f. sellan and y. meyer: Remarks and fast implementation. *Appl Comput Harmon Anal*, 3(4):377–383, 1996. (page 33)

[4] D. Breda, S. Maset, and R. Vermiglio. Trace-dde: a tool for robust analysis and characteristic equations for delay differential equations. In *Topics in Time Delay Systems: Analysis, Algorithms, and Control*, pages 145–155. Springer-Verlag, New York, 2009. (page 83)

[5] D. Bullock and S. Grossberg. Neural dynamics of planned arm movements: Emergent invariants and speed-accuracy properties during trajectory formation. *Psychol Rev*, 95(1):49–90, 1988. (page 46)

[6] J. Cabrera and J. G. Milton. On-off intermittency in a human balancing task. *Phys Rev Lett*, 89(15):158702, 2002. (page 15, 16)

[7] J. L. Cabrera. Controlling instability with delayed antagonistic stochastic dynamics. *Physica A*, 356:25–30, 2005. (page 47)

[8] O. Caron, B. Faure, and Y. Brenière. Estimating the centre of gravity of the body on the basis of the centre of pressure in standing posture. *J Biomech*, 30(11-12):1169–1171, 1997. (page 61)

[9] S. Carver, T. Kiemel, H. V. D. Kooij, and J. Jeka. Comparing internal models of the dynamics of the visual environment. *Biol Cybern*, 92(3):147–163, 2005. (page 7, 9)

[10] C. Chow and J. Collins. Pinned polymer model of posture control. *Phys Rev E*, 52(1):907–912, 1995. (page 15, 46)

[11] T. Cluff, M. A. Riley, and R. Balasubramaniam. Dynamical structure of hand trajectories during pole balancing. *Neurosci Lett*, 464:88–92, 2009. (page 104)

[12] J. Collins and C. DeLuca. Open-loop and closed-loop control of posture: a random-walk analysis of center-of-pressure trajectories. *Exp Brain Res*, 95(2):308–318, 1993. (page 3, 49, 52, 74, 104)

[13] J. Collins and C. DeLuca. Random walking during quiet standing. *Phys Rev Lett*, 73(5):764–767, 1994. (page 46)

[14] J. Collins and C. DeLuca. The effects of visual input on open-loop and closed-loop postural control mechanisms. *Exp Brain Res*, 103:151–163, 1995. (page 8, 52, 62, 104, 119)

[15] A. Daffertshofer, C. J. C. Lamoth, O. G. Meijer, and P. J. Beek. Pca in studying coordination and variability: a tutorial. *Clin Biomech*, 19(4):415–428, 2004. (page 116)

[16] V. Dietz. Proprioception and locomotor disorders. *Nat Rev Neurosci*, 3(10):781–790, 2002. (page 7)

[17] S. Donker, M. Roerdink, A. Greven, and P. Beek. Regularity of center-of-pressure trajectories depends on the amount of attention invested in postural control. *Exp Brain Res*, 181(1):1–11, 2007. (page 8, 104)

[18] J.-P. Eckmann, S. O. Kamphorst, and D. Ruelle. Recurrence plots of dynamical systems. *Europhys Lett*, 4(91):973–977, 1987. (page 36)

[19] C. Eurich and J. G. Milton. Noise-induced transitions in human postural sway. *Phys Rev E*, 54(6):6681–6684, 1996. (page 2, 6, 15, 16, 46, 52, 54)

[20] R. Fitzpatrick and D. McCloskey. Proprioceptive, visual and vestibular thresholds for the perception of sway during standing in humans. *J Physiol*, 487(1):173–186, 1994. (page 8)

[21] P. Flandrin. On the spectrum of fractional brownian motions. *IEEE Trans Inform Theory*, 35(1):197–199, 1989. (page 33)

[22] T. Frank, A. Daffertshofer, and P. Beek. Multivariate ornstein-uhlenbeck processes with mean-field dependent coefficients: Application to postural sway. *Phys Rev E*, 63(1):11905, 2000. (page 46)

[23] A. Fraser and H. Swinney. Independent coordinates for strange attractors from mutual information. *Phys Rev A*, 33(2):1134–1140, 1986. (page 37)

[24] W. Gage, D. Winter, J. Frank, and A. Adkin. Kinematic and kinetic validity of the inverted pendulum model in quiet standing. *Gait & Posture*, 19:124–132, 2004. (page 3, 5, 6, 46)

[25] L. Glass, A. Beuter, and D. Larocque. Time delays, oscillations, and chaos in physiological control systems. *Math Biosci*, 90:111–125, 1988. (page 45)

[26] H. Gray and W. Lewis. *Anatomy of the human body.* Lea & Febiger, Philadelphia, 20th edition, 1918. (page 6, 9)

[27] S. Guillouzic, I. L'Heureux, and A. Longtin. Small delay approximation of stochastic delay differential equations. *Phys Rev E*, 59:3970–3982, 1989. (page 47, 92)

[28] A. C. Guyton. *Basic Human Neurophysiology.* W. B. Saunders Company, Philadelphia, 3rd edition, 1981. (page 8)

[29] J. Hale, L. M. aes, and W. Oliva. *Dynamics in Infinite Dimensions*, volume 47 of *Applied Mathematical Sciences.* Springer-Verlag, New York, 2002. (page 25)

[30] J. Jeka, K. Oie, and T. Kiemel. Multisensory information for human postural control: integrating touch and vision. *Exp Brain Res*, 134(1):107–125, 2000. (page 9)

[31] J. Jeka, K. Oie, G. Schoner, and T. Dijkstra. Position and velocity coupling of postural sway to somatosensory drive. *J Neurophysiol*, 79:1661–1674, 1998. (page 9)

[32] R. E. Kalman. A new approach to linear filtering and prediction problems. *Trans ASME J Basic Eng*, 82(D):35–45, 1960. (page 11)

[33] E. R. Kandel, J. Schwartz, and T. M. Jessell. *Principles of Neural Science.* McGraw-Hill, 4th edition, 2000. (page 7, 8)

[34] T. Kiemel, K. Oie, and J. Jeka. Multisensory fusion and the stochastic structure of postural sway. *Biol Cybern*, 87(4):262–277, 2002. (page 9, 10, 11, 14, 46)

[35] P. Kloeden and E. Platen. *Numerical Solution of Stochastic Differential Equations*, volume 23 of *Stochastic Modelling and Applied Probability.* Springer-Verlag, New York, 3rd edition, 2000. (page 36)

[36] P. Kloeden, E. Platen, and H. Schurz. *Numerical Solution of SDE Through Computer Experiments.* Springer-Verlag, New York, 1994. (page 34, 35, 68, 69)

[37] U. Küchler and B. Mensch. Langevins stochastic differential equation extended by a time-delayed term. *Stochastics*, 40(1):23–42, 1992. (page 55, 86, 99)

[38] I. D. Loram and M. Lakie. Direct measurement of human ankle stiffness during quiet standing: the intrinsic mechanical stiffness is insufficient for stability. *J Physiol*, 545(3):1041–1053, 2002. (page 5, 6)

[39] I. D. Loram, C. Maganaris, and M. Lakie. Human postural sway results from frequent, ballistic bias impulses by soleus and gastrocnemius. *J Physiol*, 564(1):295–311, 2005. (page 5, 6)

[40] E. Lutz. Fractional langevin equation. *Phys Rev E*, 64(5):51106, 2001. (page 32)

[41] M. Mackey and I. Nechaeva. Solution moment stability in stochastic differential delay equations. *Phys Rev E*, 52(4):3366–3376, 1995. (page 55)

[42] M. Magdziarz, A. Weron, and K. Burnecki. Fractional brownian motion versus the continuous-time random walk: A simple test for subdiffusive dynamics. *Phys Rev Lett*, 103(18):180602, 2009. (page 32, 33)

[43] B. Mandelbrot and J. V. Ness. Fractional brownian motions, fractional noises and applications. *SIAM Rev*, 10:422–437, 1968. (page 49, 50)

[44] T. March, S. Chapman, and R. Dendy. Recurrence plot statistics and the effect of embedding. *Physica D*, 200(1-2):171–184, 2005. (page 38)

[45] G. Marsaglia and W. Tsang. The ziggurat method for generating random variables. *J Stat Softw*, 5(8):1–7, 2000. (page 69)

[46] N. Marwan and J. Kurths. Line structures in recurrence plots. *Phys Lett A*, 336(4-5):349–357, 2005. (page 106)

[47] N. Marwan and J. Kurths. Comment on "Stochastic analysis of recurrence plots with applications to the detection of deterministic signals" by Rohde et al. [Physica D 237 (2008) 619–629]. *Physica D*, 238(16):1711–1715, 2009. (page 106)

[48] N. Marwan, M. C. Romano, M. Thiel, and J. Kurths. Recurrence plots for the analysis of complex systems. *Phys Rep*, 438(5-6):237–329, 2007. (page 38, 39, 106)

[49] N. Marwan, N. Wessel, U. Meyerfeldt, A. Schirdewan, and J. Kurths. Recurrence-plot-based measures of complexity and their application to heart-rate-variability data. *Phys Rev E*, 66(2):1–8, 2002. (page 38, 106)

[50] P. Meyer, L. Oddsson, and C. DeLuca. The role of plantar cutaneous sensation in unperturbed stance. *Exp Brain Res*, 2004. (page 74)

[51] J. G. Milton, J. L. Cabrera, and T. Ohira. Unstable dynamical systems: Delays, noise and control. *Europhys Lett*, 83(4):48001, 2008. (page 15, 47)

[52] J. G. Milton, J. L. Cabrera, T. Ohira, S. Tajima, Y. Tonosaki, C. W. Eurich, and S. A. Campbell. The time-delayed inverted pendulum: Implications for human balance control. *Chaos*, 19(2):026110, 2009. (page 15)

[53] J. G. Milton, J. Townsend, M. King, and T. Ohira. Balancing with positive feedback: the case for discontinuous control. *Phil Trans R Soc A*, 367:1181–1193, 2009. (page 2, 6, 15, 46, 111)

[54] F. Moss and J. Milton. Balancing the unbalanced. *Nature*, 425(6961):911–912, 2003. (page 1)

[55] K. Newell, S. Slobounov, E. Slobounova, and P. Molenaar. Stochastic processes in postural center-of-pressure profiles. *Exp Brain Res*, 113(1):158–164, 1997. (page 49)

[56] P. Pascolo, A. Marini, R. Carniel, and F. Barazza. Posture as a chaotic system and an application to the parkinson's disease. *Chaos Solitons Fractals*, 24(5):1343–1346, 2005. (page 104)

[57] R. Peterka and P. Loughlin. Dynamic regulation of sensorimotor integration in human postural control. *J Neurophysiol*, 91:410–423, 2004. (page 7, 8, 9)

[58] W. H. Press, B. P. Flannery, S. A. Teukolsky, and W. T. Vetterling. *Numerical recipes: the art of scientific computing.* Cambridge University Press, 3rd edition, 2007. (page 38)

[59] J. Proakis and D. Manolakis. *Digital Signal Processing: Principles, Algorithms and Applications.* Prentice Hall, Upper Saddle River, NJ, 3rd edition, 1996. (page 71, 72, 73)

[60] R. D. Rabbitt, E. R. Damiano, and J. W. Grant. Biomechanics of the semicircular canals and otolith organs. In *The Vestibular System*, pages 153–201. Springer-Verlag, New York, 2004. (page 8)

[61] B. Redmond, V. LeBlanc, and A. Longtin. Bifurcation analysis of a class of first-order nonlinear delay-differential equations with reflectional symmetry. *Physica D*, 166(3-4):131–146, 2002. (page 45, 55)

[62] M. A. Riley. Recurrence analysis of human postural sway during the sensory organization test. *Neurosci Lett*, 342(1-2):45–48, 2003. (page 104)

[63] M. A. Riley, R. Balasubramaniam, S. Mitra, and M. Turvey. Visual influences on center of pressure dynamics in upright posture. *Ecol Psychol*, 10(2):65–91, 1998. (page 2, 5)

[64] M. A. Riley, R. Balasubramaniam, and M. Turvey. Recurrence quantification analysis of postural fluctuations. *Gait & Posture*, 9(1):65–78, 1999. (page 104)

[65] M. Roerdink, M. D. Haart, A. Daffertshofer, S. F. Donker, A. C. H. Geurts, and P. Beek. Dynamical structure of center-of-pressure trajectories in patients recovering from stroke. *Exp Brain Res*, 174(2):256–69, 2006. (page 104)

[66] M. Rosenstein, J. Collins, and C. DeLuca. A practical method for calculating largest lyapunov exponents from small data sets. *Physica D*, 65(1-2):117–134, 1993. (page 42)

[67] P. Rougier. Optimising the visual feedback technique for improving upright stance maintenance by delaying its display: behavioural effects on healthy adults. *Gait & Posture*, 19(2):154–163, 2004. (page 2, 8, 45, 48)

[68] P. Rougier. Compatibility of postural behavior induced by two aspects of visual feedback: time delay and scale display. *Exp Brain Res*, 165(2):193–202, 2005. (page 64)

[69] M. Schmid, L. Casabianca, A. Bottaro, and M. Schieppati. Graded changes in balancing behavior as a function of visual acuity. *Neurosci*, 153(4):1079–1091, 2008. (page 8)

[70] B. Seigle, S. Ramdani, and P. Bernard. Dynamical structure of center of pressure fluctuations in elderly people. *Gait & Posture*, 30:223–226, 2009. (page 104)

[71] G. Stepan. Delay effects in the human sensory system during balancing. *Phil Trans R Soc A*, 367:1195–1212, 2009. (page 15, 44, 47)

[72] S. Strogatz. *Nonlinear dynamics and chaos: With applications to physics, biology, chemistry, and engineering.* Westview Press, 2001. (page iv, 20, 21)

[73] F. Takens. Detecting strange attractors in turbulence. *Dynamical systems and turbulence*, 1981. (page 37)

[74] M. Thiel, M. Romano, and J. Kurths. How much information is contained in a recurrence plot? *Phys Lett A*, 330(5):343–349, 2004. (page 106)

[75] M. Thiel, M. Romano, J. Kurths, R. Meucci, E. Allaria, and F. Arecchi. Influence of observational noise on the recurrence quantification analysis. *Physica D*, 171(3):138–152, 2002. (page 115)

[76] C. Tin and C. Poon. Internal models in sensorimotor integration: perspectives from adaptive control theory. *J Neural Eng*, 2(3):S147–S163, 2005. (page 9)

[77] L. Trulla, A. Giuliani, J. Zbilut, and C. Webber. Recurrence quantification analysis of the logistic equation with transients. *Phys Lett A*, 223(4):255–260, 1996. (page 38)

[78] L. Tsimring and A. Pikovsky. Noise-induced dynamics in bistable systems with delay. *Phys Rev Lett*, 87(25):250602, 2001. (page 47)

[79] M. van den Heuvel, R. Balasubramaniam, A. Daffertshofer, A. Longtin, and P. Beek. Delayed visual feedback reveals distinct time scales in balance control. *Neurosci Lett*, 452:37–41, 2009. (page 2, 3, 8, 45, 48, 62)

[80] C. Webber and J. Zbilut. Dynamical assessment of physiological systems and states using recurrence plot strategies. *J Appl Physiol*, 76(2):965–73, 1994. (page 38)

[81] S. Werness and D. Anderson. Parametric analysis of dynamic postural responses. *Biol Cybern*, 51(3):155–168, 1984. (page 7, 52, 54)

[82] D. Winter. Human balance and posture control during standing and walking. *Gait & Posture*, 3:193–214, 1995. (page 6)

[83] D. Winter, A. Patla, F. Prince, M. Ishac, and K. Gielo-Perczak. Stiffness control of balance in quiet standing. *J Neurophysiol*, 80(3):1211–1221, 1998. (page 3, 6, 7, 46, 58, 61)

[84] D. Wolpert, Z. Ghahramani, and M. Jordan. An internal model for sensorimotor integration. *Science*, 269(5232):1880–1882, 1995. (page 9)

[85] N. Yamada. Chaotic swaying of the upright posture. *Hum Mov Sci*, 14(6):711–726, 1995. (page 104)

[86] W. Yao, P. Yu, and C. Essex. Delayed stochastic differential model for quiet standing. *Phys Rev E*, 63(2):21902, 2001. (page 2, 6, 15, 16, 47, 52, 55, 79, 118)

[87] V. Zatsiorsky and M. Duarte. Rambling and trembling in quiet standing. *Motor Control*, 4:185–200, 2000. (page 56, 61)

[88] J. Zbilut and C. Webber. Embeddings and delays as derived from quantification of recurrence plots. *Phys Lett A*, 171(3-4):199–203, 1992. (page 38)